Design of porous materials for environmental remediation

Clara Alves Ponte

Mestrado em Química

Departamento de Química e Bioquímica da Faculdade de Ciências da Universidade do Porto

2020

Orientador

Carlos Gomes, Professor Auxiliar, Faculdade de Ciências da Universidade do Porto

Coorientador

Carlos Granadeiro, Investigador Auxiliar, Faculdade de Ciências da Universidade do Porto

Todas as correções determinadas pelo júri, e só essas, foram efetuadas.

O Presidente do Júri,

Porto, _____/_____/_____

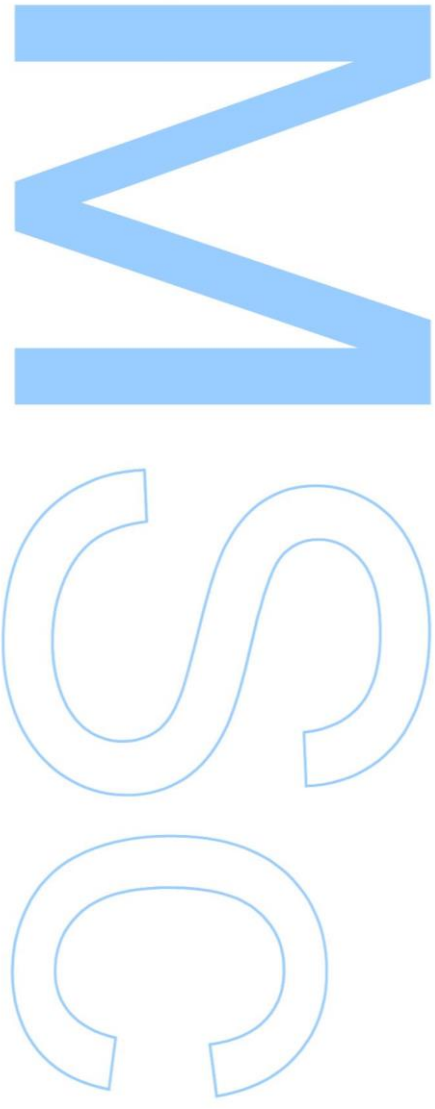

Acknowledgments

Ao Professor Doutor Carlos Gomes, meu orientador, por ter possibilitado a realização desta dissertação.

Ao Doutor Carlos Granadeiro, meu coorientador, pela disponibilidade, dedicação e confiança que depositou em mim.

A todas as pessoas do grupo de investigação que estive inserida, em especial à Doutora Salete Balula, ao Doutor Luís Cunha-Silva, à Doutora Fátima Mirante e à Doutora Diana Julião, pela disponibilidade e boa disposição.

À Doutora Marisa Almeida, pela ajuda nos estudos de adsorção de metais pesados.

À Professora Doutora Manuela Carrott da Universidade de Évora, pela realização das análises de adsorção/dessorção de azoto.

À Mestre Mafalda Flores, pela disponibilidade e ajuda no manuseamento do instrumento de Espectroscopia de Absorção Atómica.

À família e aos amigos por tudo o resto.

Abstract

The experimental work that led to the development of this MSc thesis had as main goal the design of porous adsorbents based on metal-organic frameworks (MOFs) for application in water remediation systems, namely in heavy metal ion removal, since it has become one of the greatest concerns of the twenty-first century.

The preparation of magnetic porous materials has also been addressed aiming at the increased processability and applicability of magnetic adsorbents in aqueous medium.

Concerning the scope of this work, we prepared cobalt- and iron-based MOFs with different organic moieties, enabling the production of extended crystalline frameworks with distinct underlying topologies. Moreover, magnetic MOF-based materials were synthetized through different approaches.

All materials were characterized by a myriad of well-established techniques, namely powder X-ray diffraction (PXRD), Fourier-transform infrared spectroscopy (FT-IR), thermogravimetric analysis (TGA), scanning electron microscopy/energy-dispersive X-ray spectroscopy (SEM/EDS) and nitrogen adsorption/desorption isotherms. The set of data characterization led to the confirmation of their successful preparation and unveiled interesting flexible behaviours of some of the frameworks upon external stimuli.

The adsorption capacity of each adsorbent material towards the removal of copper ions in aqueous solutions was investigated by varying important experimental parameters, such as adsorbent dosage, solution pH, contact time and initial concentration of copper. The studies enabled the evaluation of the effect of such parameters on the overall performance of the adsorption process.

In general, the studied materials revealed to be promising adsorbents towards the removal of copper ions under mild acidic conditions. The adsorption performance of MIL-88B(Fe) stands out, owing to its fast adsorption rate and higher maximum adsorption capacity in comparison to the other materials. Moreover, the adsorbents revealed great chemical stability when subjected to aqueous media as well as promising recycling performances, emphasizing their potential for practical applications.

In conclusion, all the proposed goals of this project have been reached, by effectively synthesizing a wide range of morphologically distinct MOFs as well as magnetic MOF-based materials. The adsorption capacity of the prepared materials has been studied for copper ions, proving their potential for applications in wastewater and/or natural water remediation.

Keywords: metal-organic frameworks; MOF-derived porous carbon; adsorption; magnetic adsorbents; heavy metal ions; environmental remediation.

Resumo

O trabalho experimental desenvolvido no âmbito desta dissertação de mestrado teve como principais objetivos a preparação de materiais adsorventes com base em redes metalo-orgânicas (MOFs) e a sua subsequente aplicação no tratamento de águas residuais, nomeadamente na remoção de iões de metais pesados, pois têm vindo a ser numa das maiores preocupações do século XXI.

A preparação de materiais porosos com propriedades magnéticas também foi um dos principais focos deste trabalho, dada à sua elevada aplicabilidade e processabilidade como adsorventes magnéticos em meios aquosos.

No decorrer deste projeto, foram preparadas várias redes metalo-orgânicas com centros metálicos de cobalto e ferro coordenados a diferentes ligandos orgânicos, permitindo assim a formação de estruturas cristalinas com topologias distintas. Para além disso, também foram sintetizados materiais derivados de MOFs com propriedades magnéticas, através de diferentes metodologias.

Todos os materiais preparados foram caracterizados por diversas técnicas experimentais, nomeadamente, a difração de raios-X de pós (PXRD), espectroscopia de infravermelho por transformada de Fourier (FT-IR), análise termogravimétrica (TGA), microscopia eletrónica de varrimento/ espectroscopia de raios-X por energia dispersiva (SEM/EDS) e isotérmicas de adsorção/desadsorção de azoto. O conjunto de dados de caracterização obtido permitiu confirmar que a preparação dos materiais foi bem-sucedida, para além de revelar que algumas estruturas apresentam caráter flexível, quando sujeitas a estímulos externos.

A capacidade de adsorção de cada material adsorvente na remoção de iões de cobre em soluções aquosas foi estudada através da variação de parâmetros experimentais essenciais, tais como: massa de adsorvente, pH da solução, tempo de contacto e concentração inicial de cobre, permitindo assim avaliar o seu efeito no desempenho global do processo de adsorção.

De forma geral, os materiais estudados revelaram ser adsorventes promissores para a remoção de iões de cobre sob condições moderadamente ácidas. O desempenho do MIL-88(Fe) destacou-se em comparação aos outros materiais estudados, devido à sua rápida adsorção e elevada capacidade máxima de adsorção. Para além disso, todos os adsorventes mostraram ótima estabilidade química e reutilização promissora, evidenciando assim o seu potencial para aplicação em larga escala.

Posto isto, conclui-se que todos os objetivos deste projeto foram atingidos, tendo sido possível sintetizar vários MOFs morfologicamente distintos, bem como materiais magnéticos baseados em MOFs. A capacidade de adsorção dos materiais preparados

foi avaliada para a remoção de iões de cobre, tendo assim demonstrado o seu potencial para a aplicação na remediação de águas residuais e/ou naturais.

Palavras-chave: redes metalo-orgânicas; materiais de carbono derivados de MOFs; adsorção; adsorventes magnéticos; iões de metais pesados; remediação ambiental.

Table of contents

List of Figures

List of Tables

List of Abbreviations

0D	Zero – Dimensional
1D	One – Dimensional
2D	Two – Dimensional
3D	Three – Dimensional
AAS	Atomic Absorption Spectroscopy
as	As-Synthetized
BET	Brunauer-Emmett-Teller
CP	Coordination Polymer
DLS	Dynamic Light Scattering
DMF	N,N-dimethylformamide
DTG	Thermogravimetric Derivative
EDS	Energy Dispersive X-Ray Spectroscopy
ELS	Electrophoretic Light Scattering
EPA	United States Environmental Protection Agency
EtOH	Ethanol
FT-IR	Fourier Transform-Infrared Spectroscopy
H_2BDC	Benzene-1,4-dicarboxylic acid
H_3BTC	Benzene-1,3,5-tricarboxylic acid
HSAB	Hard/Soft Acid-Base
IR	Infrared
IUPAC	International Union of Pure and Applied Chemistry
lp	Large Pore
MCL	Maximum Contaminant Level
MDPCs	MOF-Derived Porous Carbons
MIL	Materials of Institute Lavoisier
MIL-53Y	Materials of Institute Lavoisier-53(Fe) Yellow
MIL-53R	Materials of Institute Lavoisier-53(Fe) Red
MNPs	Magnetic Nanoparticles
MOF	Metal-Organic Framework
MTN	Mobile Thirty-Nine
MTV-MOFs	Multivariate Metal-Organic Frameworks
np	Narrow Pore
PCP	Porous Coordination Polymers

PDI	Polydispersity Index
PFO	Pseudo-First Order
PSM	Post-Synthetic Modification
PSO	Pseudo-Second Order
PXRD	Powder X-Ray Diffraction
rpm	Rotation Per Minute
SBU	Secondary Building Unit
SE	Standard Error
SEM	Scanning Electron Microscopy
TG	Thermogravimetric
TGA	Thermogravimetric Analysis
TMAOH	Tetramethylammonium Hydroxide Solution
ZIF	Zeolitic Imidazolate Framework
ZIF-DPC	Zeolitic Imidazolate Framework-Derived Porous Carbon

List of Symbols

A	Absorbance
$A_{s,BET}$	Specific surface area (BET model)
a_m	Cross-section area occupied by a single molecule
B	Density conversion factor
c	Concentration
c_0	Initial concentration
c_{ad}	Adsorbed concentration
C_{BET}	BET constant
c_e	Equilibrium concentration
d_{hkl}	Atomic spacing between lattice planes (*hkl*)
D_p	Pore diameter
D_h	Hydrodynamic diameter
d_{SEM}	Diameter obtained from SEM micrographs
I	Transmitted light Intensity
I_0	Initial light intensity
k_1	Rate constant of PFO
k_2	Rate constant of PSO
K_f	Freundlich constant of adsorption capacity

K_L	Langmuir constant
L	Optical path length
m	Mass
N	Number of points
N_A	Avogadro constant
n	Freundlich constant of adsorption intensity
n_{ads}	Amount adsorbed
n_i	Integer number
p	Pressure
p^0	Saturation pressure
pH_{ZPC}	pH at point of zero charge
pK_a	Acid dissociation constant
q	Adsorption capacity
q_e	Adsorption capacity at equilibrium
$q_{e,exp}$	Experimental adsorption capacity at equilibrium
$q_{e,cal}$	Predicted adsorption capacity at equilibrium
q_{max}	Maximum adsorption capacity
q_t	Adsorption capacity at time t
R_L	Separation constant
R^2	Determination coefficient
s^2	Variance
t	Time
V	Volume
V_m	Volume of adsorbed monolayer
V_{molar}	Molar volume
V_p	Total pore volume
w	Number of estimated parameters
δ	Bending vibrational mode
Δ	Variation
ε	Molar extinction coefficient
ζ	Zeta
θ	Angle between incident X-ray beam and lattice plane
λ	Wavelength
ν	Stretching vibrational mode
ν_{as}	Asymmetric stretching vibrational mode

ν_s	Symmetric stretching vibrational mode
$\bar{\nu}$	Wavenumber

1. Contextualization

1.1. Water pollution

Water is widely regarded as the most essential natural resource to sustain life on Earth.[1] Having access to potable water is a mandatory requirement for human development and well-being.[2] However, the most challenging problems that humanity is facing in the twenty-first century are related to water quantity and/or water quality issues.[3]

Human activities have always produced waste, and this was not a major problem when the human population was relatively small and nomadic, but since the advent of the industrial revolution these have generated a serious negative impact on the Earth's ecosystem.[4] The combination of several factors such as: rapid and continuous growth of world population, the advancement of technology, fast industrialization, increase of energy and commodity consumption, and the modernization of developing countries led to unprecedented amounts of hazardous wastes threatening freshwater resources all over the world and consequently the sustainability of life on Earth.[5-6]

Nowadays, the Earth's water system is the natural resource that has been more affected by environmental pollution and overexploitation, which will persist and even be aggravated in the following decades due to climate change posing harmful risks to the whole environment (Figure 1.1).[7]

Currently, more than one third of the global population is living in areas where water is scarce or/and do not have access to safe drinking water leading to severe effects on human health.[7] There are some alternatives to obtain freshwater such as from groundwater or through desalination of seawater. However, the technologies required are not yet affordable for the majority of

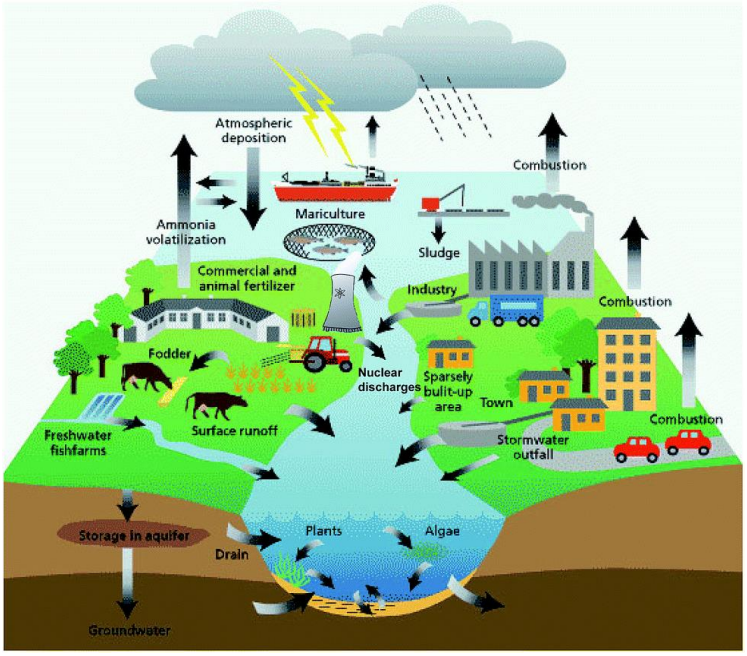

Figure 1.1. Anthropogenic sources of water contamination in the hydrologic cycle. Adapted from [5].

the world, besides that overexploitation of aquifers together with the rise of sea level can lead to groundwater contamination by saltwater.[5]

The most sustainable alternative to circumvent the world's water crisis is to develop technologies for an efficient removal of contaminants from water, which will allow wastewater recovery/reuse and environmental preservation, contributing to the re-establishment of the planet's environmental balance.[5]

1.1.1. Water Contaminants

According to the United States Environmental Protection Agency (EPA)[8], a contaminant is defined as any physical, chemical, biological or radiological substance present where it would not normally occur or at concentrations above natural background but not necessarily harmful to the surroundings. Pollutants are contaminants that cause or can cause adverse effects in the environment and consequently to the natural development of living beings.[9] All water resources contain contaminants, that can be from natural sources, particularly inorganic substances that arise from geological strata through which water flows and volcanic activities, or from anthropogenic sources, such as by-products of industrial (mining, chemical, battery, metallurgical, textile dyes), agricultural and domestic waste.[10-11]

Water pollutants can be categorized as organic, biological or inorganic substances and are present either in solvated, colloidal or in suspended form.[12] Organic pollutants are a wider family than inorganic contaminants, and the most common organic contaminants found in water include dyes, detergents, oils, pesticides (insecticides, herbicides and fungicides), polycyclic aromatic hydrocarbons, pharmaceuticals and personal care products. Even though some of these pollutants might be biodegradable, the large amount of continuous production/discharge in modern societies makes them pseudo-persistent in our environment.[13]

Biological contaminants include different types of microbes that are responsible for several serious diseases. The most harmful microbes present in wastewaters include bacteria, fungi, algae, viruses, amoeba, plankton and other worms.[12]

Inorganic contaminants include oxyanions/cations, metal ions and radioactive substances.[14] This type of pollutants, specially the heavy metals and radionuclides represent a major concern to the ecosystems due to their persistency in the environment and high toxicity even at low concentrations. Owing to their charged nature, these substances are highly soluble in water making them extremely bioavailable and liable to bioaccumulation in the human body and food chain leading to severe chronic diseases.[15-16] Hence, the removal of these substances from effluents before discharging wastewater to the environment is a subject of extreme importance.[17] Table 1.1 summarizes some of

the main anthropogenic sources, their adverse effects on human health and the safety standard levels of several toxic heavy metals.

Table 1.1. Significant anthropogenic sources, health effects and MCL standards of heavy metals.

Heavy metal	Industrial source[18-20]	Health effects[10, 18-20]	MCL[a] (mg/L)[2, 19]
As	Metal refineries Electronics Paints and pigments	Skin and vascular diseases, visceral cancer	0.010
Cd	Mining Metal refineries Electronics Batteries	Renal failure, carcinogenic, respiratory, and gastrointestinal diseases, bone damage, anaemia, Itai-Itai disease	0.003
Cr	Electroplating Mining Metal refineries Fertilizers Electronics Paints and pigments	Carcinogenic, genotoxic, alopecia, nausea, headache, skin inflammation, liver and kidney damage, pulmonary congestion	0.05
Cu	Mining Metal refineries Printing circuit Electroplating Paints	Liver and kidney damage, carcinogenic, irritation in the gastrointestinal tract, lethargy, anaemia, hair loss	2
Hg	Batteries Paper and pulp Electronics Manures sewage	Neurobehavioral disorders and developmental disabilities, kidney disease, rheumatoid arthritis, and circulatory disorder	0.006
Ni	Mining Metal refineries Landfill leachate Electroplating Batteries	Dermatitis, chronic asthma, carcinogenic, pulmonary fibrosis, renal edema, gastrointestinal ache, náusea, anaphylaxis	0.07
Pb	Fertilizers Metal refineries Explosives Electronics Batteries Paints and pigments	Renal failure, nervous system damage, carcinogenic, circulatory, and muscular disorders	0.01
Zn	Mining Fertilizers Metal refineries Paper and pulp Electroplating Batteries Paints and pigments	Skin inflammation, fever, nausea, anaemia, lethargy, depression	0.80

[a] Maximum contaminant level (MCL): The maximum concentration of a contaminant that is permitted in drinking water.

1.1.2. Wastewater treatment techniques

The main objective of wastewater treatment is to reduce the amount of specific pollutants to the level at which the discharge of the effluent will not adversely affect the environment or the health of living beings. Water treatment plants rarely contain a single method, instead they typically have a combination or sequence of methods which depends on the quality of the untreated water and the desired quality of the treated water.[21] At present, unit operations and techniques are combined to provide primary, secondary and tertiary water treatment in a typical wastewater treatment plant (Figure 1.2).[22]

Primary treatment is normally applied when water is highly polluted and involves physical processes such as screening and sedimentation methods to remove large floating materials, grit and sand, which could damage the equipment in the next steps.[12, 22]

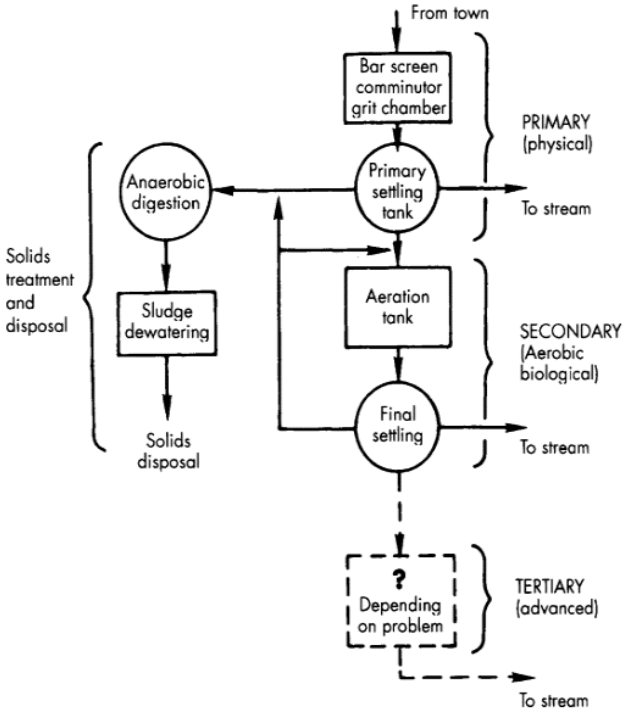

Figure 1.2. Diagram of a complete wastewater treatment plant. Adapted from[22].

In the secondary treatment, much of the solid organic matter has been removed, but still contains high content of organic pollutants.[22] This step is a biological process that uses microorganisms, usually bacterial and fungal strains.[12] If free dissolved oxygen is available in the wastewater, then aerobic decomposition processes occur, by aerobic and facultative bacteria, and the organic matter is converted into water and carbon dioxide.[23] If oxygen is not freely available, then anaerobic digestion occurs instead, in which anaerobic and facultative bacteria convert complex organic matter into simpler organic compounds based on nitrogen, carbon and sulphur.[24]

The tertiary treatment is the final and most important step in which the wastewater is converted into good quality water and can be used for different purposes, e.g. human consumption, industrial, agricultural and medicinal.[12] At present, several procedures have been applied at this stage depending upon the nature of the pollutants that are present in the wastewater. For the removal of inorganic contaminants, particularly heavy metal ions, the most common techniques are chemical precipitation, ion-exchange,

membrane filtration, coagulation-flocculation, flotation, electrochemical treatment and adsorption.[16, 20] Each of these methods has advantages and disadvantages that must be considered in order to select the most appropriate method or combination of different techniques to address a specific issue.

1.1.2.1. Chemical precipitation

Chemical precipitation is a widely used method to remove soluble ionic contaminants which involves alteration of the ionic equilibrium to produce insoluble precipitates by the addition of counter ions, that can be removed by coagulation and/or sedimentation or filtration.[25] This is a common treatment technique employed in industrial scale applications, especially for the removal of heavy metal ions and water softening, but also for removal of anions such as phosphate, fluoride and cyanide.[6] Most metals are precipitated as hydroxides, using calcium or sodium hydroxide, although other methods such as sulphide and carbonate precipitation are also used, by adding hydrogen or sodium sulphide and calcium carbonate, respectively.[20, 25]

This technique has the advantage of being relatively inexpensive, simple to operate and useful for removing the bulk of the metal ions.[26] However, its major disadvantages are the large volume of sludge produced with an excessive amount of precipitated metals which is difficult and expensive to treat and dispose, and is not efficient enough to remove the necessary metal ion content to meet the current water quality standards.[20]

1.1.2.2. Ion exchange

Ion exchange treatment is also an extensively used method for the removal or recovery of low concentration ionic contaminants dissolved in wastewater.[27] This technique is based on the exchange of toxic ions present in solution with the non-toxic ions from an ion exchanger.[12] Ion exchangers are resins, generally, made up of cross-linked polymer matrices of natural or synthetic origin with functional groups attached through covalent bonding at the resin surface.[20] Synthetic resins are usually preferred due to their efficiency to separate metal ions from solution and durability.[28] The ion exchangers can be classified as cation or anion exchange resins, based on the functional groups attached to the polymer matrix. The most common cation exchangers are strongly or weakly acidic resins with sulfonic or carboxylic groups, respectively. The anionic exchangers can be strongly or weakly basic resins with quaternary amine functional groups, or tertiary/secondary amine groups, respectively.[29] The main advantages of this technique are its selectivity, efficiency, and the reduced production of toxic sludge amount. However, its major drawbacks are the expensive equipment and maintenance required, especially when treating a large amount of wastewater.[30-31]

1.1.2.3. Membrane filtration

Membrane filtration has received considerable attention for water treatment since it can remove not only suspended solid and organic compounds, but also inorganic contaminants such as heavy metals.[18, 32]

There are different types of membrane processes commonly used in water purification, that can be pressure driven such as microfiltration, ultrafiltration, nanofiltration, reverse osmosis or electrically driven like electrodialysis.[33] The main differences among the pressure driven methods are the membranes pore sizes, that can range from 0.1 μm (microfiltration) [34] to less than 1 nm (reverse osmosis)[35], and the required operating pressure which tends to increase with the decreasing of pore size.[36]

The nanofiltration and reverse osmosis are the most promising techniques for the removal of ion contaminants, but ultrafiltration can also be used with the addition of surfactants or polymers as complexing agents resulting in the formation of aggregates which are more easily retained by membranes, designated as micellar and polymer enhanced ultrafiltration, respectively.[28, 37]

Electrodialysis separates ion contaminants under the influence of an electric potential.[38] When an electrical potential difference is applied between the two electrodes, cations move towards the cathode while anions move towards the anode crossing ion-selective membranes that retain the desired ionic contaminants.[39] This method has proven to be a promising alternative for reverse osmosis and nanofiltration for the removal of heavy metals and in the production of potable water.[16]

Reduced solid waste generation, low chemical consumption and possibility to be metal selective are some of the advantages of membrane filtration, although besides not being economically viable due to high maintenance and operational costs, the process complexity, membrane fouling and low permeate flux have also been identified as some of its disadvantages.[16, 28]

1.1.2.4. Coagulation-flocculation

Coagulation-flocculation is a two stepped process that is also one of the most applied technologies at industrial scale wastewater treatment.[40] The first step is the coagulation process that consists in particles destabilization by adding coagulant agents (iron salts, alum and lime) that reduce the electrostatic forces between the particles.[41] The coagulation is followed by flocculation, which is the action of flocculants (polyaluminium choride, polyferric sulfate or polyacrylamide) to induce agglomeration between the unstable particles in order to increase their size and create bulky floccules which can be removed by filtration.[42] Although, this technique is applicable to large scale wastewater treatment, it lacks sustainability due to the operational costs involved and the production

of large amount of toxic sludge. Besides, conventional coagulants and flocculants are not efficient on the removal of heavy metal ions.[28, 43]

1.1.2.5. Adsorption

Adsorption has been recognized as an efficient technique for water treatment that can be applied for the removal of several organic and inorganic contaminants even at low concentrations.[44] Adsorption is a mass transfer operation that involves the contact of a solid phase with a fluid phase (liquid or gas), leading to the accumulation of a substance at their interface, in this case at a solid-liquid interface.[45] The solid on which adsorption occurs is known as adsorbent and the substance that accumulates at the interface is called adsorbate. The transference of the adsorbate from the liquid phase to the adsorbent surface will continue until the equilibrium between the amount of adsorbate adhered to the adsorbent surface and the remaining amount of adsorbate in solution is reached.[46] Depending on the interactions that occur between the adsorbent and the adsorbate, the adsorption phenomenon can be classified into two types: chemical adsorption (or chemisorption) and physical adsorption (physisorption).[47]

Chemical adsorption involves electron transfer which results in the formation of strong chemical bonds (covalent bonds) between molecules or ions of adsorbate and the adsorbent surface. This process is highly specific associated to high adsorption energies, ranging from 40 to 800 kJ/mol, and subsequently, the desorption process is very difficult, generally even irreversible and only a monolayer of adsorbate is observed.[46]

Physical adsorption is characterized by non-specific binding forces, such as Van der Waals, hydrogen bonds, electrostatic and π-π interactions, between the adsorbate and adsorbent, and hence it is associated with lower adsorption energies, ranging from 4 to 40 kJ/mol, and consequently the adsorption process is reversible in most cases and multilayer adsorption is possible. This type of adsorption is the most common mechanism by which contaminants are removed in water treatment [48]

Adsorption is considered an attractive and environmental friendly alternative for the treatment of polluted waters and it is usually advantageous comparing to other methods owing to its simplicity, cost-effectiveness, versatile design and operation conditions, low-energy requirements, minimal sludge production and the possibility of adsorbent regeneration by suitable desorption processes allowing its reutilization.[44, 46, 49]

However, after the adsorption process, additional operation steps are usually required to recover the adsorbents from the aqueous media, such as filtration, sedimentation, or centrifugation, which increase the cost of their industrial application and can be time-consuming. Therefore, great efforts have been made to develop and

implement strategies to overcome this drawback. More recently, the use of adsorbents with incorporated magnetic properties is one of the most promising approaches to solve this limitation, due to their easy and fast recovery from the solution through the simple application of an external magnetic field.[50]

Moreover, the adsorption efficiency is highly dependent of several factors that must be considered including adsorbate-adsorbent interactions, adsorbent dose and initial adsorbate concentration (adsorbent/adsorbate ratio), adsorbent particle size, pore volume and surface area, temperature, pH, contact time and the presence of other pollutants.[48, 51-52]

Nowadays, activated carbon has been widely employed as an adsorbent to purify polluted water owing to its high surface area and chemical stability in solution[53]. However due to its high cost, many researchers have developed low-cost adsorbents based on natural materials and biowaste[54], such as clay minerals[55], zeolites[56], chitosan[57], silica[58] and algae[59]. Although these adsorbents are available in large quantities in the environment they present some disadvantages regarding their heterogeneous structure, random pore size distribution and irregular geometry, low adsorption capacity, slow adsorption kinetics, limited selectivity and poor recycling ability.[60-62] Thus, the design of advanced porous materials to overcome such limitations and achieve more efficient and sustainable adsorption processes is of uttermost importance.[61]

A good adsorbent should present some specific requirements, including: well-designed pore size and geometry with open pore structure and regular distribution, high accessible surface area, ease of desorption and reuse, mechanical, chemical and thermal stability, simple synthetic procedures, low cost (considering both the cost of the material synthesis as well as the equipment required for the adsorbent performance), ability to provide fast kinetics and mainly to exhibit a high adsorption capacity.[46, 60, 63]

In the past few years, metal-organic frameworks (MOFs) have been extensively studied for a wide variety of applications due to their unique and versatile properties, and more recently have also been applied in water decontamination systems, revealing promising features and performances as new advanced adsorbents.[61]

1.2. Metal-Organic Frameworks (MOFs)

The term coordination polymer (CP) has been in continuous use since the 1960's, but it was first introduced by Y. Shibata in 1916.[64] According to IUPAC, a CP is a coordination compound with repeating coordination entities extending in 1, 2 or 3 dimensions (1D-, 2D-, 3D-, respectively). [65] These polymeric structures are composed of metal ions or metal clusters (nodes) coordinated by multi-dentate ligands (linkers) that can be extended into supramolecular chains (1D), sheets (2D) or 3D frameworks (Figure

1.3). Moreover, the self-assembly of these supramolecular structures not only arise from coordination bonds, but also due to additional weaker interactions, such as hydrogen bonding, π-π stacking and Van der Waals interactions.[66]

The topology and properties of CPs are determined by several factors, such as the nature of the bridging ligands (e.g. flexibility and denticity) as well as the coordination number and coordination preference of the metal ions. Also, these can be highly affected by external chemical or physical stimuli, namely reaction temperature, pressure, pH, counter ions of the metal salt precursors, solvent and the stoichiometric metal-to-ligand ratio.[67-68] Different CPs can be produced from the same specific molar ratio of a given set of metal and ligand by simply changing the reaction conditions.[69] Thus, owing to this wide variety of factors, the CPs can be purely inorganic (e.g. Prussian blue) or metal-organic species with crystalline, amorphous, porous or non-porous structures.

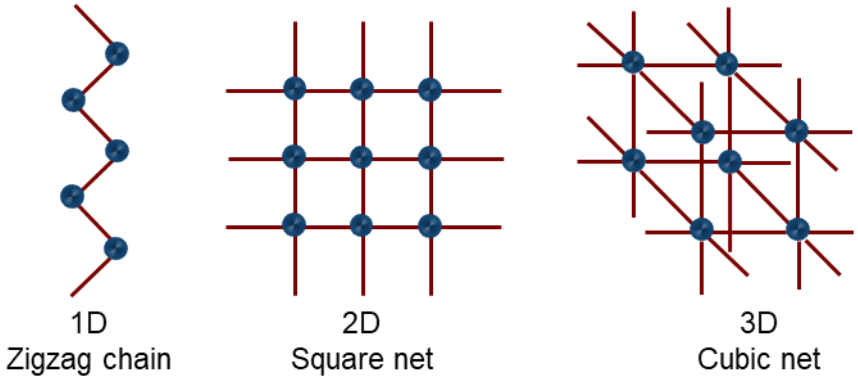

Figure 1.3. Scheme of simple CPs with different structural dimensions.

According to IUPAC, MOFs, or porous coordination polymers (PCP), are a subclass of CPs, defined as coordination networks, with organic ligands containing potential voids. IUPAC also defines a coordination network as a coordination compound extending through repeating coordination entities in 2 or 3 dimensions.[65] Therefore, MOFs are widely known as 2- or 3-dimensional crystalline materials with intrinsic porosity, leading to high surface areas, up to 10000 m^2/g, due to the periodic arrangement of polytopic organic ligands and mono- or poly-nuclear metal nodes by strong coordinating bonds.[70]

The term “MOF” first appeared in the literature by Omar Yaghi in 1995 [71] and in 1999 he and co-workers reported the first robust MOF with permanent porosity, MOF-5, based on the primitive cubic lattice (**pcu**), with more than three times the internal surface area of the most porous zeolites.[72] Since then, many research groups, have been focusing on the synthesis and characterization of several new MOFs, with more than 20,000 different structures being reported, associated with multiple unique chemical or physical properties making them versatile materials towards numerous potential applications, such as, optics, heterogeneous catalysis, luminescence sensing, adsorption, gas storage and separation (e.g. CO_2, H_2 and CH_4), drug delivery and others.[70, 73]

The understanding and construction of MOFs emerged from reticular chemistry directives, which involve preparing materials through the linkage of building units via strong bonds to give rise to tailored extended crystalline structures. In the context of reticular chemistry, the topology of each structure can be described by three-letter symbols, and their details are available in official databases. Many topologies are named after naturally occurring materials, such as sodalite (**sod**) or diamond (**dia**).[74]

1.2.1. Structural Components

MOFs can be obtained from a large variety of di-, tri-, or tetravalent metal cations. The most common are transition metal ions, such as Zr^{4+}, Fe^{3+}, Cr^{3+}, Ni^{2+}, Cu^{2+}, Cd^{2+}, Zn^{2+}, Co^{2+}, and some from the main-group metals such as Mg^{2+}, Al^{3+} or Ga^{3+}, due to their predictable coordination geometries, stability, and kinetic lability. The coordination number of these cations can range from 2 to 7, depending on the element and its oxidation state, giving rise to numerous geometries (e.g. tetrahedral, trigonal planar or bipyramidal, square planar and octahedral). More recently, lanthanide ions, such as La^{3+}, Tb^{3+} and Eu^{3+}, have also been used as inorganic connectors, owing to their interesting properties (e.g. luminescence) and large coordination numbers (greater than 6), that lead to polyhedral coordination geometries with unusual network topologies.[66, 77]

However, it is difficult to produce robust and stable MOFs with permanent porosity from single metal ions nodes, because they do not impose a strong preference for a given coordination geometry, which can result in a unstable and flexible coordination environment around the metal ion leading to more than one type of structures and consequently to overall lack of predictability and control over the final structure of the framework.[75, 78]

In order to circumvent this, the inorganic nodes of MOFs are based on multinuclear metal-oxo-clusters, also known as secondary building units (SBUs), which use carboxylate

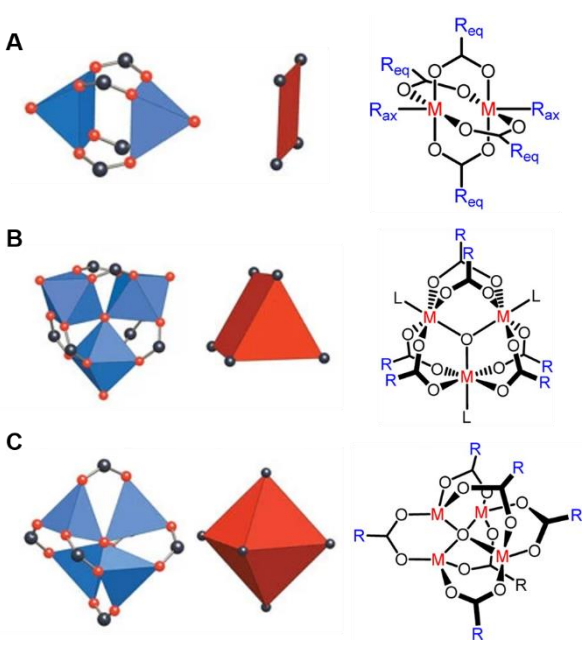

Figure 1.4. Some common SBUs geometries. A: Square-planar coordination geometry from binuclear “paddle-wheel” node. B: Trigonal prismatic coordination geometry from trinuclear node. C: Octahedral coordination geometry from tetranuclear node. Adapted from [75-76].

functional groups to chelate metal ions and lock them into rigid and directional positions with intrinsic and well-defined geometric properties that enable the design of robust frameworks with permanent porosity (Figure 1.4). This concept is fundamental to understand, predict and rationalize the resulting topologies of metal cluster-based MOFs structures. Typically, SBUs are formed *in situ,* which provides the possibility of a slow and reversible assembly of the overall structure allowing error correction mechanisms, owing to the metal-ligand coordination bonds lability and, thus ensuring the formation of highly ordered crystalline products.[75, 78] The SBUs not only provide mechanical and architectural stability to the framework, but also ensure thermodynamic stability to the MOFs, due to the fact that they are only composed by strong bonds (M-O, C-O, and C-C).[79] The SBU approach was adapted from the zeolite chemistry, where SBUs exclusively arise from inorganic components (such as tetrahedral species like SiO_4, AsO_4, PO_4, connected to metallic cations), being one of the most important advances with great impact on the development of MOFs over the years.[80]

According to G. Férey, the dimensionality of the inorganic subnetworks can be not only discrete clusters (0D), but also extended motifs with 1D-chains, 2D-grids or 3D-networks, depending on the chemical conditions (Figure 1.5).[80] Thus, MOFs represent the interface between purely organic or inorganic porous materials and can contain numerous different structural backbones.

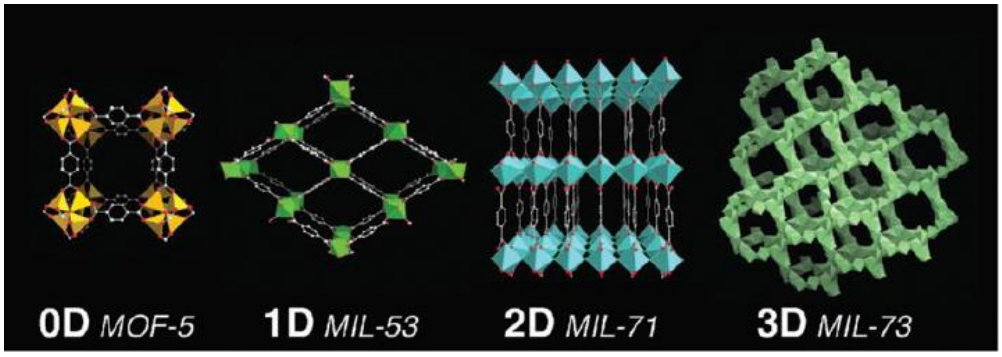

Figure 1.5. Examples of MOFs with SUBs of different dimensionalities (MIL stands for Materials of Institute Lavoisier). Adapted from [80].

The inorganic nodes are connected by organic ligands that are commonly molecules with two or more functional groups containing donor atoms, such as anionic oxygen atoms (e.g. carboxylate groups and less often phosphates and sulfonates) or neutral nitrogen atoms (e.g. pyridyl, imidazole and nitrile groups).[66] Also, more than one type of potential coordination functional group may be present within the same ligand molecule, named hetero-functional ligands.[81] (Figure 1.6)

Typically, to synthesize robust and porous MOFs, anionic carboxylate-based linkers are preferred over neutral donor linkers due to several aspects, such as: the charged

functional groups neutralize the positively charged metal nodes allowing the self-assembly of neutral frameworks without the need for additional counter ions, and their chelating ability promote the formation of SUBs with a specific coordination geometry, which results in rigid and directional structures with high thermal, mechanical and chemical stability.[74]

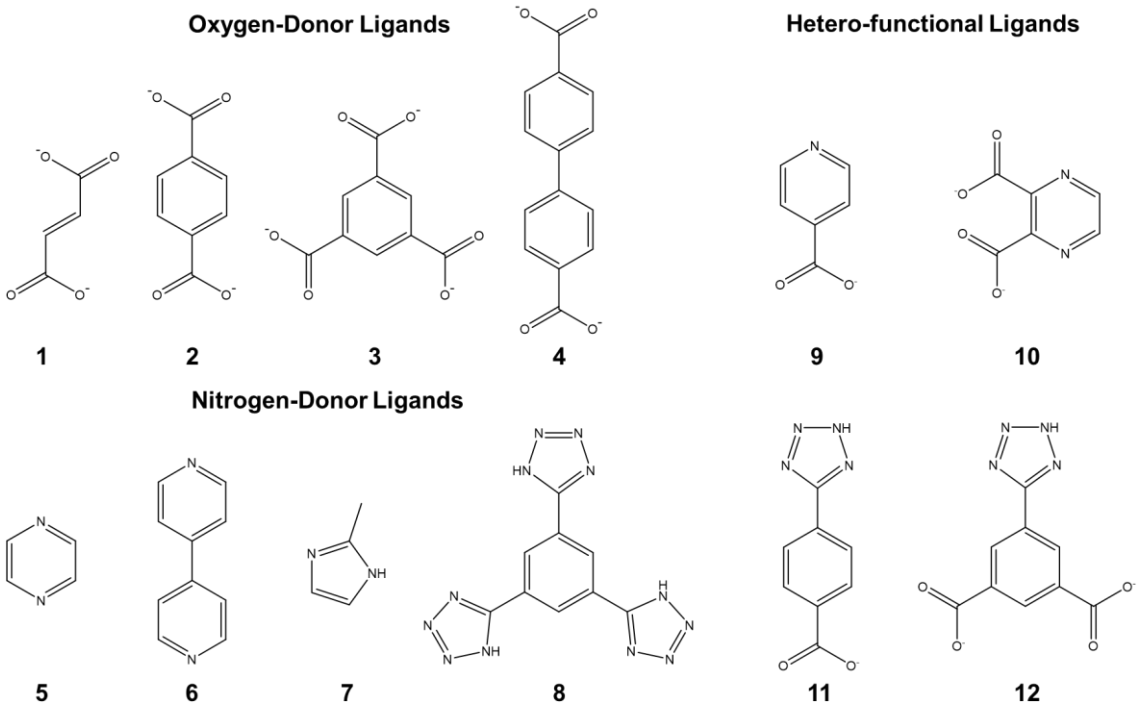

Figure 1.6. Examples of organic ligands that are used in MOFs construction. (1) But-2-enedioate, fumarate; (2) Benzene-1,4-dicarboxylate, terephthalate; (3) Benzene-1,3,5-tricarboxylate, trimesate; (4) 4,4'-biphenylenedicarboxylate; (5) pyrazine; (6) 4,4'-bipyridine; (7) 2-methylimidazole; (8) 1,3,5-tris(2H-tetrazol-5-yl)benzene; (9) 4-Pyridylcarboxylate, isonicotinate; (10) 2,3-pyrazinedicarboxylate; (11) 4-(1H-tetrazol-5-yl)benzoate and (12) 5-(2H-tetrazol-5-yl)benzene-1,3-dicarboxylate.

The intrinsic structural characteristics of the organic ligands, such as coordination ability, length, flexibility, geometry and orientation of the binding groups play a crucial role in dictating the framework topology for a given cationic SBU.[82] So, another useful approach to avoid lack of predictability of the final crystalline structure is to use ligands with rigid backbones containing aromatic or unsaturated aliphatic compounds and of relatively high symmetry. By doing so, extended crystalline networks with high structural stability and persisting porosity can be produced and able to retain its integrity even when the guest molecules are removed from the pores.[78, 83]

The charge of the framework is also an important factor in the construction of MOFs. Since the inorganic units are positively charged, there is a need for an anionic source to neutralize the overall charge and yield neutral networks. This can result either from the organic ligands with negatively charged coordinating groups, such as carboxylates, or in

the case of neutral bridging ligands, from additional counter ions, originally from the metal salt precursor, such as Cl^-, NO_3^-, SO_4^{2-} and BF_4^-.[66, 83]

The chemical and physical properties of MOFs, such as pore size, surface chemistry and chemical stability can be finely controlled and enhanced through several strategies towards specific applications without changing the underlying topology of the MOF framework, known as isoreticular chemistry.[86-87] Functionalization is a powerful and versatile tool to modulate the surface chemistry of the MOF structures, which increase their use for more specialized applications.[86] There are two main approaches that can be employed to integrate additional functionalities into these materials. The first involves the direct solvothermal synthesis of MOFs using previously functionalized organic linkers with specific chemical groups (figure 1.7a).[88] This approach is limited to relatively simple substitutes, such as $-NH_2$, -Br, $-CH_3$, due to the fact that many functional groups are not compatible with the material synthetic conditions or they may interfere with the formation of the desired topology.[84] Thus, an alternative approach has emerged to circumvent these restrictions, known as post-synthetic modification (PSM) approach, which consists on the chemical modification of MOF structures after their synthesis.[84-85, 88] The PSM approach allows a higher control and variety of the functional groups that can be incorporated into the MOF structure without affecting the inherent topology.[84] PSM can be used to functionalize not only the MOFs organic components, but also the metal clusters, through covalent and coordinate covalent modifications, respectively (Figure 1.7b and c).[88-89]

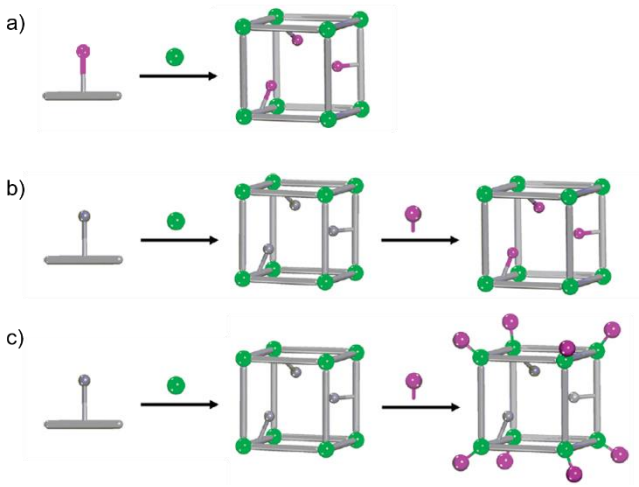

Figure 1.7. General schemes for the preparation of functionalized MOFs by using a) prefunctionalized organic linkers, b) covalent PSM, and c) coordinate covalent PSM. Adapted from[84-85].

Moreover, it is possible to enhance their porosity and surface areas by creating MOFs with unusually large pore openings and thus increase their surface areas through isoreticular expansion, which consists on preparing extended frameworks with similar, but longer organic linkers than those used on the parent MOFs.[86, 90] However, the presence of large voids within a single framework can promote the formation of interpenetrated structures. This phenomenon may occur when the pores are large enough to accommodate other independent networks, which can result in a reduction of the pore volume, surface area and the active sites availability.[78, 91]

Moreover, even though the majority of MOFs structures is composed by only one type of metal and ligand, more complex MOFs composed by mixed-metal SBUs or mixed-linkers have been reported, resulting in multiple functionalities within a single structure, called as multivariate MOFs (MTV-MOFs).[90] This proves that these materials are very adjustable and their properties can be tuned and enhanced towards several potential applications.[79, 92-93]

1.2.2. Framework Flexibility

MOFs can have numerous topologies with high crystallinity arising from all the potential combinations between inorganic SBUs and organic ligands, leading to extremely porous architectures. Their porosity and flexibility are the main characteristics responsible for most of the global interest towards several applications. In this context, S. Kitagawa, one of the pioneers on this subject, suggested that MOFs should be classified in three categories, which he named first-, second- and third-generations, regarding their structural behaviour in the presence or absence of guest molecules which is helpful to understand their framework flexibility (Figure 1.8).[95]

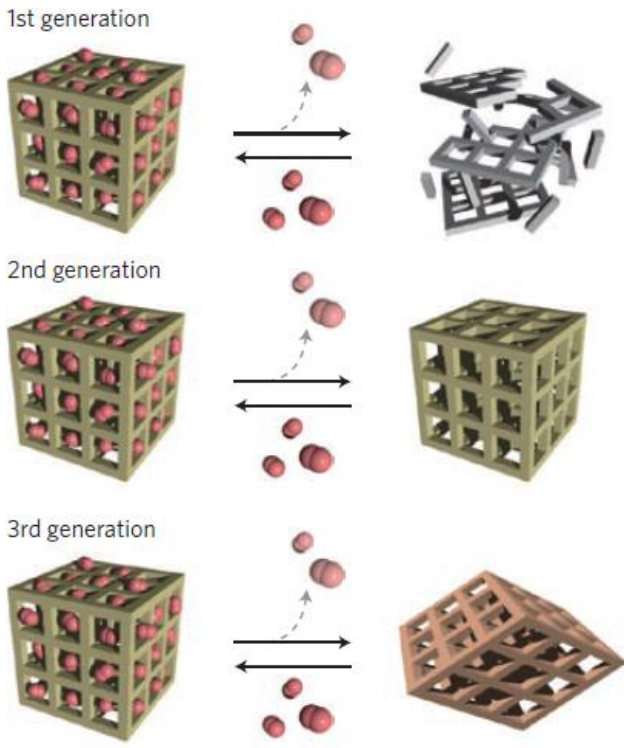

Figure 1.8 Representation of the three generations of MOFs according to S. Kitagawa.[94]

The first-generation concerns frameworks that do not possess permanent porosity due to their strong host-guest interaction dependence, which means that these structures only maintain their integrity in the presence of guest molecules and irreversibly collapses when they are removed, yielding an amorphous structure without porosity. Similar behaviour has often been observed in MOFs that contain charged frameworks and subsequently the pores are filled by counter ions. [80, 96]

The second-generation compounds are stable and robust frameworks with permanent porosity, which maintain their crystalline structure even in the absence of any guest molecules within the pores.[97] This behaviour is typical for neutral and zeolite-like MOFs (e.g. ZIFs, stands for zeolitic imidazolate frameworks) [96]

The third-generation represents a unique class of MOFs with flexible and dynamic framework, being able to reversibly change their structure, as a response to external stimuli, such as guest exchange, temperature, pressure, pH, light and electric or magnetic field, and are known as soft porous crystals or flexible MOFs.[80, 96] The structural transitions observed in these materials are often reversible crystal-to-crystal transformations, however, in some cases, the perfect crystallinity can be lost during the transition, resulting in reversible crystal-to-amorphous transformations.[94, 97]

The responsive behaviour of these materials has raised the interest of several researchers for potential applications such as chemical sensing, separation processes, drug release and catalysis. [98]

The MOFs flexibility can be determined by several factors, such as the type of SBU, the nature of the organic and inorganic moieties and, consequently, the framework topology. Discrete SUBs with flexible coordination geometry around the metal ion, rod-like SBUs with 1D square-shaped pore channels or frameworks composed by flexible organic linkers are some of the most prominent structural components found on flexible MOFs, owing to their high degree of flexibility.[74, 98]

The flexibility of the framework can be either global or local. When global flexibility is concerned, the entire backbone is dynamic and it is associated with substantial changes of the pore volume resultant from expansion or contraction movements, known as breathing effect. The local flexibility can be accomplished in MOFs that contain molecular switches implemented into the framework, such as organic linkers with the ability to modify their conformation or structure upon specific stimulus (e.g. photosensitive compounds).[74]

The most studied flexible MOFs with breathing properties are the MIL-53 series, first synthesized by the research group of G. Férey in 2002, with a framework composition of $[M^{3+}(OH)L]_n$, where M^{3+} = Fe, Al, Cr, Ga and L = terephthalate.[100] The flexible character of MIL-53 strongly depends on the nature of the metal centre.[101] The structure is composed of 1D rod-like SBUs interconnected by terephthalate linkers yielding a 3D framework with 1D square-shaped tunnels, resulting in a **sra** net topology. The breathing behaviour of MIL-53 is due to the rotation of the carboxylate groups around the O–O axis, in a “kneecap” motion, assisted by rotation of the phenyl rings (Figure 1.9).[74, 89, 99]

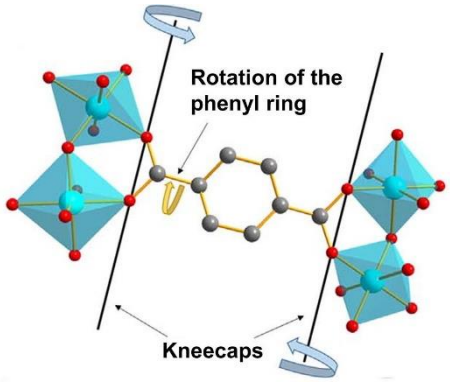

Figure 1.9. Schematic representation of the “kneecap” motion and the rotation of the organic linker responsible for the breathing effect of MIL-53 structure. Adapted from[99].

According to different external stimuli exposure, three different variants of MIL-53 are observed, such as as-synthesized (*as*), large pore (*lp*) and narrow pore (*np*) (Figure1.10).[74, 99] In the MIL-53-*as* form, the pores are occupied by disordered molecules of neutral terephthalic acid which when removed, upon heating at high temperature, lead to a structural transition to its expanded empty form, MIL-53-*lp*.[80, 102] By cooling in air, water molecules can be trapped in the pores, which induce a drastic contraction of the framework, due to strong hydrogen bonding interactions established between water guest molecules and the carboxylate groups of the MOF backbone, leading to the MIL-53-*np* form.[102] This structural transition is fully reversible when water is involved, since both, the inorganic SBU and the organic linker maintain their integrity. However, the framework reveals to be strictly inactive during the exchange of water by other solvents, such as acetone and ethanol, whereas DMF is immediately adsorbed, owing to the significantly stronger hydrogen bonds established with the framework backbone. This suggests that the MOF structure may exhibit some degree of selectivity during the guest exchange process.[80, 102]

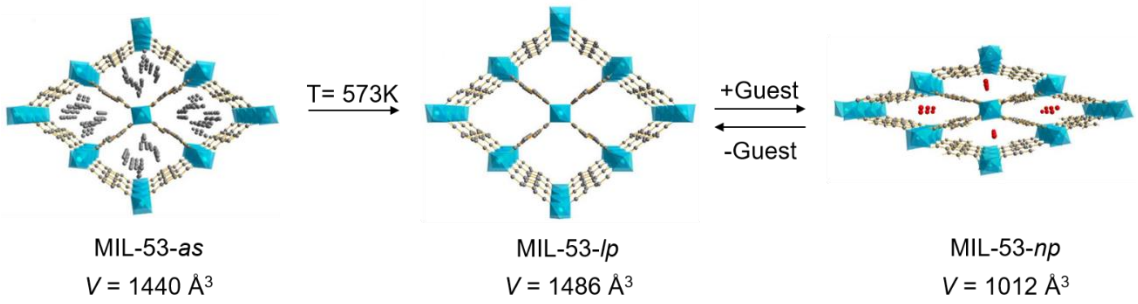

Figure 1.10. Schematic representation of the framework behaviour upon external stimuli and the respective pore volume variation. Adapted from[99].

1.3. MOF synthesis

Typically, the main goal in MOF synthesis is to identify and establish the appropriate reactional conditions that lead to the *in situ* formation of a specific type of SBU while avoiding the organic linker decomposition. This requirement is fundamental because even a slight variation in the synthetic conditions may result in the formation of different types of SBUs thus changing the overall structure and morphology of the outcome MOF.[75, 103] In order to identify the reaction parameters that have more influence in the final product (e.g. molar ratios of starting reactants, pH, solvent, presence of counterions, reaction time, temperature and pressure) serial and/or high-throughput methods are commonly used to facilitate the discovery of new compounds and to optimize the synthetic procedures of MOFs.[103-104]

1.3.1. Reaction conditions

The nature of the solvent is one of the most important parameters in MOF synthesis and must be carefully chosen. The choice of solvent is based on different aspects such as reactivity, redox potential, stability constant and solubility.[105] In addition to having direct influence on the solubility of both reactants and products, which is crucial in supersaturation and kinetics of crystal formation, solvent molecules can often act as directing agents during the self-assembly process. Depending on their steric hindrance, polarity and size it may lead to numerous structures with different dimensions, pore sizes and shapes, owing to their strong impact in the coordination behaviour of both inorganic and organic moieties, and consequently on the crystal morphology. Moreover, mixed solvent systems are often used in several MOF syntheses to enhance the crystal growth, due to the polarity difference between the solvent molecules and their ability to form different coordination environments.[69, 106-107] Solvents such as water, alcohols (e.g. methanol and ethanol), dialkyl formamides (e.g. DMF), acetone and acetonitrile are usually used in MOF synthesis.[80]

The reaction temperature is also a fundamental factor in MOF synthesis, which has a significant impact on the MOFs crystallization process. Typically, the increase of temperature leads to thermodynamically favoured products, whereas lower temperatures can result in kinetically favoured products. Moreover, the reaction temperature seems to influence the dimensionality of the inorganic subnetworks, and consequently the overall structure. Higher temperatures commonly lead to an increase in the final framework dimensionality. Thus, the choice of an appropriate reactional temperature can allow the formation of different supramolecular structures.[69, 80, 106-107]

Since the self-assembly of MOFs usually involve acid-base reactions, the pH of the reaction mixture is another important factor that can have a major impact on MOFs topology.[69] The deprotonation extent of the donor groups of the organic ligands is strongly dependent of the pH conditions, usually favoured by basic environments, which ultimately, determines the coordination modes of the ligands involved in MOF synthesis.[108] Furthermore, in some cases, the reaction kinetics can be controlled by altering the pH.[109] Several studies suggest that different crystal structures may arise due to the variation of the pH conditions, revealing that the increase of pH tends to favour the formation of networks with higher dimensionality. Nevertheless, at high pH values, the precipitation of metal salts $M(OH)_2$ can occur, depending on the metal ion and its concentration. Such conditions should be avoided, otherwise low dimensional structures may rise, due to the decrease of available metal ions in solution.[107]

1.3.2. Methods of synthesis

The synthesis of highly crystalline MOFs can be accomplished through a variety of different methodologies. The syntheses frequently occur in liquid-phase, in which the organic ligand and the metal salts are dissolved in pure solvents or solvent mixtures at specific molar ratios.[105, 110] Nevertheless, some researchers have also attempted solid-phase syntheses, due to their rapid and easy process.[105] However, it should be noted that depending on the method used to produce MOFs, the final products might exhibit different morphologies, particle sizes and size distributions, which can be reflected on the properties of the materials.[103, 107]

The conventional synthetic routes can be divided into two categories: solvothermal (or hydrothermal if the solvent is water) and non-solvothermal.[111] In general, MOFs are prepared under solvothermal conditions, which consists of reactions carried out in closed vessels, usually, at the boiling temperature of the solvent or above, under autogenous pressure, which enhances the solubility of the precursors involved in the reaction.[103] The reaction periods can range from a few hours to days. The major advantages of this method are the higher reaction yields of high-quality crystals in comparison to other methods and the possibility of precise control of size distribution and shape of the obtained products.[107, 110-111] However, these syntheses require specific equipment to reach high pressures, such as Teflon-lined stainless steel autoclaves.[108]

Non-solvothermal synthesis takes place below or at the boiling temperature of the solvent under ambient pressure.[103] Typically, these methods require highly soluble precursors and their concentrations must be adjusted in a way that the nucleation conditions are achieved, allowing the formation of MOF crystals.[103, 111] The concentration gradient can be promoted by different methods, such as slow solvent evaporation, layering of solutions, or slow diffusion of a solution of one component into another through a membrane or an immobilizing gel.[108] Once the critical nucleation concentration is exceeded, the growth of MOF crystals begins. Although these methods can be employed at room temperature and still produce high quality single crystals, their main drawback is the long reactional time required compared to other synthetic routes.[105]

Besides conventional routes, several alternative strategies have been applied to synthesize MOFs, in which the source of energy can be introduced into the system by microwave irradiation, an electric potential, mechanical force or ultrasonication, instead of using conventional electric heating (e.g. oven).

The microwave-assisted synthesis is a widely applied method to produce MOFs in shorter periods of time. Microwave irradiation is a very effective method of heating, which has the ability to achieve higher nucleation rates and accelerate the materials

crystallization, owing to the direct interaction of the radiation with the mobile electric charges, such as ions or polar solvent molecules in solution, which promote the collision between molecules and consequently increases the kinetic energy of the system.[103, 107] This method presents several advantages, including high heating efficiency, reduced reaction time and the possibility of synthesize nanosized MOFs with uniform size distributions and high purity.[110, 112-113]

More recently, electrochemical synthesis has been a promising method to quickly synthesize large amounts of MOF crystals at mild reaction temperatures.[112] In this method, metal ions are continuously introduced into the reaction medium, which contains dissolved organic linkers and electrolytes, through anodic dissolution instead of metal salts.[103, 107] The major limitation of this method is the undesirable accumulation of crystals near the electrodes during synthesis.[112]

Another method that has been used to synthesize MOFs is based on applying high-energy ultrasound waves into a reaction mixture, which stimulate chemical and physical changes in the system, without direct interaction with the molecules, through a cavitation process.[103] This relies on the formation, growth and instant collapse of bubbles in solution that creates local hot spots with high temperature and pressure due to the energy release.[105] The sonochemical synthesis is an energy-efficient and environmentally friendly method that offers reduced crystallization times.[110]

MOFs can also be synthesized by a solvent-free method known as mechanochemical synthesis, in which chemical reactions are induced by mechanical force that leads to the rupture of intermolecular interactions and the formation of new bonds between the precursors molecules (e.g. ball-milling).[103, 107] This method is also considered to be environmentally friendly because organic solvents can be avoided and can be performed at room temperature.[107] However, the MOF syntheses that follow this method usually present low reaction yields and difficulties in obtaining single crystals.[105]

1.4. MOFs as adsorbents for water contaminants

Over the last decade, MOFs have been studied for water purification, revealing excellent performances, as a result of their high adsorption capacities, fast adsorption kinetics and superior selectivity for both organic pollutants (e.g. pharmaceuticals, dyes, and pesticides) and inorganic pollutants (e.g. heavy metals, radionuclides and oxyanions) compared to conventional adsorbents, which pose MOFs as a promising next generation of high-performance adsorbent materials for environmental remediation.[61, 114]

The adsorption performance of MOFs is dictated by their crystalline structure, hydrophilicity, pore size and distribution, surface area, and surface chemistry.[61] These characteristics can be modified by different strategies to improve their affinity and

selectivity for specific analytes, such as, isoreticular or post-synthetic modifications (as mentioned in section 1.2.1.), or through the deliberate creation of structural defects, which can enlarge and/or introduce additional adsorption sites.[61, 115]

In order to understand the adsorption behaviour of MOFs towards water contaminants, it is essential to study their interactions. These are highly dependent on the nature of the adsorbate, physicochemical properties of MOFs and solution conditions (e.g. pH, temperature, ionic strength, coexisting substances in the solution and initial concentration of the adsorbate).[5, 61] Depending on the dominant interactions between MOFs and adsorbates, the adsorption process can undergo through several different mechanisms, such as electrostatic attraction, van der Waals forces, hydrogen bonding, acid-base interaction, diffusion, coordination, ion-exchange, chemical bonding, and π-π interaction/stacking (Figure 1.11). However, further research is needed to better understand the most significative interactions that affect the adsorption behaviour of MOFs and to improve their performances.[114, 116-117]

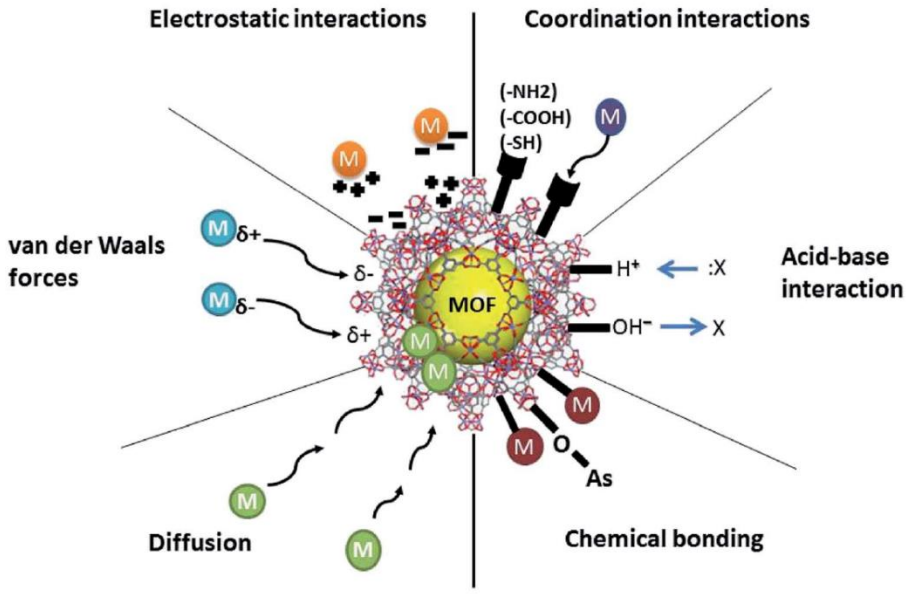

Figure 1.11. Schematic representation of some of the adsorption mechanisms of MOFs. Adapted from[117].

Despite the several advantages of using MOFs for water remediation compared to conventional adsorbents, there are still some challenges regarding their chemical stability in water, recovery and reusability, and lack of knowledge on their behaviour in complex solutions with multiple competitive substances. The water stability of MOFs is determined by thermodynamic and kinetic factors, which are correlated to the strength and lability of the metal-ligand coordination bonds that support the framework structure.[118-119] One strategy to improve their stability and produce robust structures is by reinforcing the interactions between the metal cations (Lewis acids) and the organic

ligands (Lewis bases).[120] According to the hard/soft acid-base (HSAB) principle, high-valence metal ions, such as Zr^{4+}, Al^{3+}, Fe^{3+}, tend to stablish strong interactions with carboxylate-type linkers, while divalent metal ions, such as Zn^{2+}, Co^{2+}, form stronger bonds with nitrogen-containing ligands.[5, 118]

In general, MOFs tend to form fine water suspensions, due to their small sized particles. Therefore, their recovery usually requires additional separation processes, such as filtration or centrifugation, which makes their large scale application still challenging.[121] The most promising approaches to overcome this limitation are based on the combination of MOFs with magnetic nanoparticles (MNPs) through different methods to give rise to MOF-based magnetic composites, or using pristine MOFs as templates to obtain magnetic porous carbon materials. As a result, both MOF-based materials can be easily separated and recovered from the medium by applying an external magnetic field, allowing an efficient, convenient and recyclable adsorption process.[122]

1.5. Magnetic MOF composites

The MOF-based magnetic composite materials can be prepared through a wide variety of methods (Figure 1.12). The impregnation method is the simplest strategy to obtain magnetic composites and can be implemented practically in any MOF. The MNPs and the MOF support are synthesized separately and mixed in a solvent solution under the influence of sonication/mechanical agitation to prevent aggregation. The magnetic composite is mainly formed due to electrostatic interactions between the MNPs and the surface of the MOF. However, due to the relatively weak interactions involved in the composite formation, the MNPs can be easily detached from the surface of MOFs and leached into the solution.[123-124]

The magnetic composites can also be produced through *in situ* growth methods which can be grouped into two categories: the ship-in-a-bottle and bottle-around-the-ship strategies. The first approach is based on the dispersion of pre-synthesized MOF crystals in a reactional mixture containing the MNPs precursors, allowing the growth of the MNPs in the presence of the frameworks. The MOFs selected for this method should be stable under the synthetic conditions of the MNPs.[121, 124] In the bottle-around-the-ship method, the preparation of the MOF crystals is carried out in the presence of preformed MNPs under reactional conditions similar to those used for the synthesis of the pristine MOFs (e.g. solvothermal processes), resulting in MOF composites with embedded MNPs.[121, 125]

The preparation of the magnetic composites can be also achieved through the layer-by-layer methodology, giving rise to core-shell structures. In this method, the surface of the MNPs is modified with suitable functional groups (e.g. thioglycolic acid), which

facilitate the growth of the MOFs around the particles and ensure stability for the formation of the core-shell composites. The inorganic and organic precursors of MOFs are added, alternately, to a solution with the functionalized MNPs, covering their surface with consecutive MOF layers. The thickness of the MOF coating is defined by the number of sequential cycles performed, which can be time-consuming.[121, 124]

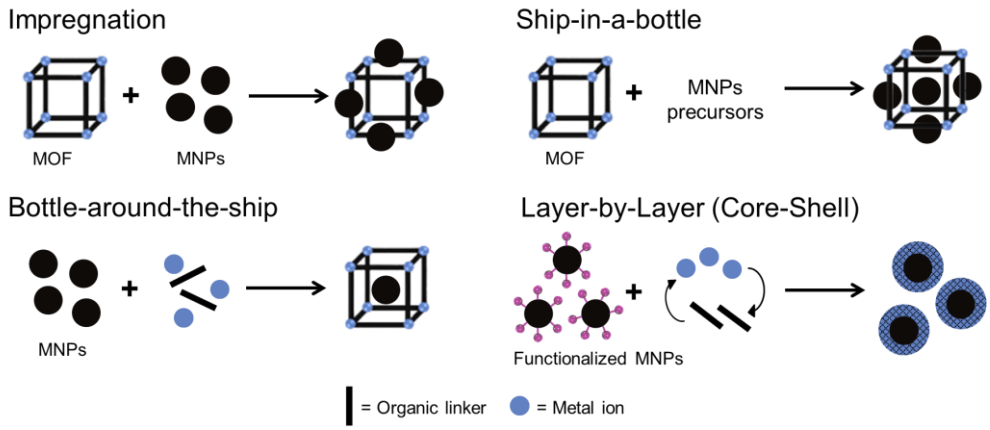

Figure 1.12. Schematic representation of the different methods for the preparation of the MOF-based magnetic composites.

1.6. MOF-derived porous carbons

In the past years, porous carbon materials have received much attention due to their promising potential for several applications, including catalysis, adsorption processes, energy storage and conversion, and chemical sensing. Recently, MOFs have been employed as precursors for the preparation of porous carbon materials due to their abundant carbon content, robust ordered structure, and high porosity.[126] Compared to traditional carbon materials, MOF-derived porous carbons (MDPCs) present unique advantages, such as ease and convenient syntheses without additional templates, tuneable pore sizes, large surface areas, controllable particle size and facile uniform doping of heteroatoms (usually element species as boron, nitrogen, phosphorus and sulphur) and metal/metal oxide particles in the carbon network (Figure 1.13). Also, MDPC materials have revealed enhanced conductive properties and superior chemical and thermal stability compared to the parent MOF precursors.[126-127]

In general, the preparation of MDPCs relies on the direct pyrolysis of pristine MOFs at high temperatures, usually 600 ºC or higher, under inert atmosphere (e.g. N_2 and Ar) to prevent the carbon oxidation.[128] The physicochemical properties of the MDPCs, such as particle morphology, porosity, and specific surface area, are determined by the parent MOF decomposition mechanisms, which are highly dependent of the framework structure and its stability, type of organic ligands, nature of the metal clusters, and experimental conditions (temperature, atmospheric conditions, heating ramp rate).[129]

During the pyrolysis process, the metal clusters present in the pristine MOFs tend to aggregate and produce metal oxides and/or metallic nanoparticles. If the metal centres contain elements such as Fe, Co or Ni, the carbonized products will present magnetic properties, giving rise to magnetic MDPCs.[121, 130] Under proper experimental conditions, the organic species not only tend to avoid the rupture and collapse of the MDPCs structure during the pyrolysis process, but also, ensure the homogeneous dispersion of the metal nanoparticles within the carbon matrix.[129]

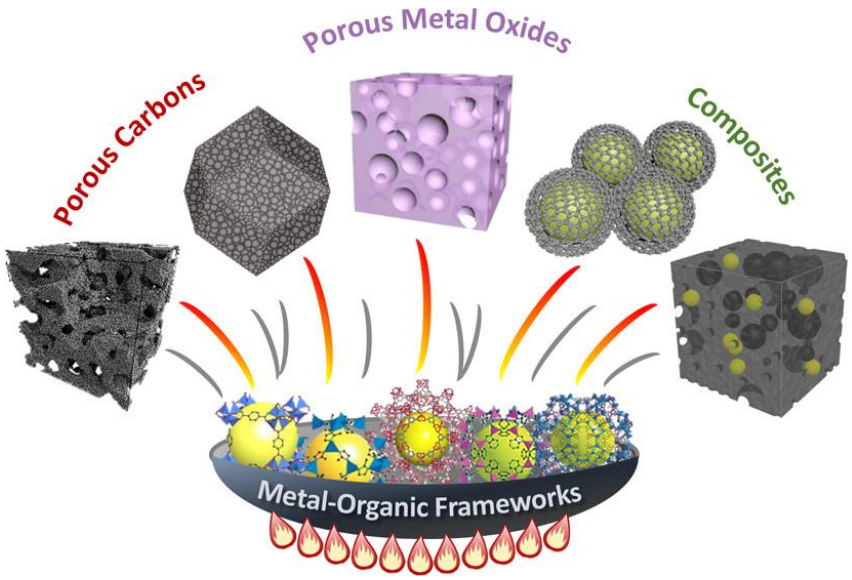

Figure 1.13. Schematic representation of different porous materials arising from MOF pyrolysis. Adapted from[129].

2. Experimental section

2.1. Materials and instrumentation

All the following solvents and chemical reagents were purchased from commercial suppliers and used without further purification.

The chemical reagents used in the synthesis of the materials were: iron(III) chloride hexahydrate [$FeCl_3 \cdot 6H_2O$, Sigma-Aldrich (≥ 99.0%)], iron(II) chloride tetrahydrate [$FeCl_2 \cdot 4H_2O$, Sigma-Aldrich (≥ 99.0%)], iron(II) sulphate heptahydrate [$FeSO_4 \cdot 7H_2O$, Sigma-Aldrich (≥ 99.0%)], cobalt(II) acetate tetrahydrate $(CH_3COO)_2Co \cdot 4H_2O$, Merck (≥ 98.0%)], 2-methylimidazole (Sigma-Aldrich, 99.0%), terephthalic acid [H_2BDC, Sigma-Aldrich (98.0%)], trimesic acid [H_3BTC, Sigma-Aldrich (95.0%)] and fumaric acid (Sigma-Aldrich, ≥ 99.0%). The solvents used were N,N-dimethylformamide [DMF, Fisher (≥ 99.5%)], ethanol [EtOH, Fisher (≥ 99.8%)] and tetramethylammonium hydroxide solution, 25 wt.% in H_2O (TMAOH, Sigma-Aldrich).

In the adsorption experiments, the copper ion solutions with initial concentration ranging from 5.00-20.0 mg/L were prepared using a copper standard solution (Cu 1000 mg/L, in 0.5 mol/L HNO_3) for Atomic Absorption Spectroscopy (AAS) purchased from PanReac AppliChem, while the copper ion solutions with initial concentrations ranging from 30.0 to 800 mg/L were prepared using copper(II) nitrate trihydrate ($Cu(NO_3)_2 \cdot 3H_2O$, ≥ 99.0%) acquired from Sigma-Aldrich.

The pH was adjusted using diluted solutions of hydrochloric acid (HCl, ~37%) and sodium hydroxide (NaOH) obtained from Fisher and pronalab, respectively. All solutions were prepared using double-deionized water.

The pH measurements were carried out in Hatch sensION™ + pH3 pH meter with a sensION + 5010T pH electrode. The calibration of the instrument was performed using buffer solutions at pH 4.00, 7.00 and 10.00.

Dynamic Light Scattering and Electrophoretic Light Scattering (DLS/ELS) studies were performed using Nano Zetasizer ZS instrument from Malvern with a monochromatic laser with λ = 633 nm (detector position was at 173º relative to the laser). Experiments were carried out using DTS1070 cells at 25 ºC.

2.2. MOFs synthesis

Throughout this project, five different MOFs were synthesized, which four of them were iron-based (MIL-100(Fe), MIL-88A(Fe), MIL-88B(Fe) and MIL-53(Fe) and one was cobalt-based, ZIF-67(Co). In Table 2.1 are summarized both organic and inorganic components of each MOF as well as the respective SBU and overall framework structure (crystal properties imported from CIF files reported in the literature[131-135])

Table 2.1. Summary of the metal centres, chemical structure of the organic precursors, SBUs and the respective framework structure of each MOF prepared.

MOF	Metal centre	Organic linker	SBU[90]	Structure
MIL-100(Fe)	Fe^{3+}	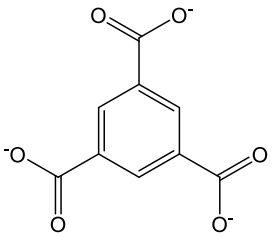	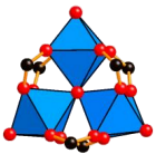	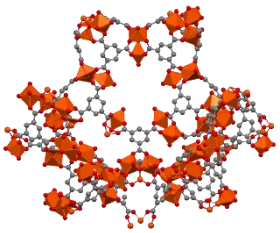
MIL-88A(Fe)		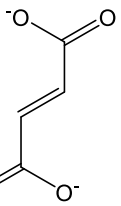		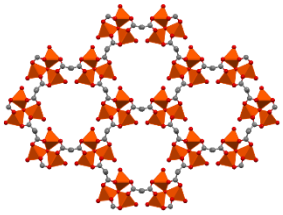
MIL-88B(Fe)		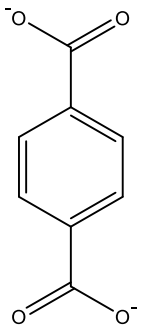		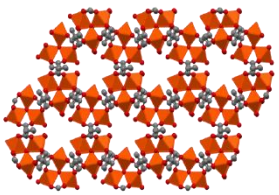
MIL-53(Fe)			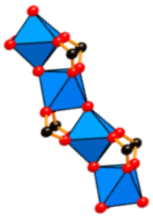	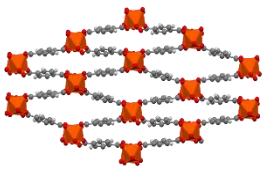
ZIF-67(Co)	Co^{2+}	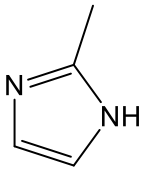	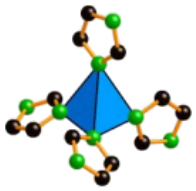	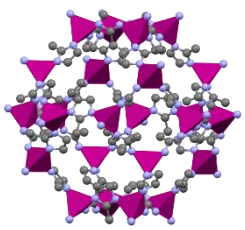

2.2.1. MIL-100(Fe)

The MIL-100(Fe) synthesis was adapted from a previously reported procedure.[136] Two different solutions were prepared separately at room temperature and under magnetic stirring. Solution 1 was prepared by mixing trimesic acid (2.50 mmol; 0.525 g) and NaOH (7.50 mmol; 0.300 g) in deionized water (20.00 mL) and solution 2 was prepared by dissolving $FeCl_4 \cdot 4H_2O$ (3.75 mmol; 0.745 g) in deionized water (20.00 mL). When both solutions became completely clear, solution 1 was added dropwise to solution 2 under stirring using a dropping funnel and the resulting solution was kept under vigorous stirring for 4h at room temperature. When the two solutions were mixed, the immediate formation of a green solid could be observed that slowly turned to yellowish-brown during the reaction time indicating the crystallization of the MOF. The formed solid was recovered by centrifugation at 6000 rpm for 15 min and then washed 3 times with deionized water and once with ethanol to remove free organic linker molecules. The as-synthesized solid was dried at room temperature in a desiccator over silica gel.

2.2.2. MIL-88A(Fe)

MIL-88A(Fe) was synthesized by a hydrothermal process based on the literature.[137-138] In a Teflon container, $FeCl_3 \cdot 6H_2O$ (2.00 mmol; 0.541 g) was firstly dissolved in ultrapure water (10.00 mL) under magnetic stirring and followed by the addition of fumaric acid (2.00 mmol; 0.232 g) and the reactional mixture was stirred for 1 h at room temperature to completely dissolve the organic linker. Next, the Teflon-liner was placed into a stainless-steel autoclave, sealed and kept in a preheated oven at 85 ºC for 24 h. After that, the autoclave was allowed to cooled down naturally to room temperature and the obtained orange solid was recovered by centrifugation at 6000 rpm for 15 minutes and then washed 2 times with deionized water and 3 times with ethanol to remove free organic linker molecules. The material was dried at 100 ºC under reduced pressure (175 mbar) overnight.

2.2.3. MIL-88B(Fe)

MIL-88B(Fe) was synthesized by a solvothermal process following an adapted protocol from the literature.[139] In a Teflon container $FeCl_3 \cdot 6H_2O$ (2.00 mmol; 0.541 g) was dissolved in DMF (10.00 mL) under magnetic stirring and then terephthalic acid (2.00 mmol; 0.332 g) and an aqueous solution of NaOH of 2 mol/dm^3 (800 µL) were added to the mixture which was stirred for 1 h at room temperature to completely dissolve the precursors. Then, the Teflon-liner was placed into a stainless-steel autoclave, sealed and kept in a preheated oven at 100 ºC for 12 h. After the heat treatment, the autoclave was allowed to cool down naturally to room temperature and the orange powder was

recovered by centrifugation at 6000 rpm for 15 minutes and washed several times with deionized water and ethanol to remove the solvent and/or free organic linker molecules. The solid was dried at 60 ºC under reduced pressure (175 mbar) overnight.

2.2.4. MIL-53(Fe)

MIL-53(Fe) was prepared by a solvothermal process following previously reported works.[140-141] $FeCl_3 \cdot 6H_2O$ (1.00 mmol; 0.271 g) was mixed with DMF (5.00 mL) in a Teflon container and when it was completely dissolved, terephthalic acid (1.00 mmol; 0.166 g) was added to the solution and the mixture was stirred for 1 h at room temperature. The Teflon container was placed into a stainless-steel autoclave, sealed, and kept in a preheated oven at 150 ºC for 12 h. After the heat treatment, the autoclave was allowed to cool down naturally to room temperature and the solid was recovered by centrifugation at 6000 rpm for 15 minutes. To remove the solvent molecules, the obtained yellow powder was resuspended in 200 mL of deionized water for 24 h followed by centrifugation at 6000 rpm for 15 minutes and dried at 60 ºC under reduced pressure (175 mbar) for 24 h.

2.2.5. ZIF-67(Co)

ZIF-67(Co) was synthesized by a solvothermal process following a reported method in the literature.[142] First, $Co(Ac)_2 \cdot 4H_2O$ (1.33 mmol; 0.331 g) was dissolved in ethanol (10.00 mL) under magnetic stirring and then 2-methylimidazole (4.00 mmol; 0.328 g) was added to the solution. The reactional mixture was stirred for 1 h to completely dissolve the precursors at room temperature. Thereafter, the Teflon-liner was placed into a stainless-steel autoclave, sealed, and kept in a preheated oven at 130 ºC for 72 h. After the heat treatment, the autoclave was allowed to cool down naturally to room temperature and the as-synthesized material was recovered by centrifugation at 6000 rpm for 15 minutes and washed with ethanol several times. Finally, the dark purple solid was dried at 150 ºC for 8 h under reduced pressure (175 mbar).

2.3. Magnetic materials synthesis

2.3.1. Magnetic nanoparticles (MNPs)

The nanoparticles were synthesized via a co-precipitation method adapted from the literature.[143] Two solutions were prepared separately, $FeCl_3 \cdot 6H_2O$ (8.00 mmol; 2.162 g) and $FeSO_4 \cdot 7H_2O$ (4.00 mmol; 1.112 g) were dissolved in an aqueous solution of HCl of 0.50 mol/dm^3 (5.00 mL), respectively. When the iron salts were completely dissolved,

the two solutions were mixed and then added dropwise to an aqueous solution of NaOH 1.50 mol/dm^3 (100.0 mL) under vigorous mechanical stirring and continued for 30 minutes at room temperature. The colour of the suspension immediately turned black which is a characteristic feature of magnetite (Fe_3O_4) particles. The precipitated solid was collected from the reactional mixture by magnetic separation, applying an external magnet (Figure 2.1), and then the supernatant solution was removed by decantation. The magnetic product was washed 2 times with deionized water (50.0 mL) and finally, dispersed in a stabilizing medium of TMAOH (25.00 mL) to avoid the MNPs aggregation. The concentration of the MNPs dispersion was approximately 3 g/L.

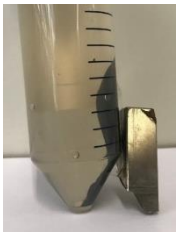

Figure 2.1. Magnetic separation of the MNPs by an external magnet.

2.3.2. Magnetic MIL-53(Fe) composite

The magnetic composite was prepared by a solvothermal process following a bottle-around-the-ship approach based on a reported work.[140] In a glass vial, 100 µL of MNPs were transferred from the MNPs suspension and washed 3 times with deionized water to remove the TMAOH solution. Then, $FeCl_3 \cdot 6H_2O$ (1 mmol; 0.270 g) dissolved in DMF solution (5.00 mL) was added to the MNPs and the suspension was sonicated for about 5 minutes. Afterwards, the terephthalic acid (1 mmol; 0.166 g) was added to the mixture and then again sonicated for 15 minutes. After sonication, the mixture was transferred to a Teflon-lined stainless-steel autoclave and heated up to 150 ºC for 12 h. After the heat treatment, the autoclave was allowed to cool down naturally to room temperature and the products were recovered by centrifugation at 6000 rpm for 15 minutes. In order to remove the solvent molecules, the solid was suspended in deionized water (200 mL) for 24 h and then collected again by centrifugation. The obtained powder was dried at 60 ºC for 24 h under reduced pressure (175 mbar). The products from this synthesis presented two different colours, yellow, similar to the as-synthesized MIL-53(Fe) powder, and red (Figure 2.2) Due to this difference, the materials were named MIL-53Y and MIL-53R, respectively, and characterized in separate.

Figure 2.2. Magnetic separation of (a) MIL-53Y and (b) MIL-53R by an external magnet.

2.3.3. ZIF-derived porous carbon

The material was prepared based on a procedure from the literature[144]. The as-synthesized ZIF-67(Co) powders (1.231 g) were divided in two porcelain combustion boats that were placed into a quartz tube which was kept inside a tubular furnace. The

powders were directly carbonized under a nitrogen flow, to avoid undesired oxidation of the material. The temperature inside the furnace was gradually increased from room temperature to 600 ºC at a heating rate of 5 ºC/min and the material was kept for 5 h at the target temperature. The obtained black powder was collected with no further treatment and denoted as ZIF-DPC (Figure 2.3).

Figure 2.3. Magnetic separation of ZIF-DPC by an external magnet.

2.4. Adsorption studies

2.4.1. Determination of the pH at point of zero charge (pH_{ZPC})

The pH_{ZPC} of each material that was applied in the adsorption studies was previously determined following an adapted procedure from the literature.[145] The experiments were performed in double deionized water with an adsorbent dosage of 1.00 g/L. The initial pH of each solution was adjusted, before adding the adsorbent, at different pH values, ranging from 2.00 to 10.00, using HCl and NaOH solutions of 1.00 mol/dm^3. The suspensions were left under magnetic stirring for 48 h at room temperature. Afterwards, the pH of each suspension was measured and the difference between the final and initial pH (ΔpH) was calculated and plotted as a function of the initial pH. The pH_{ZPC} values were obtained at the point where ΔpH was equal to zero, this is, when the curve intersected the xx axis.

2.4.2. Effect of adsorbent dosage

The experiments to study the effect of adsorbent dosage were performed in glass vials containing 10.00 mL of Cu (II) metal aqueous solution with initial concentration of 10.0 mg/L and different adsorbent dosages, ranging from 0.25 – 1 g/L. The suspensions were kept under magnetic stirring for 3 h at room temperature. During this period, the pH was monitored, and small additions of HCl and NaOH solutions of 1.00 mol/dm^3 were used to maintain the pH at 5.50. Thereafter, the adsorbent was separated from the solution by centrifugation at 6000 rpm for 10 minutes and 1% (v/v) of HNO_3 was added to the recovered solution and stored at 4 ºC for posterior quantification of the remaining copper concentration by AAS. All experiments were performed in duplicate.

The adsorption capacity of the adsorbent and the corresponding removal efficiency were calculated by the following expressions (Eq. 1 and 2), respectively:

$$q = \frac{c_0 - c_e}{m} \times V \quad (1)$$

$$\% \, Removal = \frac{(c_0 - c_e)}{c_0} \times 100 \quad (2)$$

where q is the amount of Cu(II) adsorbed per gram of adsorbent (mg/g), c_0 and c_e are the initial and the equilibrium concentrations of Cu(II) ions in solution (mg/L), m is the mass of adsorbent used (g), and V is the volume of the solution (L)

2.4.3. Effect of pH

The assays for the analysis of the effect of solution pH were carried out in glass vials with 10.00 mL of Cu (II) metal solution with initial concentration of 10.0 mg/L containing a fixed amount of adsorbent material (10.0 mg). The pH of the suspensions was adjusted to 3 different values, 3.50, 4.50 and 5.50, using HCl and NaOH solutions of 1.00 mol/dm^3. The suspensions were kept under magnetic stirring for 3 h at room temperature and the pH was controlled to the desired pH value by small additions of acid or base solutions. Subsequently, the adsorbent was separated from the solution by centrifugation at 6000 rpm for 10 minutes and the solution was stored at 4 ºC with 1% (v/v) of HNO_3 for posterior quantification of copper concentration by AAS. All experiments were performed in duplicate.

2.4.4. Adsorption kinetics

In order to evaluate the adsorption rate as function of the time contact for each adsorbent material, kinetic experiments were carried out in glass vials, where 10.00 mL of Cu(II) solution with initial concentration of 10.0 mg/L were mixed with 10.0 mg of adsorbent material and stirred at room temperature during different periods of time up to a maximum of 8 h. The initial pH of the suspensions was adjusted with HCl and NaOH solutions of 1.00 mol/dm^3 at 5.50 and readjusted over time when required. Each sample corresponded to a different contact time and were extracted at predefined time intervals, respectively. The adsorbent was recovered by centrifugation at 6000 rpm for 10 minutes and 1%(v/v) of HNO_3 was added to each solution and stored at 4 ºC for subsequent copper ion quantification by AAS. All experiments were performed in duplicate.

The study of the adsorption kinetic is essential to predict the removal rate of the adsorbate and provides some information about the mechanisms that control the adsorption processes. To accomplish this, mathematical fitting models are used, which the most common ones are the pseudo-first order (PFO) and the pseudo-second order (PSO) models.[146]

The PFO and PSO kinetic models are represented by the following expressions (Eq. 3 and 4):

$$q_t = q_e(1 - e^{-k_1 t}) \quad (3)$$

$$q_t = \frac{q_e^2 k_2 t}{1+q_e k_2 t} \quad (4)$$

where q_t and q_e are the amount of Cu(II) adsorbed per unit of mass of adsorbent for a contact time t and at equilibrium (mg/g), respectively. k_1 (min^{-1}) is the rate constant of the PFO model and k_2(g/(mg.min)) is the rate constant of PSO model.

2.4.5. Adsorption Equilibrium

The equilibrium experiments were carried out in glass vials containing 10.00 mL of Cu(II) ion solution with different initial concentrations, ranging from 10.0 to 800 mg/L, and 10.0 mg of adsorbent material. Based on the outcome of the kinetic experiments, the samples were placed under magnetic stirring for 6 h, at room temperature, to ensure that the equilibrium had been attained for every concentration. The pH of the suspensions was also adjusted to 5.50 and thoroughly controlled during the course of the experiments by small additions of acid and base solutions. Afterwards, the adsorbent material was separated from the solution by centrifugation at 6000 rpm for 10 minutes and 1%(v/v) of HNO_3 was added to each sample and stored at 4 ºC for posterior Cu(II) quantification by AAS. All experiments were performed in duplicate.

The behaviour of an adsorption process in equilibrium can be represented by isotherm models, which mathematically describe the relationship between the amount of adsorbate adsorbed to the solid phase surface and its remaining concentration in solution, at a given temperature. The Langmuir and Freundlich isotherms are the most common models applied to explain adsorption processes in liquid phases.[59, 147]

The Langmuir isotherm model can describe both chemical and physical adsorption processes, assuming that all adsorption sites are well-defined, homogeneous, and each one has equal affinity to interact with only one adsorbate molecule, creating a monolayer that completely covers the adsorbent surface. Also, the rate of adsorption and desorption are assumed to be proportional to the number of vacant and occupied adsorption sites, respectively, and the interactions between adjacent adsorbate molecules are not considered.[147-149] This model is described by the following equation (Eq. 5):

$$q_e = \frac{q_{max} K_L c_e}{1+K_L c_e} \quad (5)$$

where q_{max} (mg/g) is the amount of adsorbate required to form a complete monolayer per unit of mass of the adsorbent, reflecting the maximum adsorption capacity of the material, K_L (L/mg) is the Langmuir constant and c_e is the concentration of adsorbate at equilibrium (mg/L).

Moreover, it is possible to evaluate the feasibility of a given adsorption process through the Langmuir isotherm by a dimensionless constant known as separation constant or equilibrium parameter, R_L, and can be expressed by the following equation (Eq. 6):

$$R_L = \frac{1}{1+K_L \times c_0} \quad (6)$$

where K_L is the Langmuir constant (L/mg) and c_0 is the initial concentration of the adsorbate (mg/L). The value of R_L indicates whether the type of adsorption process is unfavourable (R_L > 1), linear (R_L = 1), irreversible (R_L = 0) or favourable (0 < R_L < 1).

The Freundlich isotherm is an empirical model usually applied to describe multilayer adsorption processes that occur on adsorbents with heterogeneous surface and irregular distribution of the adsorption sites affinities to the adsorbate molecules. Moreover, this model takes into account the repulsive interactions between the adsorbed molecules.[147, 149-150] The Freundlich isotherm model is represented by the following expression (Eq. 7):

$$q_e = K_f c_e^{1/n} \quad (7)$$

where K_f [((mg/g).(mg/L))$^{1/n}$] and n are Freundlich constants related to adsorption capacity and adsorption intensity, respectively. The magnitude of $1/n$ can be associated with the viability of the adsorption process, while the n value can provide information regarding the nature of the adsorption, whether it is linear (n = 1), unfavourable (n < 1) or favourable (n > 1).

2.4.6. Desorption and recycling studies

The desorption experiments were performed with 10.0 mg of the adsorbent material after adsorption studies in 10.0 mg/L of Cu(II) ions solutions, with HCl solution 0.01 mol/L as the desorption solvent at a solid/liquid ratio of 1.00 g/L. The suspensions were kept under magnetic stirring for 24 h at room temperature. Then, they were separated by centrifugation at 6000 rpm for 10 min. The adsorbent materials were dried under vacuum at 60 ºC overnight for posterior use in consecutive adsorption cycles. The supernatant was collected and stored at 4 ºC with 1% (v/v) of HNO_3 for posterior quantification of the Cu(II) ion concentration in solution by AAS. The desorption efficiency was determined from the relation between the adsorbed concentration of Cu(II) ions, c_{ad} (mg/L) and its equilibrium concentration in solution, c_e(mg/g), expressed by the following equation (Eq. 8):

$$\%\, Desorption = \frac{c_e}{c_{ad}} \times 100 \quad (8)$$

The recycled adsorbents were reused to extract Cu(II) ions in solutions with initial concentration of 10.0 mg/L under the same experimental conditions as the equilibrium studies using 1.00 g/L of adsorbent dosage. The adsorption capacity and removal percentage were calculated by the equations 1 and 2, respectively. All experiments were performed in duplicate.

2.5. Experimental techniques

2.5.1. Powder X-Ray Diffraction (PXRD)

X-ray diffraction is a powerful and effective non-destructive technique used to characterize solid materials, providing detailed information about their crystallographic structure at the atomic or subatomic scale (10^{-9}-10^{-11} m). X-rays are a high-energy electromagnetic radiation, that are generated by the collision of high-speed electrons on a metal target (usually Cu and Mo), that were previously accelerated by a high-voltage field under vacuum conditions. The rapid deceleration of the electrons when they collide on the surface of the target allows the kinetic energy of the electrons to be converted into X-ray radiation.[151]

In a typical PXRD experiment, the crystalline specimen is placed on the sample holder, between the X-ray beam source and the detector, and illuminated with a wavelength-shiftable monochromatic beam of X-rays, characteristic of the metal anode.

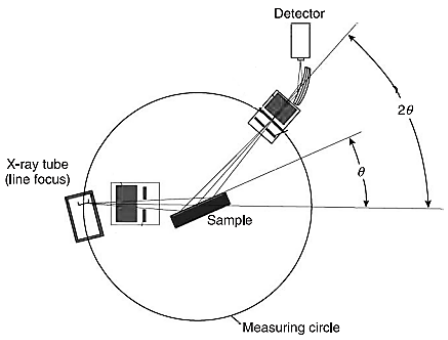

Figure 2.4. Geometric arrangement of X-ray diffractometer. Adapted from[151].

In general, the X-ray source and detector move in synchronized motion around the specimen, recording signals related to the diffraction intensities in a range of 2θ angle. (Figure 2.4) Thus, unique diffraction patterns characteristic of the atomic structure of the sample are generated. Given that the wavelength of the X-ray radiation is in the same order of magnitude as the interatomic plane distances, the incident beam will interact with the sample, inducing interference that can be destructive or constructive, either cancelling or reinforcing the diffracted waves, respectively. For X-ray diffraction to occur, the elastically scattered electrons from the lattice planes must interact constructively, which only occurs when the Bragg's Law is satisfied (Figure 2.5).[151-152]

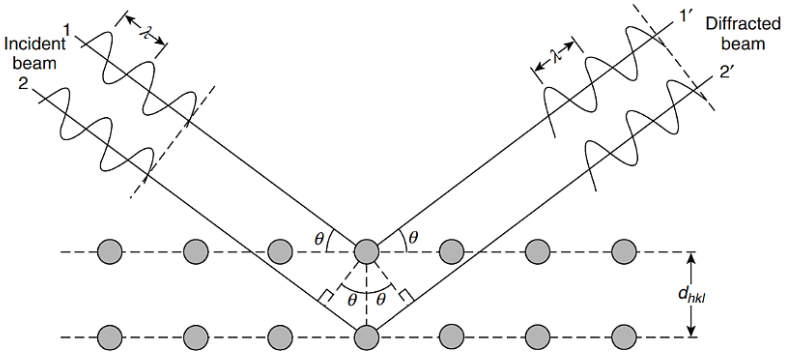

Figure 2.5. Schematic representation of X-ray beam diffraction from a pair of adjacent atoms in different lattice planes. Adapted from[151].

This law states that constructive interferences happen when the path difference between the diffracted beams equals to one or multiple wavelengths of the incident X-rays, and can be expressed by the following equation (Eq. 9):

$$n_i\lambda = 2d_{hkl}\sin\theta \tag{9}$$

where n_i is the integer number, λ the radiation wavelength, d_{hkl} the atomic spacing between crystallographic planes associated with a given Miller index (hkl) and θ is the angle between incident X-ray beam and the crystallographic plane that causes diffraction.

Powder X-ray diffraction (PXRD) patterns were obtained at room temperature on a Rigaku's Smartlab diffractometer operating with a Cu radiation source (λ = 1.540593 Å) and in a Bragg-Brentano θ/2θ configuration (45 kV, 200 mA). Intensity data were collected by a step-counting method (step 0.01°), in continuous mode, in the 2 ≤ 2θ ≤ 50° range. For Fe_3O_4 nanoparticles and related magnetic materials, diffraction patterns were acquired until 2θ = 80º. All experiments were performed at Faculty of Sciences of the University of Porto.

2.5.2. Fourier Transform Infrared Spectroscopy (FT-IR)

Infrared (IR) spectroscopy is a type of absorption spectroscopy that is widely used to provide information about the molecular composition and interactions within a compound. The sample is irradiated in the vibrational IR region of the electromagnetic spectrum, that ranges from wavelengths of 2.5 to 25 µm, corresponding to 4000 – 400 cm^{-1} in terms of wavenumbers ($\bar{\nu}$), that is directly proportional to the frequency and energy. The energy of IR photons is insufficient to cause electronic excitation. Nonetheless, it can result in molecular vibrational excitation if their energy matches the energetic difference between the excited and ground energy state associated with a given vibrational mode among two atoms, increasing the amplitude of the vibrational

motions of the covalent bonds within a molecule. However, only those bonds that have an electric dipole moment that changes as a function of time at the same frequency as the incoming radiation, will absorb IR radiation.[151, 153]

Each molecule has a defined number of different vibrational modes, that are dependent on the degrees of freedom present in a molecule. In case of the linear molecules, there are 3*N*-5 normal modes of vibration and in the non-linear molecules are 3*N*-6 modes, where *N* is the number of atoms of the molecule. These vibrational modes can be broadly divided into two types: stretching, if there is a change in the length of the bonds, or bending, if the angle between two bonds is changed, as illustrated in Figure 2.6. Each one of these vibrational modes absorb at different frequencies of vibration, stretching vibrational modes usually absorb at higher frequencies than bending vibrations.[151]

In order to obtain an IR spectrum of a given sample, a beam of IR light containing all frequencies of interest pass through the sample, and the amount of transmitted radiation is detected. The signal received constitutes an interferogram of all transmitted wavelengths of the incident IR radiation and it is converted into an IR spectrum by the Fourier transform, giving a plot of transmitted light intensity versus wavenumber.[151, 153]

Since every bond presents a different frequency of vibration, which is also dependent on the molecular environment that it lies in, the position of all spectrum vibrational bands and their relative intensities are characteristic of a given molecular species. Therefore, this technique can be used to identify the presence of a given molecule in a sample, accomplish through comparison/overlap of the obtained sample IR spectrum with previously reported IR absorption bands of a specific substance.

FT-IR absorption spectra were obtained on a Jasco FT/IR-460 Plus spectrometer, using KBr pellets. Spectra were collected in the range 400–4000 cm^{-1}, using a resolution of 4 cm^{-1} and 64 scans. All experiments were performed at Faculty of Sciences of the University of Porto.

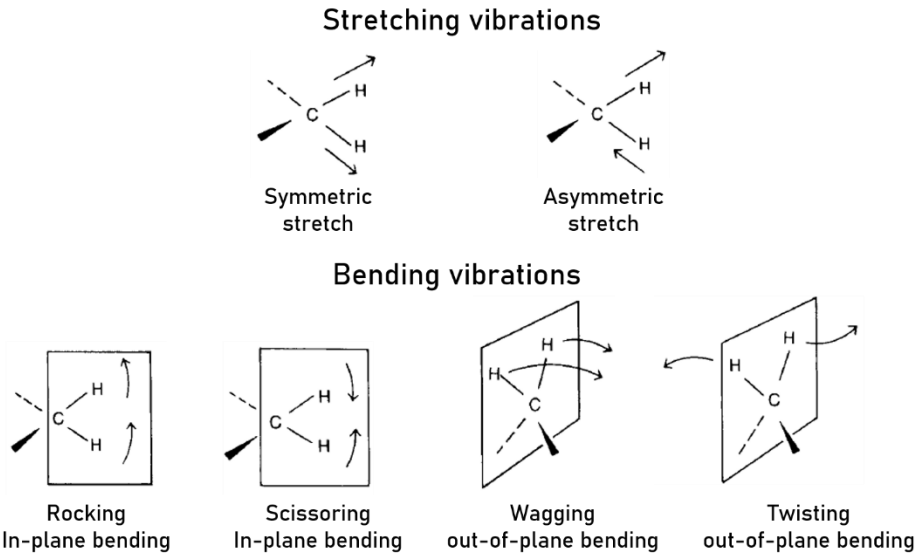

Figure 2.6. Representation of the different types of stretching and bending vibrations. Adapted from[153].

2.5.3. Scanning Electron Microscopy and Energy Dispersive X-ray Spectroscopy (SEM/EDS)

SEM is an imaging technique that is widely used to characterize the surface and structure of a given material, providing useful information about the topology, morphology, and particle size, through quasi-3D high-resolution images with a maximum resolution in the nanometre scale. Moreover, SEM instruments are usually coupled with an energy dispersive X-ray spectrometer (EDS), which enables the evaluation of the chemical composition and its distribution over the specimen surface.[151-152]

The working principle of SEM is based on scanning a specimen surface with a focused beam of electrons. The electrons are generated from an electron gun and accelerated by an electric potential to pass through a combination of electromagnetic lenses, including condenser and objective lenses, to acuminate and focus the electron beam as a fine probe with a spot size diameter at the nanometre scale, as illustrated in Figure 2.7. The probe is operated by a sequential deflection system that moves the electron beam over a defined area of the specimen, which is usually placed in high vacuum chambers to avoid undesired dispersion of the electron beam. When the high-energy beam of electrons interacts with the surface specimen, it produces different types of signals, such as secondary electrons, backscattered electrons, and characteristic X-ray photons, that are collected by appropriate detectors and generate high-resolution point-to-point images, known as SEM micrographs, as well as, elemental spectra or maps.[151, 154]

The secondary electrons are generated by interaction of the (primary) beam electrons by inelastic scattering and provide valuable insights about the topology and

morphology of the specimen surface. On the other hand, backscattered electrons result from elastic scattering of the incident beam with the specimen. The number of backscattering electrons produced, and their intensity is related to the atomic number of the atoms, which provide useful information about the spatial distribution of different elements on the specimen surface. The X-rays are emitted from the surface of the specimen and have a specific wavelength that is characteristic for each element, since each one has a unique energy difference of electronic transitions between the excited and ground states. They are used to identify and determine the relative abundance of different elements in a defined area of the specimen. Also, X-rays can be combined with the secondary electrons to produce elemental distribution maps (EDS mapping).[151, 154]

In this work, SEM analyses were performed at ‘‘CEMUP – Centro de Materiais da Universidade do Porto’’ (Porto, Portugal), using a high-resolution environmental scanning electron microscope, FEI Quanta 400 FEG ESEM, coupled with an EDS, EDAX Genesis X4M. The average particle sizes presented were determined using the ImageJ software, measuring a total of 30 particles. Then, the arithmetic mean of the obtained values and the respective standard deviation were determined.

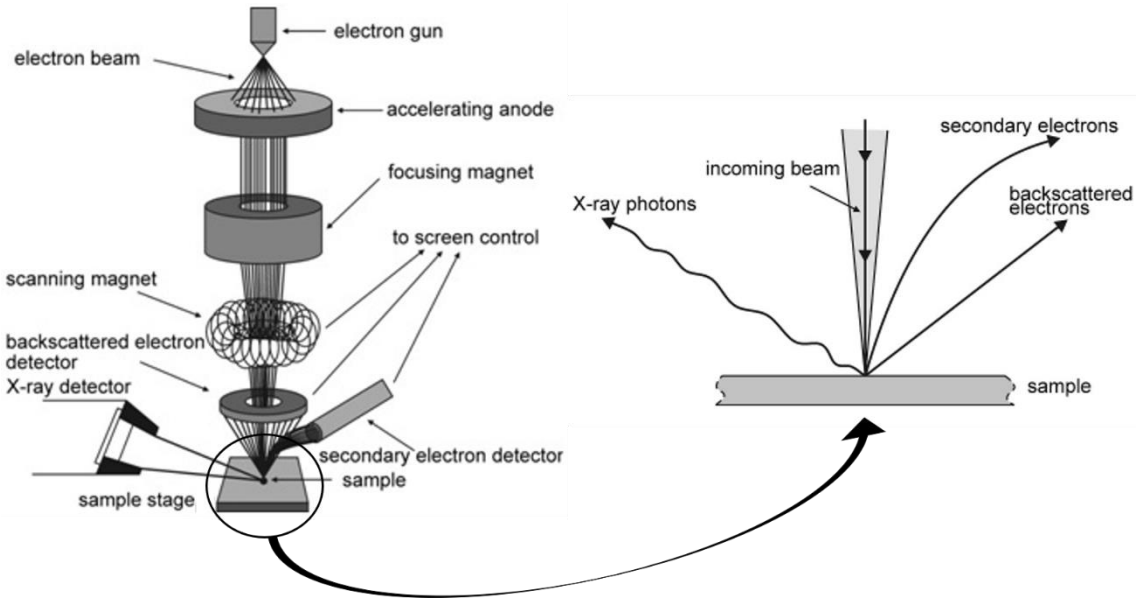

Figure 2.7. Schematic representation of the basic working principle of SEM (left) and the products of the electron-sample interactions (right). Adapted from[154]

2.5.4. Thermogravimetric Analysis (TGA)

TGA is an analytical technique used to evaluate the thermal stability of a given material and quantify volatile substances that may be present by measuring mass changes that occur as a function of temperature or time. Although this technique does not allow for undisputed identification of the substances that cause mass loss, one can assume by comparing the temperature at which the mass variation occurs with the

boiling temperatures of the compounds expected to be present in the sample. TGA can be either static (or isothermal), if the sample is maintained at constant temperature for a period of time, or dynamic (non-isothermal), if the temperature is changed over time at constant or variable rate.[152, 155]

In a typical TGA experiment, the mass change is monitored by a thermobalance, where 2-10 mg of sample are placed in a sample holder inside a furnace, with a programmable temperature control, and it is connected to a microbalance by a suspension wire, allowing a precise measurement of the mass variation (Figure 2.8). The thermal analyses can be either performed under inert (N_2 and dry Ar), or reactive atmospheres (O_2, H_2 and CO_2) depending on the experiment goals. Besides the temperature control, the gas flow and pressure in the furnace can be also adjusted.[151, 155]

The TG data collected from an experiment is compiled into a plot of mass or percentage of initial mass as a function of temperature or time, which is known as a TG curve. The slope variation in a TG curve is the main feature used to analyse mass changes. However, since in some cases the slope variation is not so notorious, the first derivative of the TG curve is determined and represented as DTG curve, in which the rate of the mass changes upon heating is plotted against temperature. The DTG curve does not contain any additional information other than the already obtained in the TG curve, however, it provides a more detailed interpretation of the experimental data, allowing the clear identification of the temperatures at which the mass losses are at its maximum.[151, 155]

The thermogravimetric analyses were performed in a Hitachi STA 7200 RV instrument, under inert atmosphere (200 mL/min N_2 flow rate), from room temperature to 800 ºC at a heating rate of 5 ºC/min. All experiments were performed at Faculty of Sciences of the University of Porto.

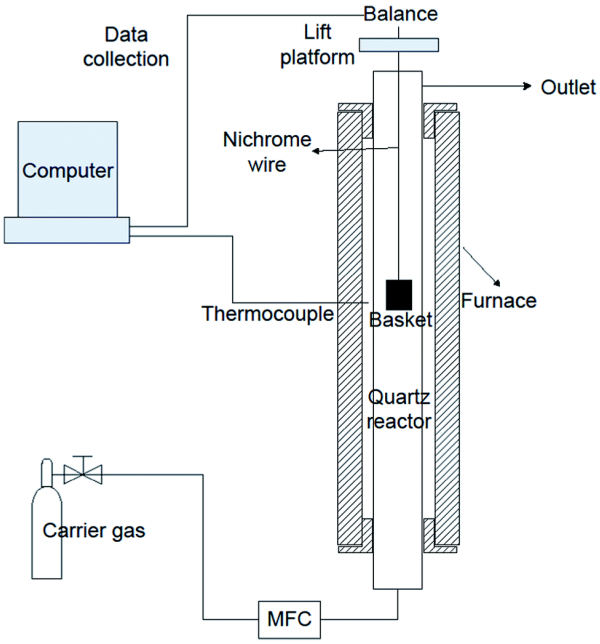

Figure 2.8. Schematic diagram of the basic step-up of a TGA instrument. Adapted from[156].

2.5.5. N_2 adsorption/desorption isotherms

Nitrogen adsorption is a well-established and widely used method to characterize porous materials, allowing the determination of their specific surface area and pore volume. These properties are assessed from the adsorption/desorption isotherms data, which consist of measuring the amount of physiosorbed/desorbed nitrogen as a function of pressure at constant temperature. The isotherms are usually recorded at cryogenic temperatures, which for nitrogen is at -196 ºC.[157]

In a typical N_2 adsorption/desorption experiment, the samples are first outgassed under vacuum at a given temperature, in order to remove any adsorbate molecules that may be trapped inside the porous material. In this step, the temperature at which the process is carried out must be carefully chosen, since high temperatures might cause to partial decomposition of the material, while low temperatures could lead to the incomplete outgassing of the sample, thus impairing the final outcome. After this stage is complete, the weighted sample cell is cooled down to -196 ºC and then a specific amount of nitrogen is introduced into the sample cell. From the moment that both pressure and temperature inside the cell are stable, the isotherm starts to be recorded until the adsorbent surface is completely covered. Thereafter, the nitrogen inside the sample cell is gradually removed and desorption cycle begins.[158]

According to IUPAC, the adsorption isotherms can be categorized in six different types, providing a direct classification of a given porous material based on the shape of the outcome isotherm (Figure 2.9).[157] Type I isotherms are given by microporous solids (pore size < 2 nm) with small external surfaces. Type II isotherms are normally obtained

by nonporous or macroporous materials (pore size > 50 nm) with unrestricted multilayer adsorption. Type III isotherms are not often seen in most materials, although it can occur when the adsorbate-adsorbate interactions are stronger than the adsorbate-adsorbent interactions. Isotherms of type IV are usually seen in mesoporous materials (pore size between 2 – 50 nm), featuring a monolayer-multilayer adsorption at lower relative pressures followed by capillary condensation in the mesopores at high pressures, causing the hysteresis loop upon desorption. The type V isotherms are observed for mesoporous materials that, as in type III, establish weak interactions with the adsorbate. Finally, type VI isotherms can be observed for materials with uniform surface, featuring a layer-by-layer adsorption type.[157-158]

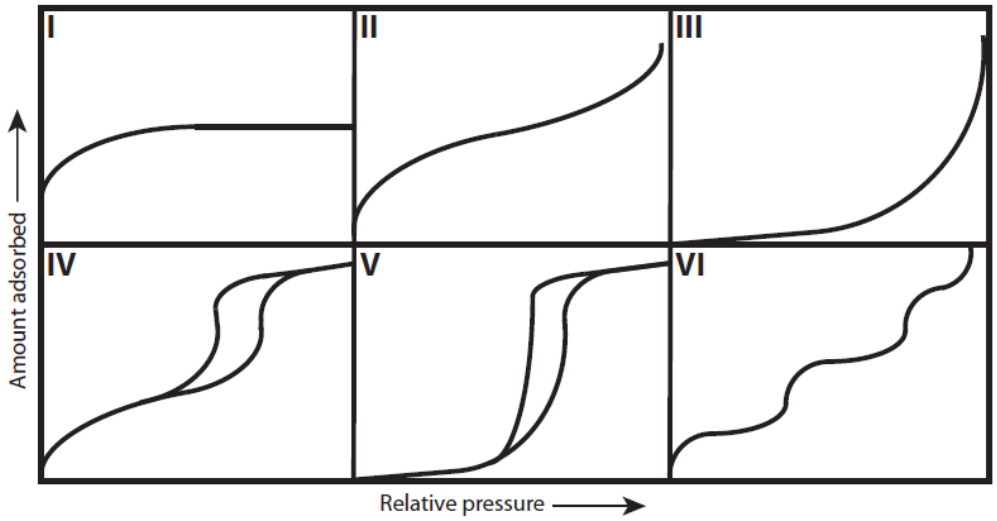

Figure 2.9. The six types of physisorption isotherms according to IUPAC. Adapted from[157].

The most common method used to determine the specific surface area is the Brunauer-Emmett-Teller (BET) theory, described by the following equation (Eq. 10):

$$\frac{p}{V\times(p^0-p)} = \frac{1}{V_m\times C_{BET}} + \frac{C_{BET}-1}{V_m\times C_{BET}}\frac{p}{p^0} \quad (10)$$

where p and p^0 are the pressure inside the sample cell and the saturation pressure of the adsorbate at a given temperature (bar), respectively, V is the volume adsorbed (dm^3), V_m is the volume of adsorbate required to form a complete monolayer (dm^3/g) and C_{BET} is the BET constant, associated with the magnitude of the adsorbent-adsorbate interactions.[159]

Based on the V_m value, the specific surface area, $A_{s,BET}$ (m^2/g), can be calculated by the following equation (Eq. 11):

$$A_{s,BET} = \frac{V_m\times N_A\times a_m}{V_{molar}\times m} \quad (11)$$

where N_A is the Avogadro constant (mol^{-1}), a_m is the cross-sectional area occupied by a single adsorbate molecule (16.2 $Å^2$ for N_2), V_{molar} is the molar volume of the adsorbate (dm^3/mol) and m is the sample mass (g).[157]

Apart from the specific surface area, the nitrogen adsorption measurements can also be used to determine the total pore volume, V_p (cm^3/g), of micro- and mesoporous adsorbents, assuming that for a relative pressure (p/p^0) in the 0.95-1 range, all pores are filled with condensed gas, and is described by the following expression (Eq.12):

$$V_p = n_{ads} \times V_{molar} \times B \quad (12)$$

where n_{ads} is the amount of N_2 adsorbed (mmol/g), V_{molar} is the molar volume of N_2 (cm^3/g) and B is a density conversion factor (for N_2 at -196 ºC is 0.0015458).[160]

The mean pore diameter can also be calculated assuming a cylindrical shaped pore by the following equation (Eq.13):

$$D_p = \frac{4 \times V_p}{A_{s,BET}} \quad (13)$$

where V_p is the total pore volume and $A_{s,BET}$ is the specific surface area determined by BET model.

In this work, N_2 adsorption/desorption isotherms were performed at -196 ºC using a Quantachrome Quadrasorb instrument. The samples were firstly outgassed under vacuum at 80 ºC for 6h and then at 120 ºC for 12h using a Quantachrome Masterprep instrument. All experiments were performed at Évora University.

2.5.6. Atomic Absorption Spectrometry (AAS)

AAS is one of the most widely used methods for the quantification of chemical elements, especially for trace metals analysis. This technique is based on irradiating free gaseous atoms with electromagnetic radiation in the ultraviolet/visible region at a specific wavelength, which will only be absorbed by the analyte in study, thus producing a measurable signal.[161] The amount of absorbed light is the difference between the initial light intensity (I_0) and the intensity of the transmitted light (I) considering that no interferences occur. The quantification of the analyte concentration is obtained by the Lambert-Beer law, that describes a linear relationship between the absorbance and the concentration of analyte atoms and the optical path which can be expressed by the following equation (Eq.14):

$$A = log\left(\frac{I_0}{I}\right) = \varepsilon \times L \times c \quad (14)$$

where ε is the molar extinction coefficient (m^2/mol), L is the optical path length (m) and c is the analyte concentration (mol/dm^3).[162]

Typically, an atomic absorption spectrometer can be divided into four main components (Figure 2.10): a light source, which emits an intense atomic line spectrum of the element of interest; an atomization system, where the sample is converted into gaseous atoms; a monochromator, which selects and isolates only the wavelength of light that is absorbed by the analyte; and a detector, which quantifies the intensity of light passing through the monochromator.[162-163]

The most common light sources in AAS are the hollow cathode lamps, which consist of an enclosed glass tube, filled with inert gas (Ar or Ne) at low pressure, containing an anode and a cathode coated with the element of interest. When an electrical potential is applied across the electrodes, the filling gas atoms are ionized and accelerated towards the cathode. Once the gas ions impact on the cathode surface, the metal atoms are ejected and collide with other gas ions, leading to their excitation and consequently to the emission of photons at a characteristic wavelength when returning to their ground state. Therefore, each hollow cathode lamp is specific for a given element, which restricts the AAS measurements to one element analysis at a time.[162, 164]

In general, the analysis of liquid samples performed by spectrometers with flame atomizers. In a typical experiment, the solution is aspirated by a pneumatic nebulizer, transformed into an aerosol in a nebulization chamber and mixed with the flame gases (usually a mixture of air-acetylene) before entering in the flame. Once the sample aerosol reaches the flame, a sequence of several processes can occur, including desolvation of the droplets, vaporization of solid particles, dissociation of molecular species into free atoms and possible undesired ionization of the atoms.[162-163]

The AAS analysis were performed in a Perkin Elmer AAnalyst 200 instrument (λ = 324.75 nm) using calibration solutions with Cu(II) concentrations ranging from 0.1 to 10 mg/L (Figure A.1. in the Appendix section). All experiments were performed at Faculty of Sciences of the University of Porto.

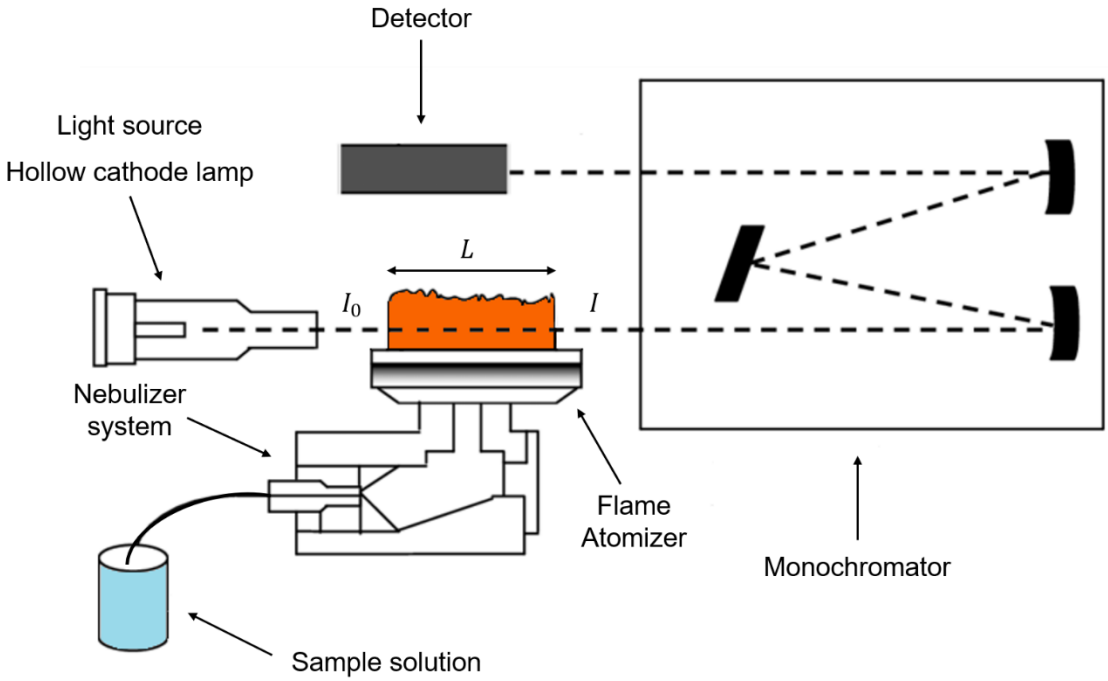

Figure 2.10. Schematic representation of the main components of an AAS instrument. Adapted from[165].

3. MOFs characterization

3.1. MIL-100(Fe)

3.1.1. PXRD

The as-synthesized MIL-100(Fe) was first characterized by PXRD, in order to obtain information about its crystallographic structure. As shown in Figure 3.1, the experimental PXRD pattern of MIL-100(Fe) is in good agreement with the simulated XRD pattern obtained from the crystallographic data of MIL-100(Fe) single crystals, confirming that the material was successfully prepared.[134]

Interestingly, despite the fact that the MOF synthesis was performed at room temperature, the experimental PXRD pattern exhibited well-defined and sharp diffraction peaks, which is a good indicator of the high crystallinity of the material. The main diffraction peaks observed at 2θ of 3.65º, 4.24º, 4.06º, 5.50º, 6.51º, 10.49º and 11.25º correspond to the (220), (311), (400), (331), (511), (822) and (842) lattice planes, respectively, which are characteristic of the cubic zeolite Mobil Thirty-Nine (MTN) architecture of MIL-100 materials indexed to the $Fd\bar{3}m$ space group.[166-167]

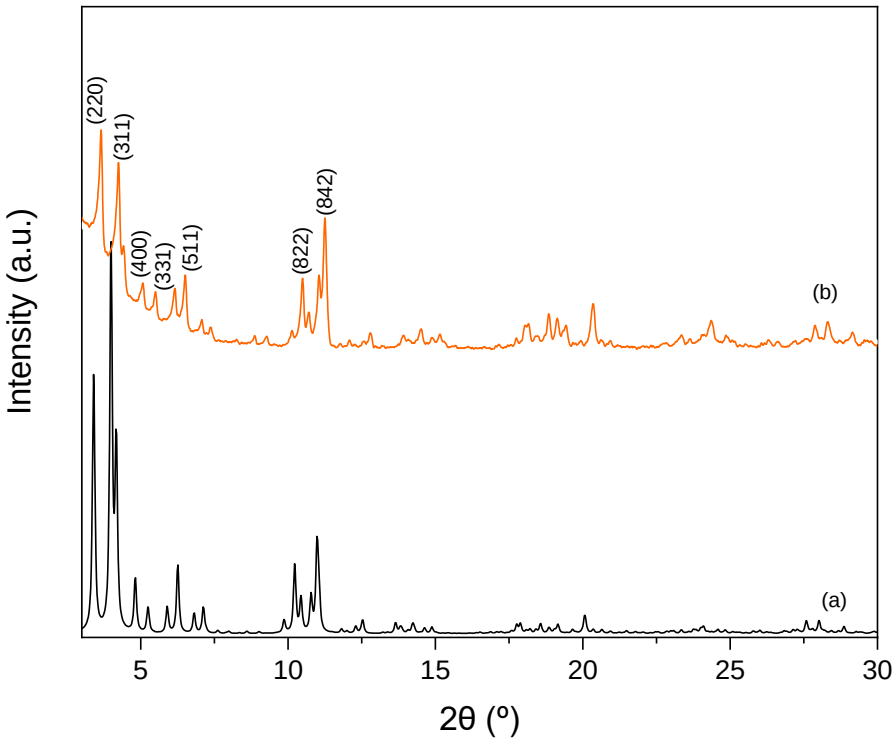

Figure 3.1. PXRD patterns of MIL-100(Fe) (a) simulated and (b) as-synthesized.

3.1.2. FT-IR

The molecular structure of MIL-100(Fe) was assessed by FT-IR and the resulting spectrum is displayed in Figure 3.2, revealing valuable information about the presence of characteristic vibrational bands related to the main functional groups in the framework structure.

The three main absorption peaks around 1630 cm^{-1}, 1574 cm^{-1} and 1383 cm^{-1} are attributed to the stretching vibrational mode of the C=O bond and the asymmetric and symmetric stretching vibration of the O–C–O bond of the coordinating carboxylate groups, respectively, confirming the presence of the organic linker in the framework of MIL-100(Fe).[168] Also, two sharp peaks at 760 cm^{-1} and 712 cm^{-1} can be observed corresponding to the bending vibrational modes of the =C–H bonds from the benzene rings. The vibrational band around 484 cm^{-1} is related to the stretching vibrational mode of Fe–O bond, indicating that the metal ions are coordinated to the carboxyl groups of the trimesate linkers.

Furthermore, the FT-IR spectrum shows that the purification method used to remove residual molecules of organic linker was efficient, due to the absence of the characteristic vibrational band at *ca*. 1710-1720 cm^{-1} associated with the stretching vibrational mode of the C=O bond of free carboxyl groups.[169]

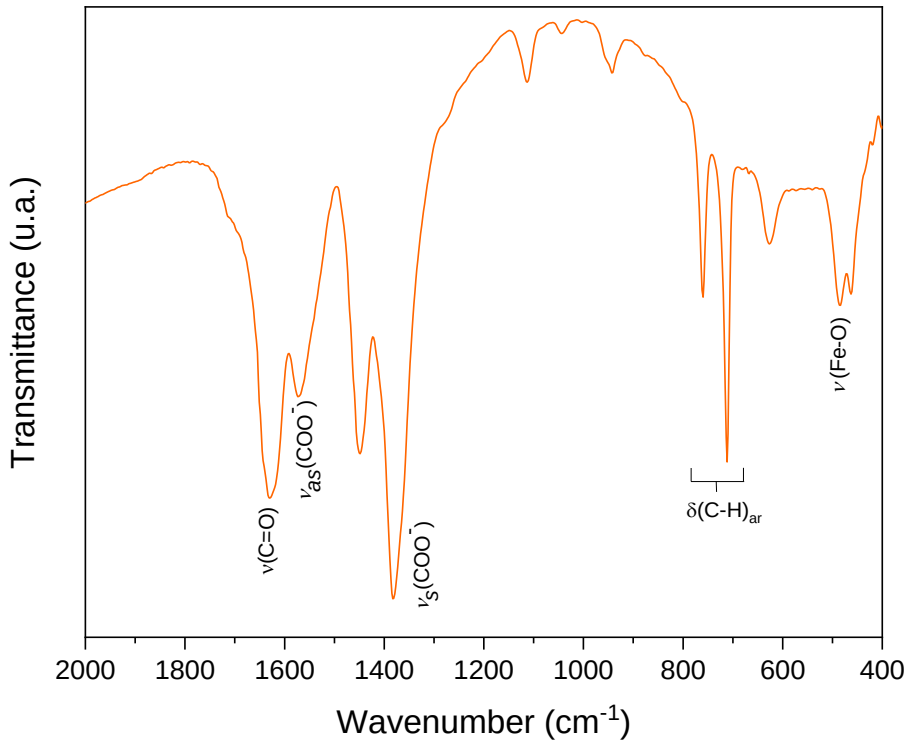

Figure 3.2. FT-IR spectrum of the as-synthesized MIL-100(Fe).

3.1.3. TGA

The thermal stability of MIL-100(Fe) was evaluated by TGA, revealing that the framework structure was stable up to 300 ºC, which is in agreement with previously published works.[170-171] The resulting TG curve, presented in Figure 3.3, showed the occurrence of several mass losses within the studied temperature range.

The first mass loss (~24%) around 50 ºC could be due to the release of physiosorbed water molecules on the MOF surface or inside the porous framework. The second mass loss (~9%) between 70 ºC and 250 ºC could be related to the removal of water molecules coordinated to the iron trimers and free trimesic acid molecules.

Moreover, the mass losses (~10% + 16%) between 300 and 500 ºC could be associated to the decomposition of coordinated trimesate groups, followed by the collapse of the MOF crystalline structure. According to the literature, pure trimesic acid compounds are thermally stable up to 250 ºC, which is 50 ºC below the temperature at which the MIL-100(Fe) structure begin to decompose.[172] This suggests that the organic precursors are in fact coordinated to the metal clusters, thus increasing their thermal stability. The final mass loss (~12%) may have been caused by the further destruction of the remaining framework and potential formation of iron oxides from the metal-oxo cluster units. [171, 173]

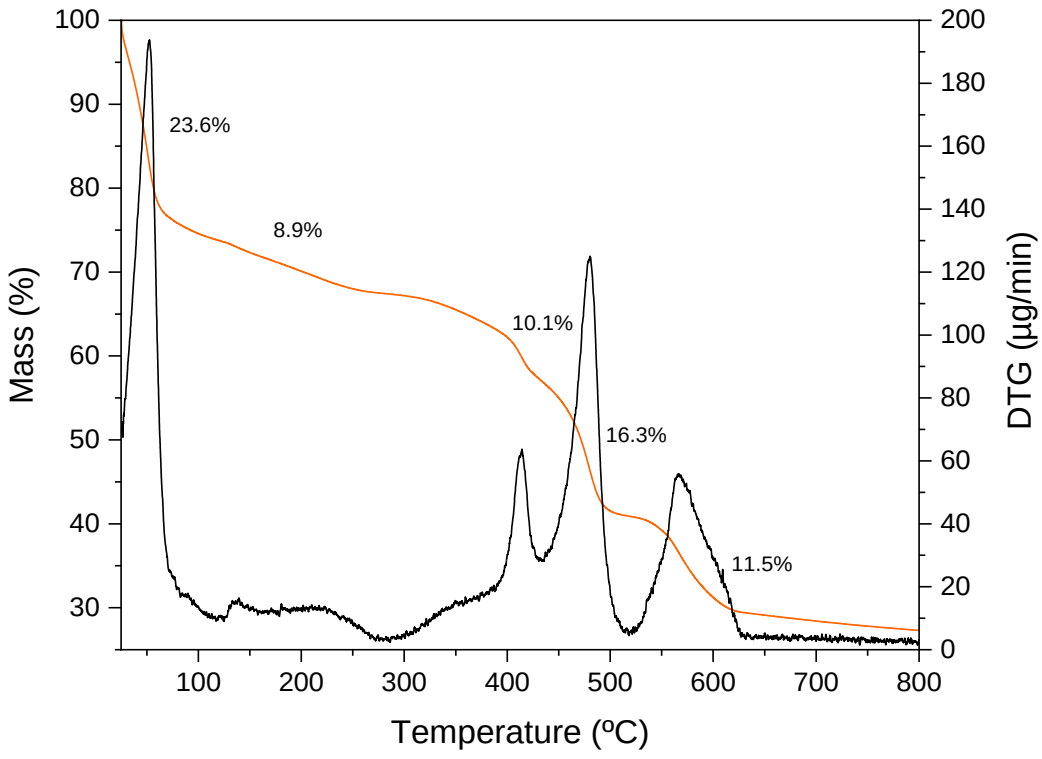

Figure 3.3. TG and DTG curves of MIL-100(Fe).

3.1.4. SEM/EDS

The morphology and particle size of MIL-100(Fe) were verified by SEM while its chemical composition was assessed by EDS analysis. The resulting SEM micrographs and the EDS spectrum are represented in Figure 3.4 and 3.5, respectively.

The SEM micrographs revealed agglomerated particles with octahedral shape and an average particle size of 274 ± 57 nm. The resulting morphology is in agreement with the underlying topology identified through XRD analysis. Moreover, these observations are characteristic of MIL-100(Fe) materials that were synthetized under similar conditions [168, 174]

The EDS analysis detected the main chemical elements present in MIL-100(Fe), such as iron, carbon, and oxygen, confirming the elemental composition of the sample. However, the relative abundance of oxygen and carbon cannot be unequivocally attributed to the sample composition due to external influences related to the sample preparation, such as from the double-sided carbon tape used to fix the sample and its exposure to an oxidizing atmosphere. The appearance of small amounts of gold and palladium is the result of the deposition of a conductive coating before SEM analyses.

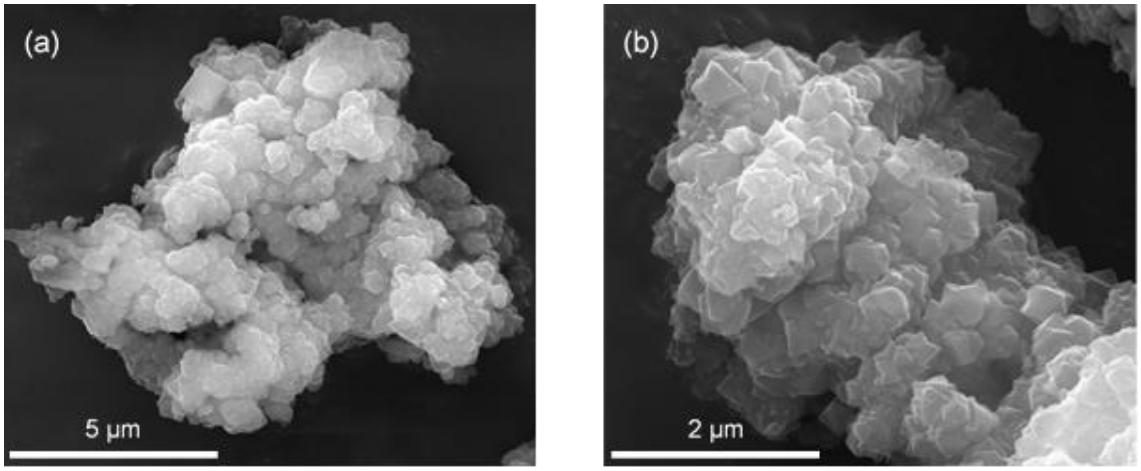

Figure 3.4. SEM micrographs of MIL-100(Fe) at different magnifications (a) 20,000 x (b) 50,000x.

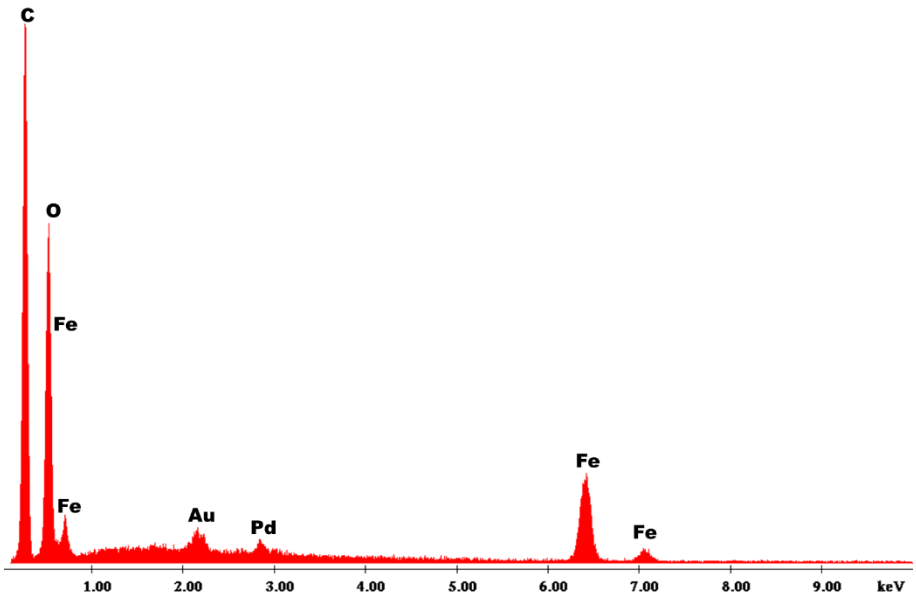

Figure 3.5. EDS spectrum of MIL-100(Fe).

3.2. MIL-88A(Fe)

3.2.1. PXRD

The crystalline structure of the as-synthesized MIL-88A(Fe) was analysed by PXRD. Figure 3.6 shows the experimental and simulated XRD pattern from crystallographic data of MIL-88A(Fe) single crystals with hexagonal structure indexed to the $P\bar{6}2c$ space group.[175]

As it can be observed, the experimental diffraction pattern is in accordance with the simulated pattern, indicating that the crystalline structure of MIL-88A(Fe) was successfully prepared. However, the intensity of the diffraction peak at 2θ = 8.10º, corresponding to the (100) crystallographic facet, is much lower than the intensity of the simulated one, which might be due to the type of solvent used in the material synthesis. It is known that the solvents used in MOF syntheses can have a strong influence on the overall morphologies of the crystals owing to their ability to act as directing agents during the self-assembly process. Previously reported studies, suggest that MIL-88A(Fe) crystals synthesized in water exhibit preferential growth of the (101) crystallographic facet over the (100), which is consistent with the obtained results.[176-177]

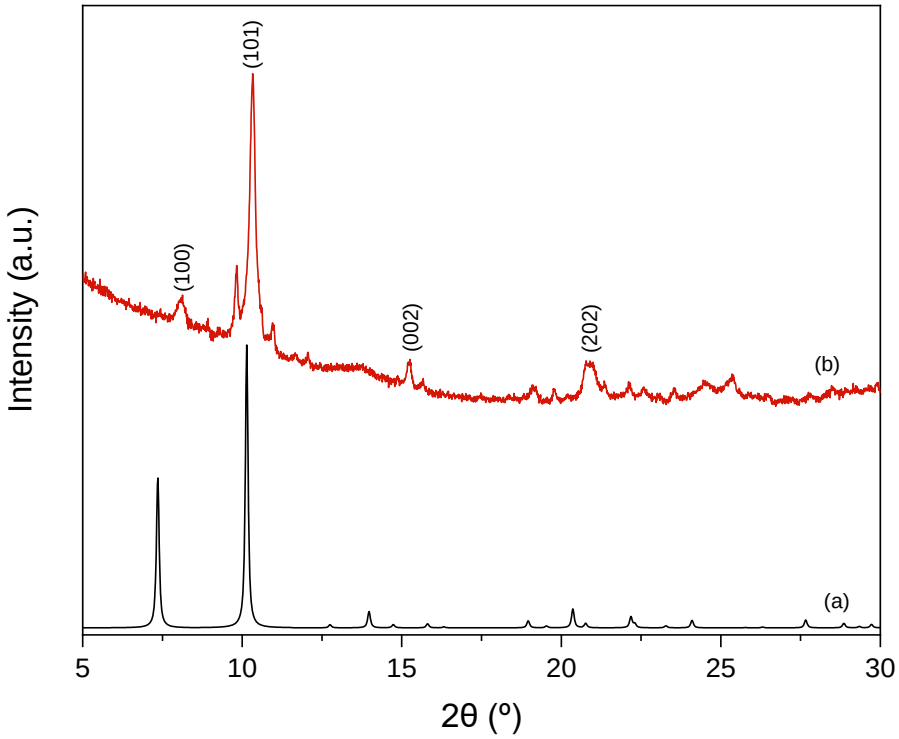

Figure 3.6. PXRD pattern of MIL-88A(Fe) (a) simulated and (b) as-synthesized.

3.2.2. FT-IR

The chemical structure of MIL-88A(Fe) was further characterized by FT-IR and the obtained spectrum is shown in Figure 3.7. The two strong vibrational bands at 1601 cm^{-1} and 1394 cm^{-1} correspond to the asymmetric and symmetric stretching vibrational modes of the O–C–O bond from the coordinating carboxylate groups of the fumaric acid molecules, respectively. This confirms the presence of the organic linker in the MIL-88A(Fe) framework. The sharp, but less intense, vibrational band at 980 cm^{-1} can be assigned to out-of-plane bending vibrational modes of the C=C bond. Furthermore, the absorption peak at *ca*. 575 cm^{-1} can be attributed to the stretching vibrational mode of the Fe–O bond. These findings confirm that the fumarate anions are coordinated to the iron cations through the carboxylate groups, resulting in iron-oxo clusters.

The absence of a strong vibrational band around 1700 cm^{-1}, typical of the stretching vibrational mode of free carbonyl groups, indicates that free fumaric acid molecules were successfully removed during the purification process. [178-179]

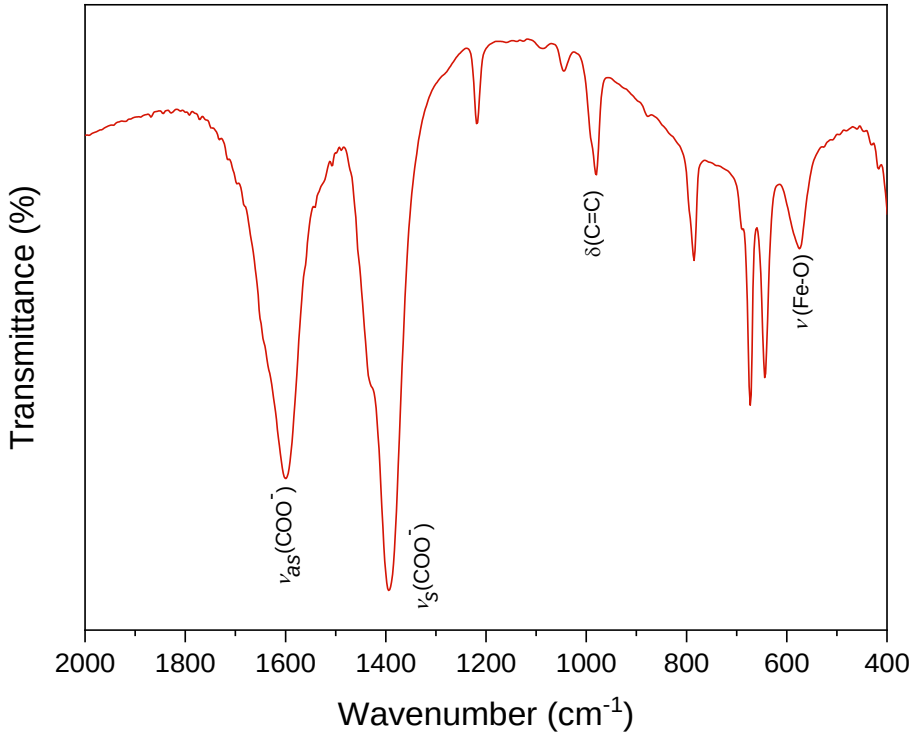

Figure 3.7. FT-IR spectrum of the as-synthesized MIL-88A(Fe).

3.2.3. TGA

The thermal behaviour of the as-synthesized MIL-88A(Fe) was examined by TGA and the obtained data is presented in Figure 3.8. The TG curve revealed four main mass loss stages upon heating the sample from room temperature up to 800 ºC.

The first mass loss (~26%), occurred from 50 to 100 ºC and can be related to the volatilization of physically adsorbed water molecules inside the framework cavities. The second mass loss (~11%), that occurs between 200 ºC and 300 ºC, could be due to the removal of water molecules bounded to the iron trimer clusters concomitant with a minor decomposition of free fumaric acid molecules.

Further degradation (~24%) occurred from 300 ºC to 450 ºC which can be attributed to the complete decomposition of the fumarate ligands, followed by the collapse of the metal-organic framework. According to the literature, pure fumaric acid compounds present lower thermal stability than what was observed for MIL-88A(Fe), since they are completely decomposed after 280 ºC. This suggests that the fumarate anions are strongly coordinated to the metal clusters, thus increasing their thermal stability.[180]

The final mass loss (~13%) took place at 600 ºC and can be assigned to the progressive formation of iron oxides from the metal-oxo clusters. The results gathered through TGA indicate that the framework structure of MIL-88A(Fe) is thermally stable up to 300 ºC, which is in good agreement with previously reported studies.[176, 179]

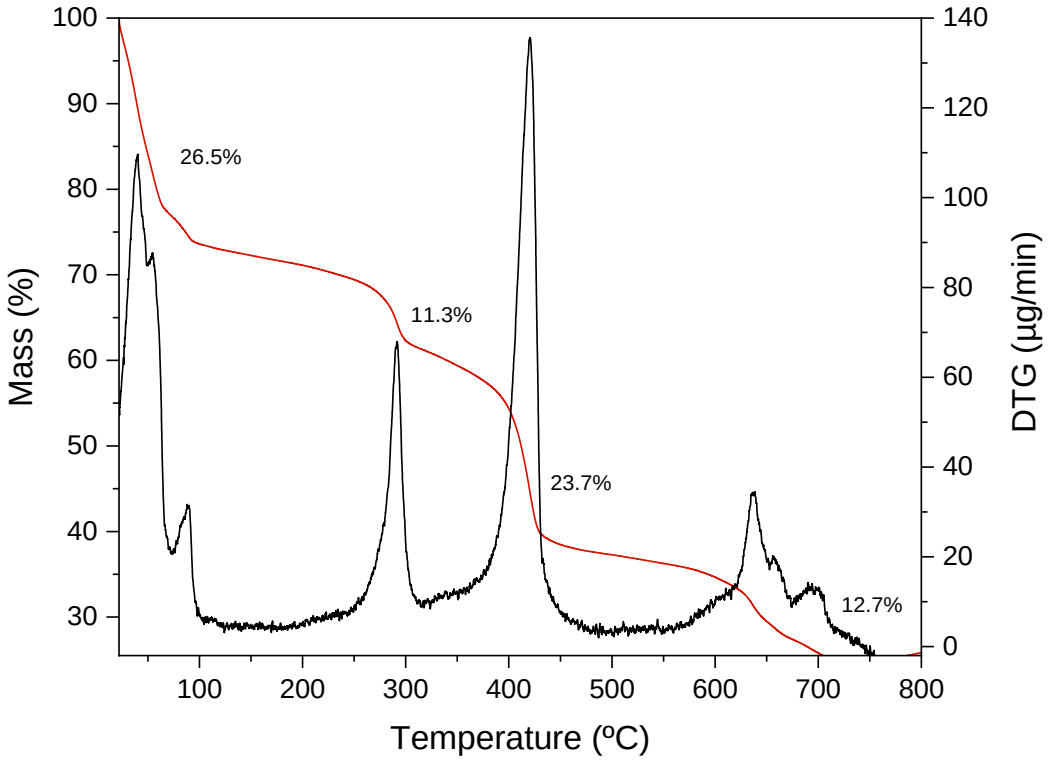

Figure 3.8. TG and DTG curves of MIL-88A(Fe).

3.2.4. SEM/EDS

The morphology of the prepared MIL-88A(Fe) particles was evaluated by SEM and the resulting micrographs at different magnifications are shown in Figure 3.9. The SEM micrographs revealed well-crystallized particles with a uniform hexagonal rod-like shape at the micrometric scale. The average size of the MIL-88A(Fe) microrods was 5.83 ± 1.00 µm in length and 1.33 ± 1.00 µm in width. The observed morphology is characteristic of MIL-88A(Fe) particles synthetized under similar conditions and it is consistent with the results obtained through PXRD analysis.[138]

The chemical composition of MIL-88A(Fe) was evaluated by EDS analysis and it is presented in Figure 3.10. As expected, the obtained EDS spectrum confirmed the presence of iron in the sample. Considerable amounts of chlorine were also detected, probably arising from the ferric chloride used as metal precursor in the MOF synthesis.

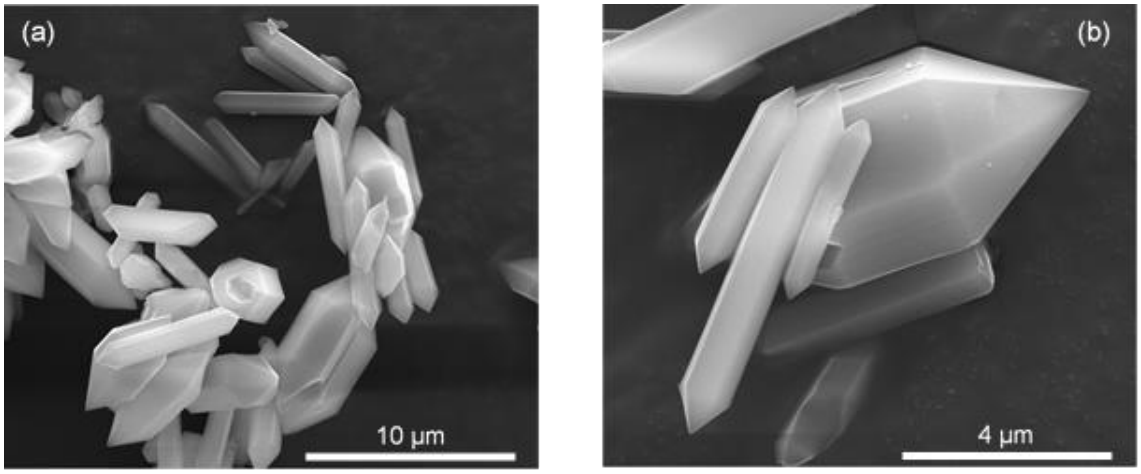

Figure 3.9. SEM micrographs of MIL-88A(Fe) at different magnifications (a) 5,000 x, (b) 25,000 x.

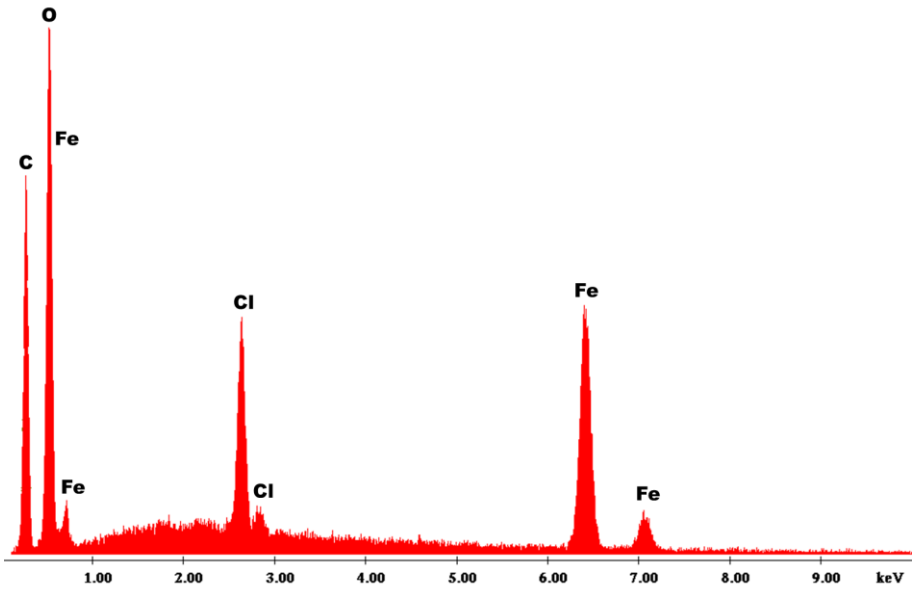

Figure 3.10. EDS spectrum of MIL-88A(Fe).

3.3. MIL-88B(Fe)

3.3.1. PXRD

The crystallographic structure of the prepared MIL-88B(Fe) crystalline framework was evaluated by PXRD. As it can be seen in Figure 3.11, the experimental diffraction pattern matched well with the simulated pattern obtained from the crystallographic data of single crystals, confirming the successful synthesis of MIL-88B(Fe).[133] The diffraction peaks at 2θ of 9.60º, 10.61º, 16.84º, 19.29º, 19.82º, 21.36º and 26.01º corresponding to the (100), (101), (103), (004), (201), (202) and (105) lattice planes are characteristic of the hexagonal MIL-88B(Fe) topology indexed to the $P\bar{6}2c$ space group.[181] Moreover, the

appearance of narrow and well-defined diffraction peaks indicates that the solvothermal synthesis produced highly crystalline structures.[182]

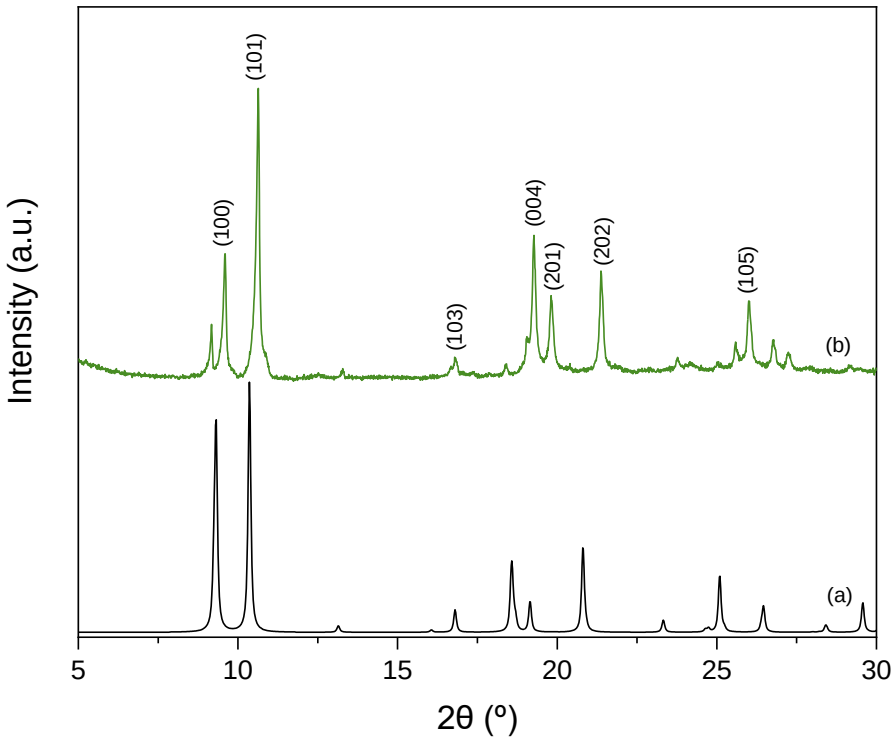

Figure 3.11. PXRD pattern of MIL-88B(Fe) (a) simulated and (b) as-synthesized.

3.3.2. FT-IR

In order to further analyse the structural integrity of MIL-88B(Fe), FT-IR spectroscopy was performed, and the acquired spectrum is presented in Figure 3.12. The absorption peak at 1652 cm^{-1} is attributed to the stretching vibrational mode of the carbonyl group from the coordinated terephthalate linker. The strong absorption peaks at 1602 cm^{-1} and 1392 cm^{-1} are characteristic of the asymmetric and symmetric stretching vibrational modes of the carboxylate groups, respectively, confirming the existence of coordinated dicarboxylate linkers in the structure of MIL-88B(Fe). In addition, the vibrational bands at 749 cm^{-1} and 555 cm^{-1} are attributed to the bending vibrational mode of the =C–H bonds in the aromatic ring and the stretching vibrational mode of the Fe–O bond of the iron-oxo-clusters, respectively.[183-184]

The IR spectrum also suggests that the purification process performed with deionized water and ethanol was efficient, due to the absence of characteristic absorption peaks from the solvent (DMF) and non-coordinated ligands in the 1750-1700 cm^{-1} range assigned to stretching vibrations of the C=O group.[185]

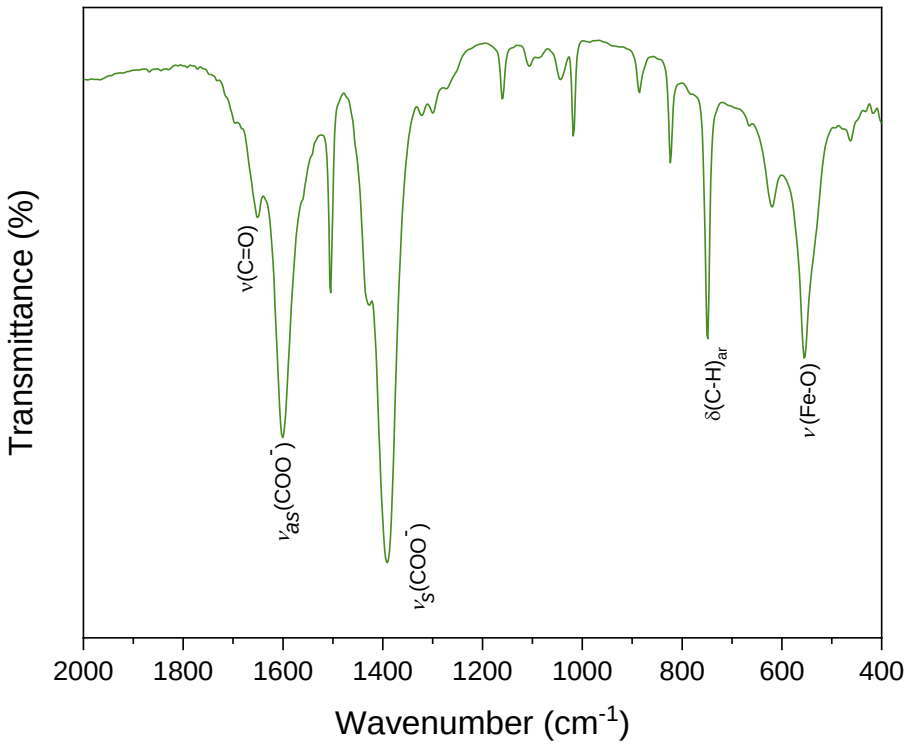

Figure 3.12. FT-IR spectrum of the as-synthesized MIL-88B(Fe).

3.3.3. TGA

TGA provided information about the thermal decomposition of MIL-88B(Fe) and the resulting TG and DTG curves are shown in Figure 3.13. The TG curve revealed two mass loss stages as the temperature increased up to 800 ºC. No mass loss was observed until 300 ºC, indicating that the structure of MIL-88B(Fe) is thermally stable at this temperature range, which is in good agreement with previously reported TG curves.[186-187]

A drastic mass loss of 29.5% occurred from 300 ºC up to 500 ºC, which could be ascribed to the decomposition of the terephthalate anions along with the rupture of the MIL-88B(Fe) framework. The second step begun above 500 ºC and can be attributed to the further pyrolysis of the organic content and transformation of the metal clusters into iron oxides.[186-187]

The TG curve also confirmed that the purification and drying processes to remove solvent or water molecules inside the pores and/or adsorbed at the MOF surface were successful given the absence of mass losses below 300 ºC, which otherwise would occur between 30 ºC and 180 ºC, typical of the volatilization of solvent molecules, such as water, ethanol and DMF.[187]

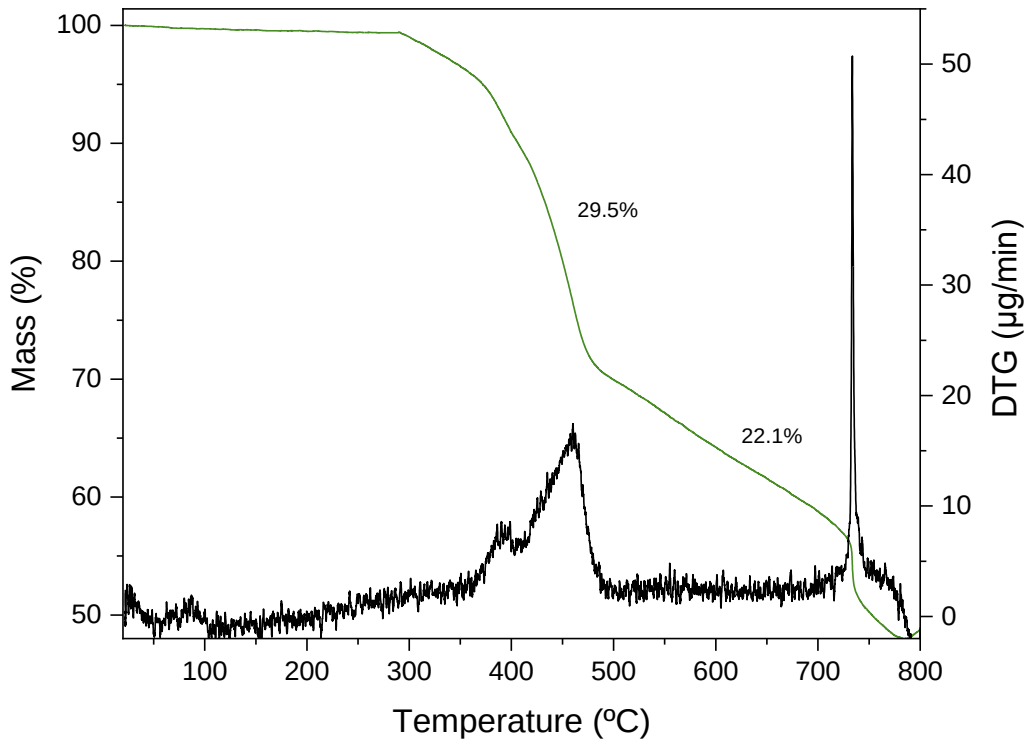

Figure 3.13. TG and DTG curves of MIL-88B(Fe).

3.3.4. SEM/EDS

The morphological characterization of MIL-88B(Fe) particles was performed by SEM and the obtained micrographs are shown in Figure 3.14. The SEM micrographs revealed elongated particles with a hexagonal shape, which is consistent with the obtained PXRD pattern and previously reported studies.[183, 186, 188] The MIL-88B(Fe) particles display an average length of 6.22 ± 2.00 µm and average width of 1.47 ± 0.50 µm.

The elemental composition of MIL-88B(Fe) was attained by EDS analysis and the obtained EDS spectrum is shown in Figure 3.15. The presence of iron in the sample was confirmed. It was also found minor relative quantities of chlorine, which was probably resultant from the ferric chloride used as metal precursor in the synthesis of MIL-88B(Fe).

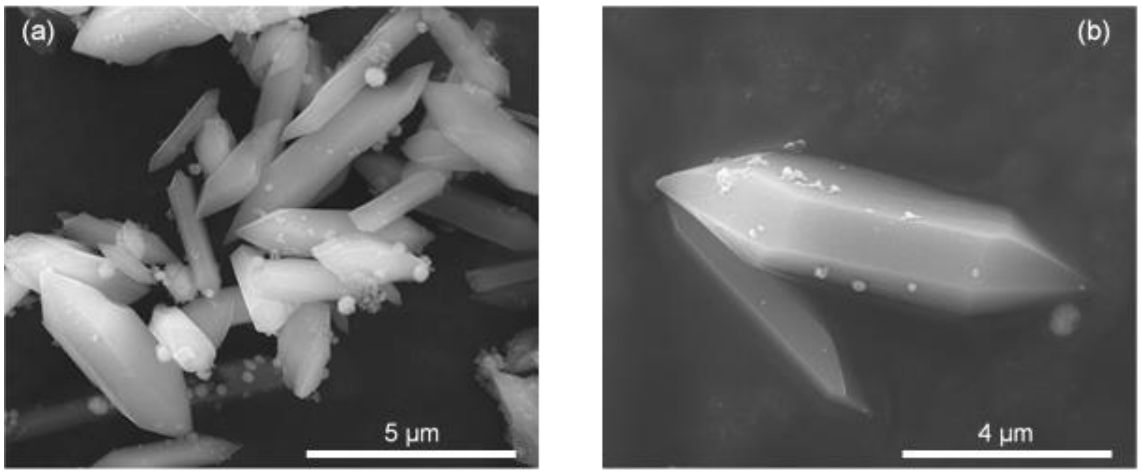

Figure 3.14. SEM micrographs of MIL-88B(Fe) at different magnifications (a) 15,000 x, (b) 25,000 x.

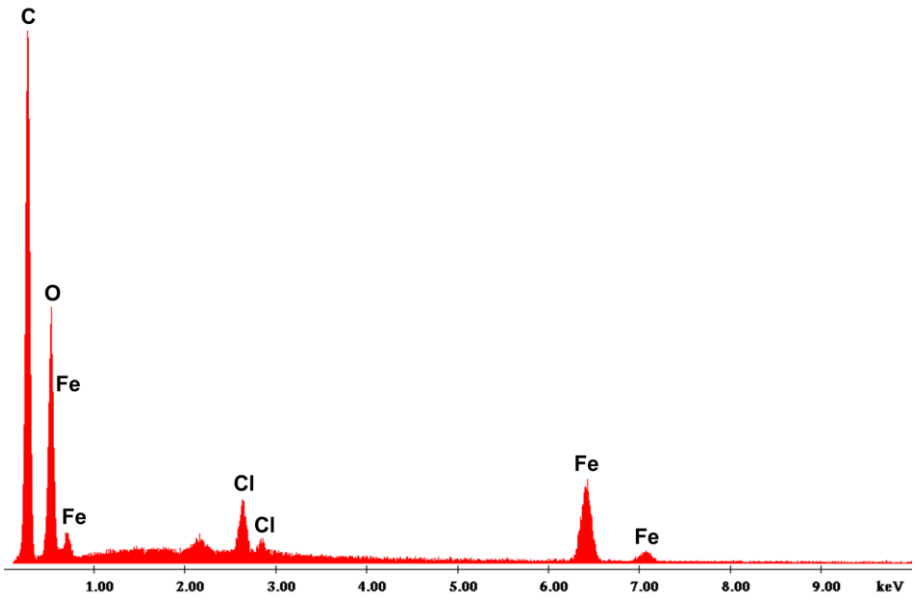

Figure 3.15. EDS spectrum of MIL-88B(Fe).

3.4. MIL-53(Fe)

3.4.1. PXRD

Figure 3.16 presents the PXRD patterns of MIL-53(Fe), before and after activation procedure, and the simulated pattern from crystallographic data of MIL-53(Fe) single crystal structure. The framework of MIL-53(Fe) is well-known for its breathing behaviour, consisting of reversible structural deformations that can be triggered by temperature, pressure, or exchange of guest molecules. In this case, the as-synthetized MIL-53(Fe) underwent structural transitions due to the uptake of different guest molecules.[101, 189] The structural analysis of MIL-53(Fe) before activation resulted in a diffraction pattern that is

assigned to the crystallographic structure of MIL-53(Fe) when the pores are filled with DMF molecules. DMF tends to establish strong hydrogen bonding interactions with the carboxylate groups inside the framework pores, inducing a gradual closure of MIL-53(Fe) pores, and consequently altering the unit cell parameters and distance between the lattice planes. This results in substantial changes in the position of the diffraction peaks associated with the characteristic crystallographic planes of MIL-53(Fe). The XRD pattern of MIL-53(Fe) before activation is in accordance with previously reported studies in the literature for MIL-53(Fe) materials containing DMF molecules.[190-191]

The activation of MIL-53(Fe) consisted in a guest exchange process, where DMF molecules were replaced by water molecules. Since water molecules have a lower boiling point than DMF molecules, they are easier to remove by standard drying procedures. The PXRD pattern obtained for the MOF after the activation process is in agreement with the simulated pattern from MIL-53(Fe) single crystals indexed to the $C2/c$ space group, being a good indicator that the synthesis and activation of MIL-53(Fe) were successful.[131, 191] These outcomes further evidence the flexible behaviour of the framework of MIL-53(Fe) without permanent structural deformation upon guest molecules exchange.

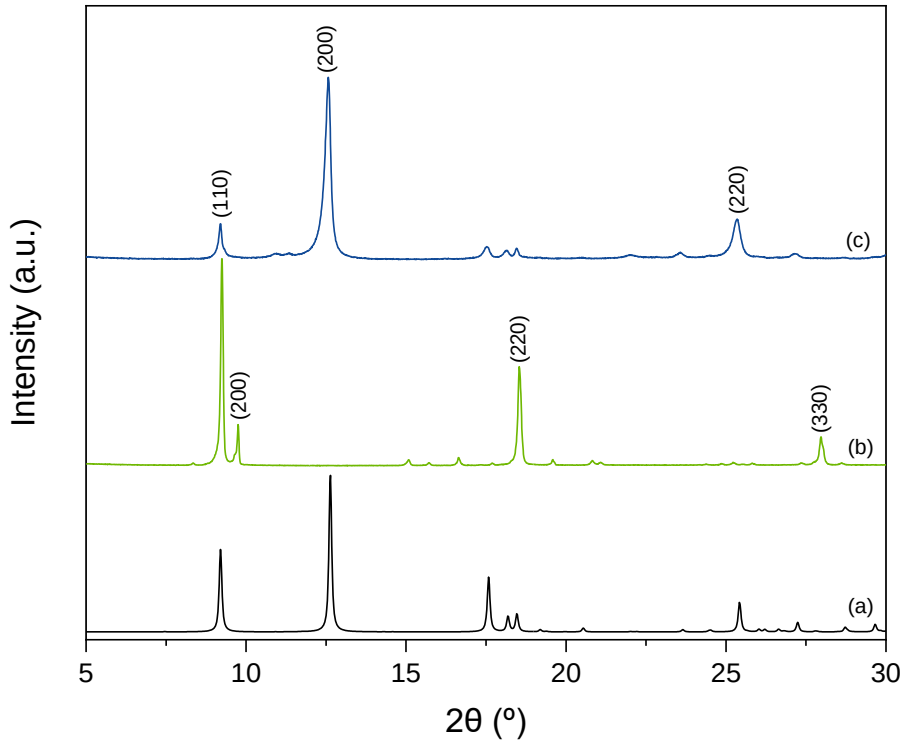

Figure 3.16. PXRD pattern of MIL-53(Fe) (a) simulated, (b) before activation, and (c) after activation.

3.4.2. FT-IR

The functional groups within the structure of MIL-53(Fe) before and after activation were characterized by FT-IR spectroscopy, and the corresponding spectra are shown in Figure 3.17. By comparison of both spectra, it can be seen the appearance of a more intense absorption peak at 1668 cm^{-1} in the infrared spectrum of MIL-53(Fe) before activation that after the activation, which can be assigned to the stretching vibrational mode of the carbonyl group of adsorbed DMF molecules.[190] A shift to higher wavenumbers can also be observed for the characteristic vibrational bands of the O–C–O asymmetrical and symmetrical stretching modes of the carboxylic groups from 1536 cm^{-1} to 1556 cm^{-1} and from 1384 cm^{-1} to 1392 cm^{-1}, respectively, in the presence of DMF. This can be attributed to the influence of the hydrogen bonds established between the hydroxyl groups belonging to the carboxylic groups and the aldehyde moiety of DMF.[190]

Furthermore, the sharp vibrational band at 750 cm^{-1} can be assigned to the bending vibrational mode of the =C–H bonds of the benzene ring. The absorption peak at 538 cm^{-1} can be ascribed to the stretching mode of Fe–O bond, confirming the coordination of the terephthalate linkers to the metal ions.[141, 192]

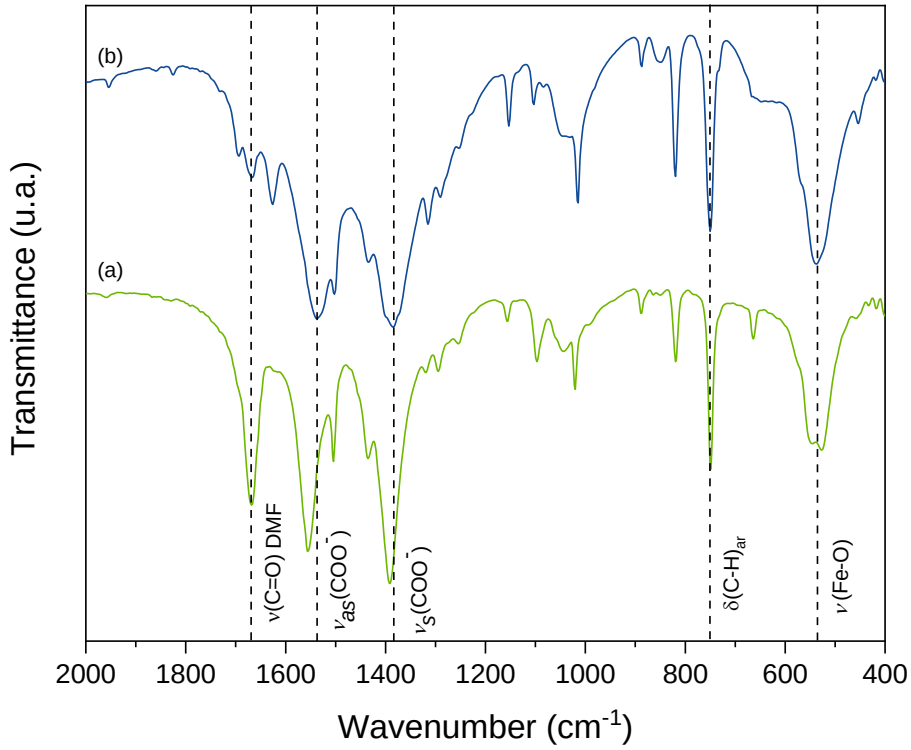

Figure 3.17. FT-IR spectrum of MIL-53(Fe) (a) before activation and (b) after activation.

3.4.3. TGA

The thermal profiles of the pristine MIL-53(Fe) before and after activation obtained by TGA are shown in Figure 3.18 and 3.19, providing valuable information about the thermal stability of the framework and presence of different guest molecules. Both TG curves revealed very similar steps at specific temperature points, suggesting that the frameworks had nearly the same thermal stability, but distinct content of guest molecules.

The TG profile of MIL-53(Fe) before activation showed a notorious mass loss (~18%) before 250 ºC, which could be due to the desorption of guest molecules that were present in MIL-53(Fe) pores. The DTG curve revealed that the maximum mass loss occurred at 176 ºC, which is in the same temperature range as the boiling point of DMF. Whereas, in the TG curve of MIL-53(Fe) after activation, a minimal mass loss (~5%) was observed below 100 ºC, which could be related to the removal of physiosorbed water molecules.[131, 190] Between 250 ºC and 500 ºC, both materials lost approximately 36% of their mass, which could correspond to the decomposition of the terephthalate linkers and partial collapse of the MOF framework. Above 500 ºC, a mass loss of ~12% occurred in both TG curves, which could be associated to the complete collapse of the MOF framework and further pyrolysis of the organic backbone combined with the formation of iron oxides from the metal-oxo clusters.[193-194]

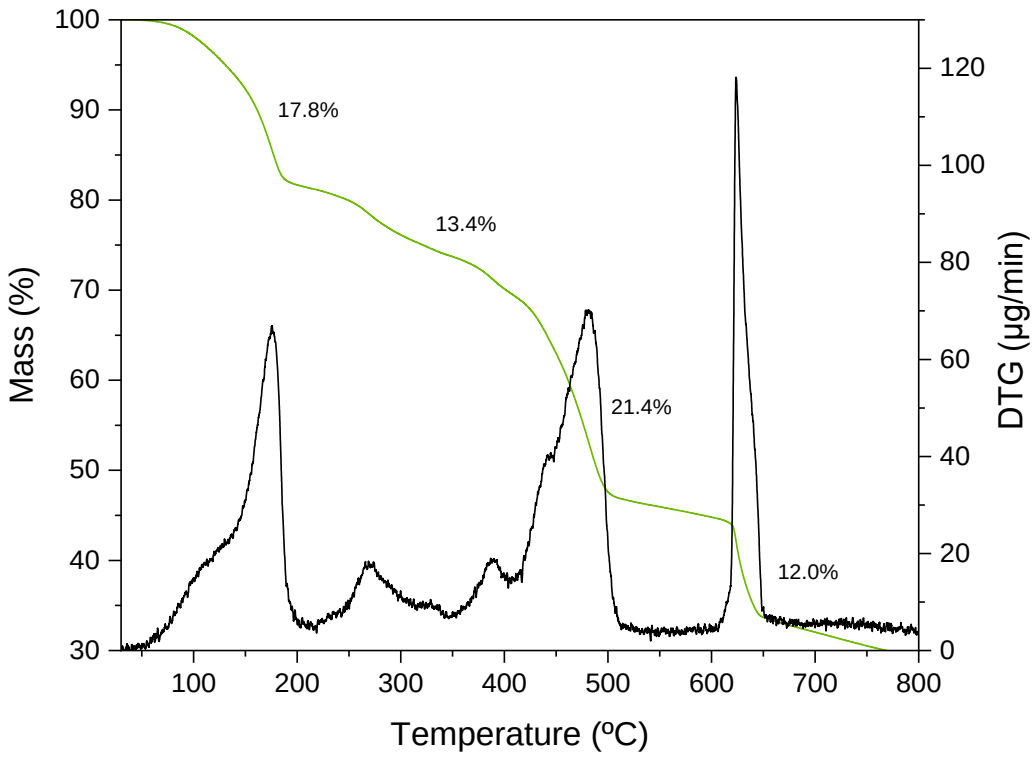

Figure 3.18. TG and DTG curves of MIL-53(Fe) before activation.

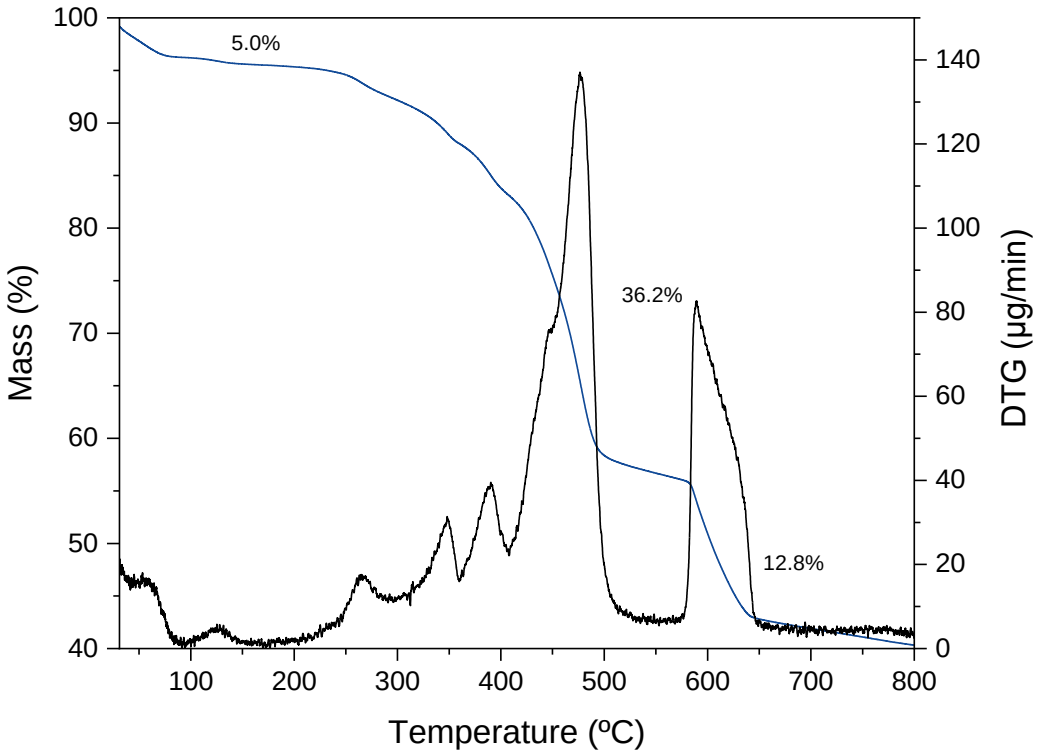

Figure 3.19. TG and DTG curves of MIL-53(Fe) after activation.

3.4.4. SEM/EDS

The morphology and particle size of MIL-53(Fe) before and after activation were evaluated by SEM and the corresponding micrographs are presented in Figure 3.20. The SEM micrographs showed analogous morphologies for both MIL-53(Fe) before and after activation, revealing well-defined elongated particles with triangular prism shape at a micrometric scale, which is characteristic of MIL-53(Fe) polycrystals synthetized under the same solvothermal conditions, according to previously reported studies.[140, 194] The average size of MIL-53(Fe) particles before activation was 30.1 ± 9.0 µm in length and 13.7 ± 6.0 µm in width, while MIL-53(Fe) particles after activation revealed an average size of 43.8 ± 18.0 µm in length and 17.6 ± 6.0 µm in width, suggesting that the particle sizes were not significantly affected by the guest exchange process.

The elemental compositions of MIL-53(Fe) before and after activation were also analysed by EDS and the respective spectra are shown in figure 3.21. Both samples revealed very similar elemental compositions, in which the presence of iron can be unequivocally attributed to the MOF inorganic building units. The EDS spectrum of MIL-53(Fe) before activation does not reveal elemental traces of nitrogen, from DMF, probably due to its relatively low content in comparison with the overall composition of the material, making nitrogen below the EDS detection limit (0.1 wt%).

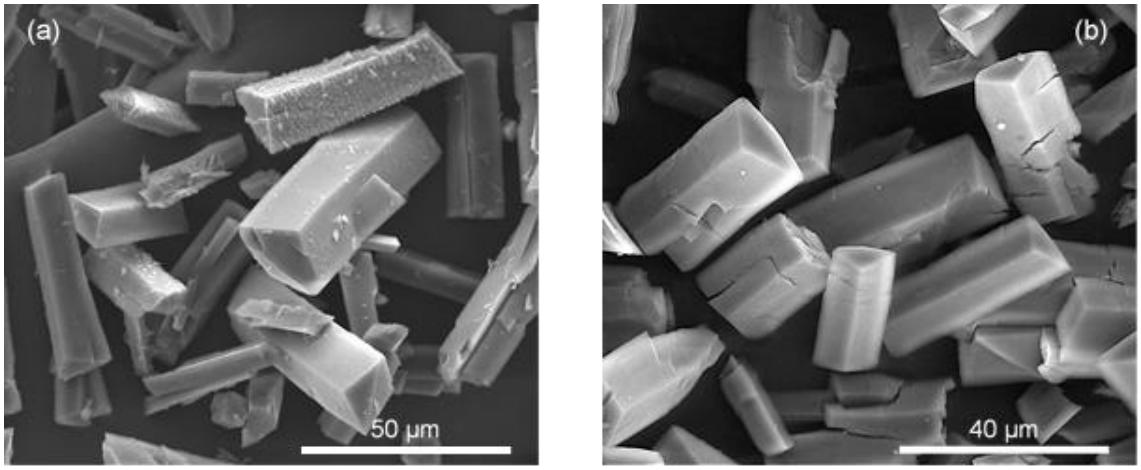

Figure 3.20. SEM micrographs of MIL-53(Fe) (a) before activation (2,000x) and (b) after activation (2,500x).

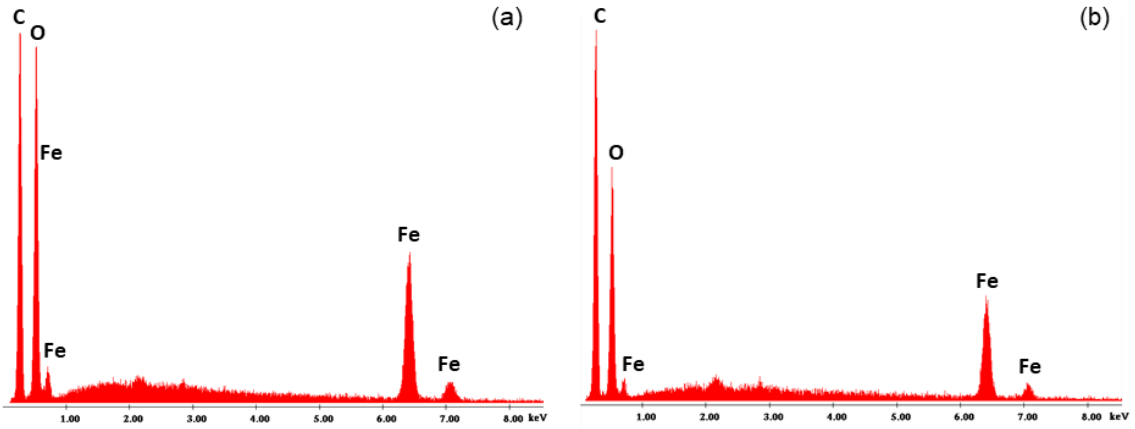

Figure 3.21. EDS spectra of MIL-53(Fe) (a) before activation, and (b) after activation.

3.5. ZIF-67(Co)

3.5.1. PXRD

The crystallographic structure of the as-synthetized ZIF-67(Co) was characterized by PXRD. As shown in Figure 3.22, the obtained PXRD pattern was compared with the simulated pattern from the single crystal structure of ZIF-67(Co). The intensity and position of all experimental diffraction peaks are in good agreement with the predicted pattern indexed to a sodalite topology with a cubic lattice in a space group $I\bar{4}3m$, which is characteristic of ZIF-67(Co) crystals. These outcomes suggest that the synthesis of ZIF-67(Co) was successful and resulted in pure-phase and highly crystalline products.[135]

195-196

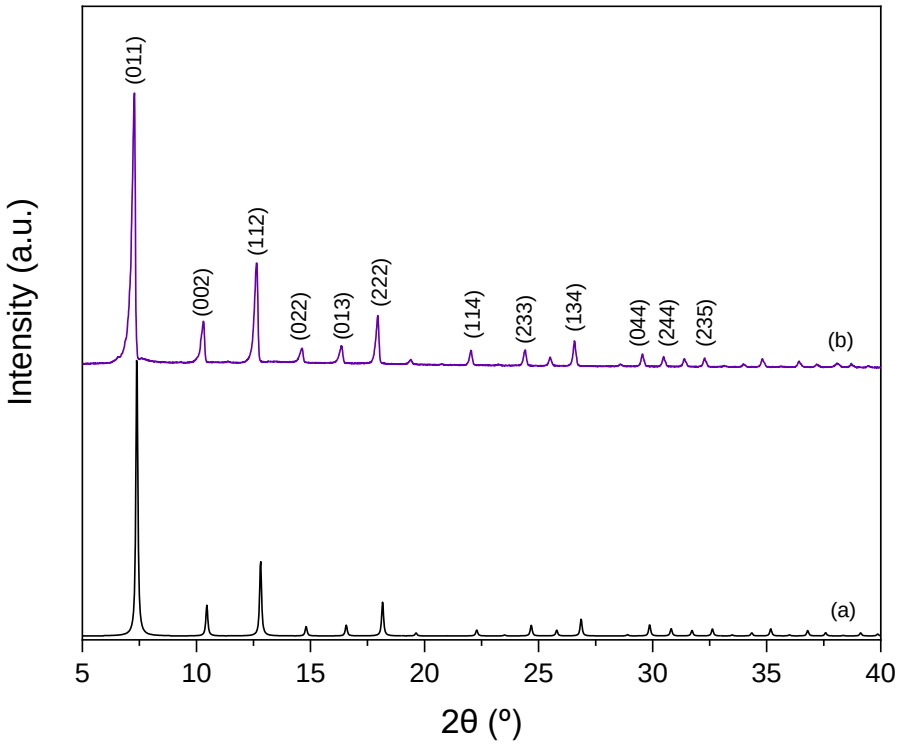

Figure 3.22. PXRD pattern of ZIF-67(Co) (a) simulated and (b) as-synthesized.

3.5.2. FT-IR

The molecular structure of ZIF-67(Co) was confirmed by FT-IR spectroscopy. The infrared spectrum is displayed in Figure 3.23 and it is consistent with previously reported spectra of ZIF-67(Co). [195, 197-198]

The absorption peak at 1579 cm^{-1} is assigned to the stretching vibrational mode of C=N bonding in the imidazole ring of the 2-methylimidazolate linker. The intense absorption peaks in the 1380–1500 cm^{-1} range are associated to the entire imidazole ring stretching vibrational mode. The set of intense vibrational bands in the spectral region between 1300 cm^{-1} and 990 cm^{-1} are attributed to the in-plane bending of the imidazole ring, while those at *ca*. 756 cm^{-1} and 694 cm^{-1} are from the out-of-plane bending of the ring. These observations confirm the presence of the 2-methylimidazolate linker in the framework of ZIF-67(Co). Additionally, the absorption peak at 424 cm^{-1} can be ascribed to the Co–N bond, proving that the metal cations are coordinated to the nitrogen from the organic linkers.[195, 197-198]

The absence of characteristic vibrational bands around 1850-1800 cm^{-1} assigned to the resonance between the N–H···N out-of-plane bending vibration and the N–H stretching vibration, suggest that all of the 2-methylimidazolate linkers are completely deprotonated, this is, they are coordinated to the cobalt ions, indicating that the

purification process used to remove free organic linkers inside the pores was efficient.[195, 199]

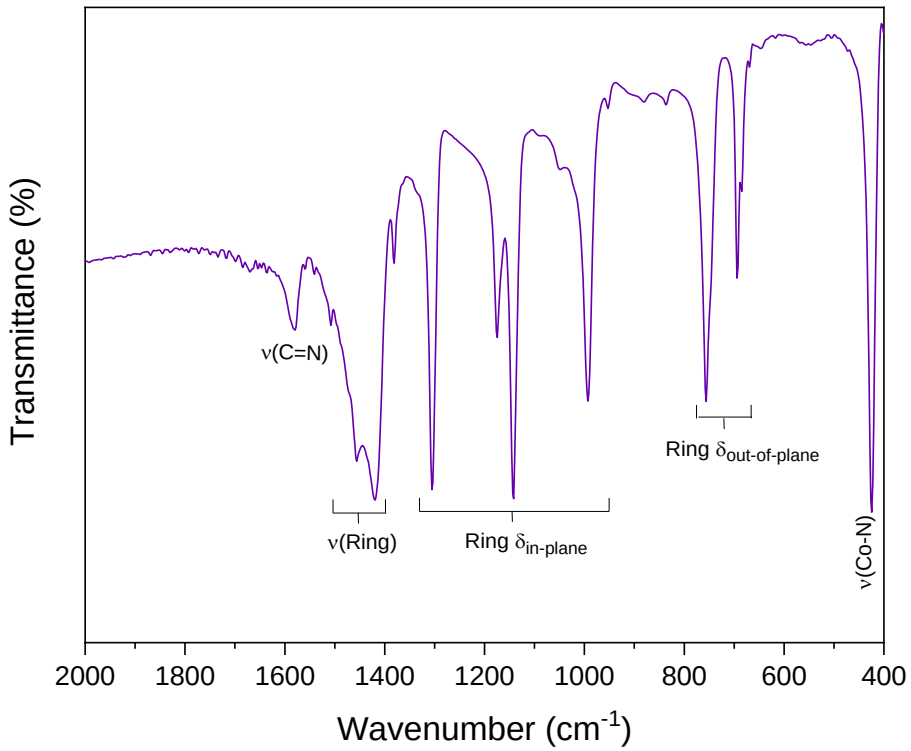

Figure 3.23. FT-IR spectrum of the as-synthesized ZIF-67(Co).

3.5.3. TGA

The thermal behaviour of the as-synthetized ZIF-67(Co) was examined by TGA and the obtained TG and DTG curves are shown in Figure 3.24. The TG curve revealed two mass loss stages with the increase of temperature in the 25 ºC to 800 ºC range. There were almost no mass changes below 500 ºC, indicating that the structure of ZIF-67(Co) is very stable in this temperature range, which is consistent with previous reports in the literature.[200-201] Additionally, this observation suggests that the purification and drying procedures used to remove guest molecules located inside the pores of the framework were successful.[202] Above 500 ºC, it can be seen that ZIF-67(Co) structure underwent through an abrupt mass loss (~40%), which could be due to the decomposition of 2-methylimidazolate linkers and subsequent collapse of the framework of ZIF-67(Co). Previously reported studies, suggest that pure 2-methylimidazole compounds are only stable up to 270 ºC, which is much lower than the decomposition temperature observed, further confirming that the 2-methylimidazolate anionic linkers are coordinated to the cobalt cations, thus leading to an increase in their overall stability.[203]

As the temperature continues to rise up to 800 ºC, a less noticeable mass loss occurred (~30%), which could be attributed to the further degradation of the remaining organic structure and the aggregation of cobalt to form metallic and/or metal-oxide nanoparticles.[204]

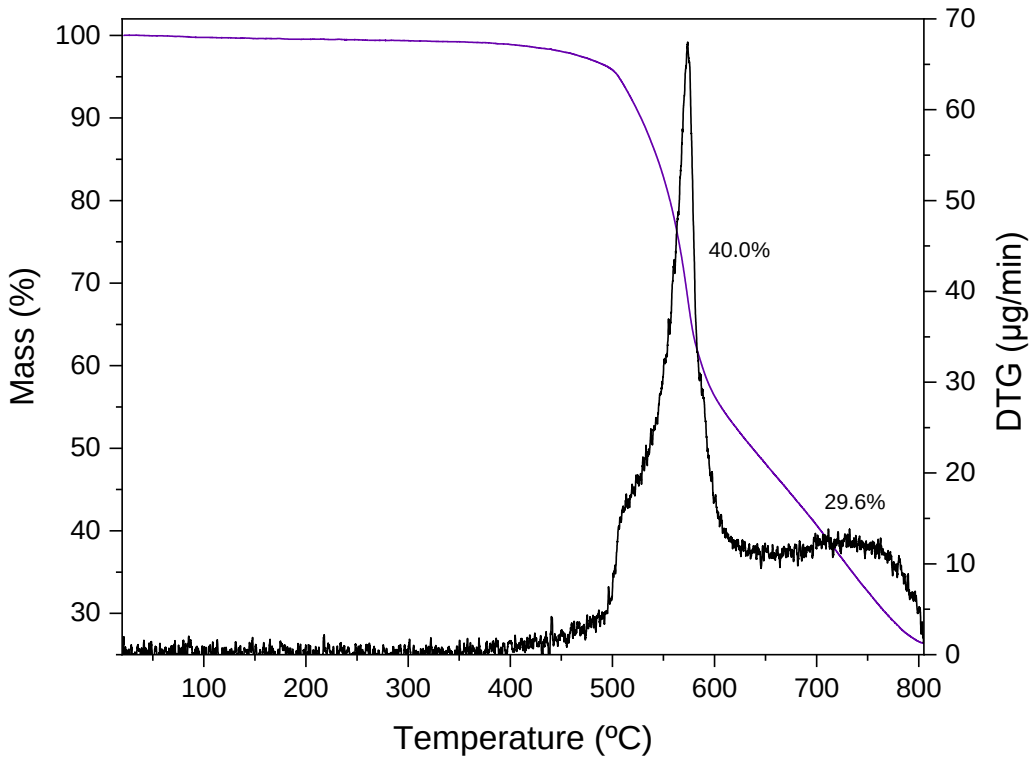

Figure 3.24. TG and DTG curves of ZIF-67(Co).

3.5.4. SEM/EDS

The morphology and particle size of ZIF-67(Co) were investigated by SEM. The SEM micrographs, shown in Figure 3.25, revealed large particles at a micrometric scale with a well-defined truncated rhombic dodecahedral shape, which is characteristic of ZIF-67(Co) materials produced under the same synthetic conditions and it is also in agreement with the results from PXRD.[142] From the SEM micrographs we gathered that the particle size distribution in the sample is polydisperse, with an average particle size of 19.1 ± 6.0 µm.

The elemental composition of ZIF-67(Co) was evaluated by EDS analysis. The obtained EDS spectrum, shown in Figure 3.26, revealed the existence of cobalt and nitrogen arising from the metal centres and the 2-methylimidazolate linkers, respectively, confirming the elemental composition of the sample.

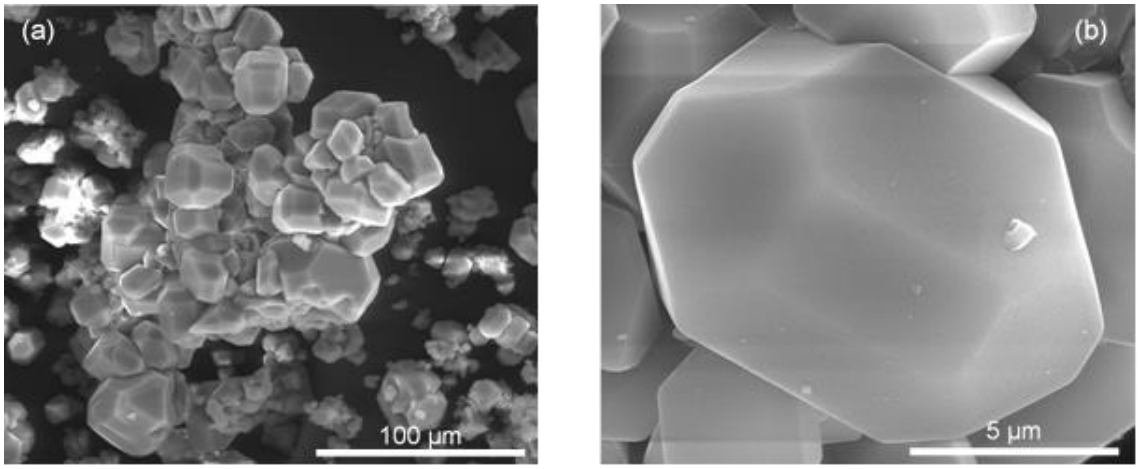

Figure 3.25. SEM micrographs of ZIF-67(Co) at different magnifications (a) 1,000 x, (b) 15,000 x.

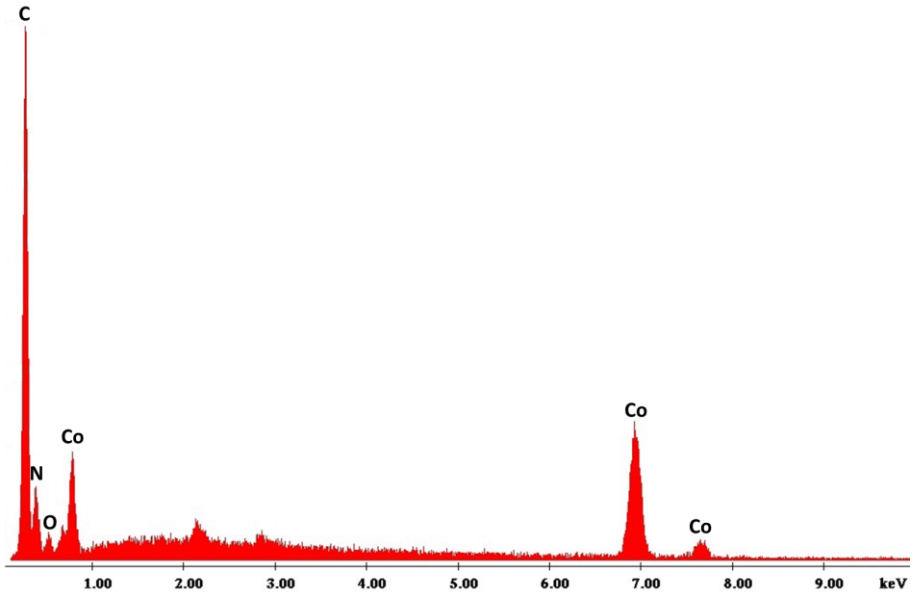

Figure 3.26. EDS spectrum of ZIF-67(Co).

4. Magnetic materials characterization

4.1. Magnetic nanoparticles (MNPs)

4.1.1. PXRD

The as-synthetized iron oxide particles were characterized by PXRD in order to obtain information about their crystalline structure and hence evaluate the effectiveness of the synthetic procedure. As displayed in Figure 4.1, the experimental diffraction pattern is in agreement with the simulated pattern, presenting characteristic peaks at 2θ values of 30.3º, 35.5º, 43.3º, 57.1º and 62.7º, which correspond to the (220), (311), (200), (511) and (440) crystallographic planes of iron oxides with a cubic spinel structure (Fe_3O_4) indexed to the space group $Fd\bar{3}m$.[205] These results confirm that the Fe_3O_4 nanoparticles were successfully synthetized via co-precipitation method. The broadening of the experimental diffraction peaks may be due to the small sizes of the crystalline nanoparticles.[206]

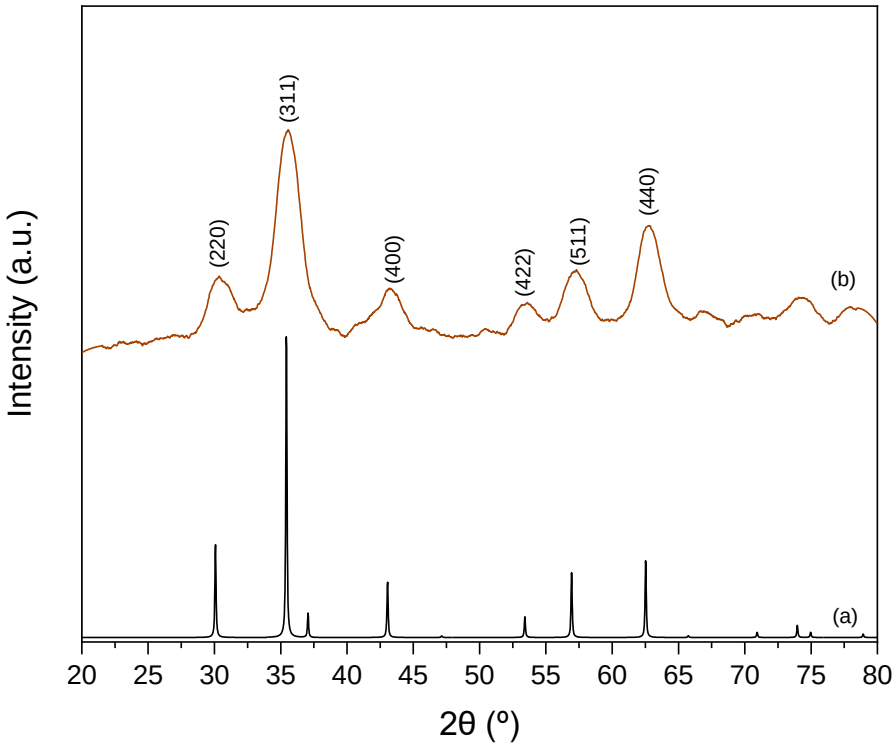

Figure 4.1. PXRD pattern of Fe_3O_4 nanoparticles (a) simulated and (b) as-synthesized.

4.1.2. FT-IR

The molecular structure of the Fe_3O_4 nanoparticles was evaluated by FT-IR and the obtained spectrum is presented in Figure 4.2. The strong vibrational bands at 580 cm^{-1} and 426 cm^{-1} are related to the characteristic Fe–O stretching vibrational modes of the tetrahedral and octahedral sites in the Fe_3O_4 structure, respectively.[140] The broad vibrational band centred at 3435 cm^{-1} and the less intense band at 1628 cm^{-1} can be attributed to the stretching and in-plane bending vibrational modes of the O–H bond respectively. This could be from water molecules adsorbed at the surface of the nanoparticles or surface hydroxyl groups.[143, 205]

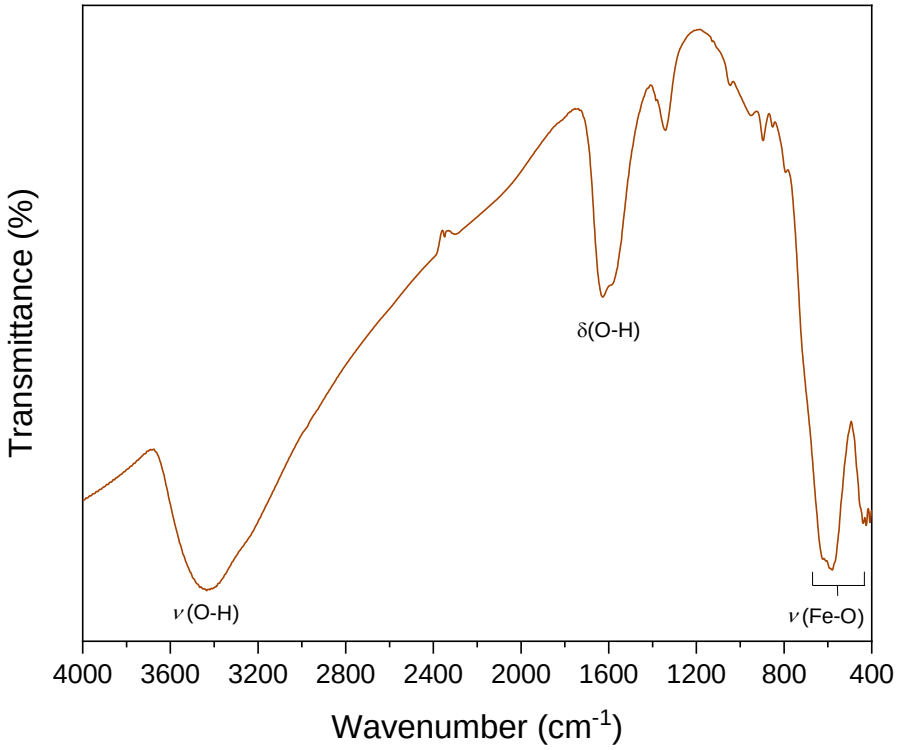

Figure 4.2. FT-IR spectrum of the as-synthesized Fe_3O_4 nanoparticles.

4.1.3. SEM/EDS

Figure 4.3 displays the SEM micrographs of the Fe_3O_4 nanoparticles at different magnifications, revealing information about their morphology and particle size. The micrographs show agglomerated nanoparticles with nearly spherical appearance and an average diameter of 19 ± 4 nm.[140, 143] However, the micrographs were acquired at magnifications close to the limit of resolution of the microscope, making it difficult to discern between adjacent particles as separate entities.

The chemical composition of the nanomaterial was investigated by EDS analysis. The corresponding EDS spectrum, shown in Figure 4.4, confirmed that the nanoparticles are composed of iron and oxygen. However, the ratio between these two elements cannot be accurately determined, due to potential external influences regarding the relative abundance of oxygen. The obtained Si peak is from the silicon wafer used as a support for the deposition of an ethanolic suspension of the Fe_3O_4 nanoparticles.

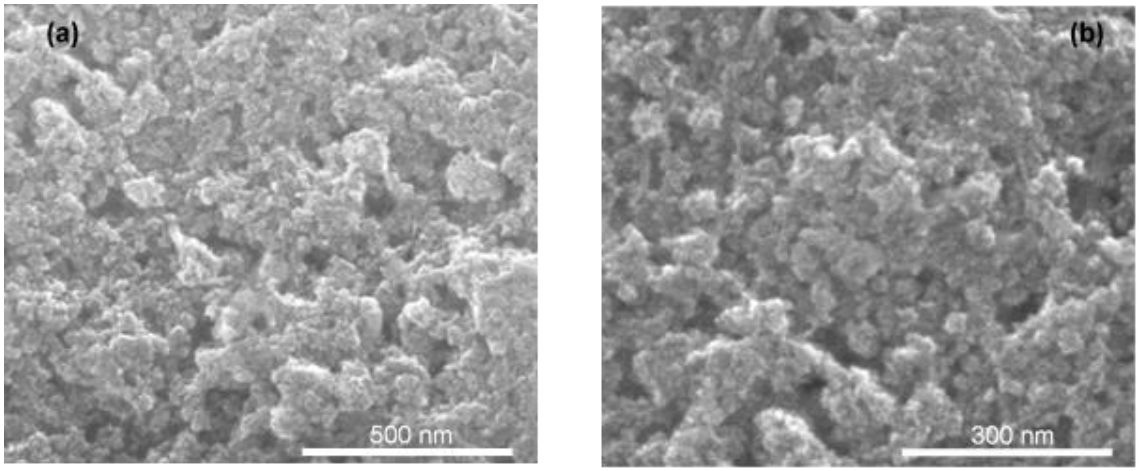

Figure 4.3. SEM micrographs of Fe_3O_4 nanoparticles (a) 200,000x and (b) 300,000x.

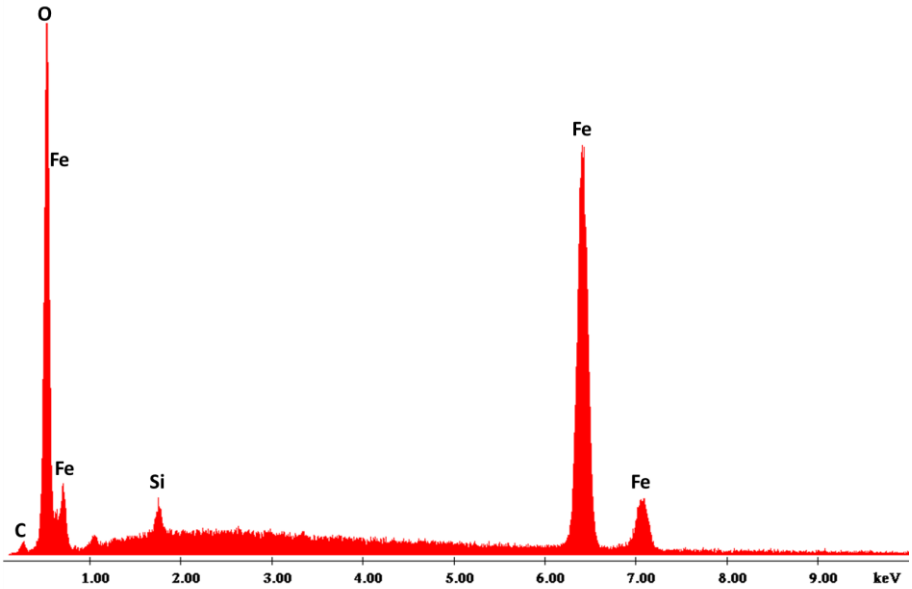

Figure 4.4. EDS spectrum of Fe_3O_4 nanoparticles.

4.1.4. Dynamic Light Scattering and Electrophoretic Light Scattering (DLS/ELS)

A dispersion of Fe_3O_4 nanoparticles was prepared in ultrapure water under sonication, in order to determine the average particle sizes and the zeta potential (ζ)

through DLS and ELS, respectively. The distribution of the hydrodynamic diameter (D_h) of the particles is represented by number in figure 4.5. The obtained results show a log-normal monomodal distribution with an average D_h of 134 ± 14 nm and polydispersity index (PDI) of 0.3 ± 0.1. The D_h of a particle corresponds to the size of a theoretical sphere, including the dispersed particle and additional layers of adsorbed ions at the particle surface. Thus, the diameter measured by DLS is usually higher than the actual diameter of the particle.[143, 207]

The surface charge of the nanoparticles determined with ELS shows that they have a ζ-potential of -10 ± 2 mV at neutral pH (pH = 7.08). Usually, dispersions with colloidal stability have ζ-potential values above + 30 mV or below -30 mV, hence the ζ-potential of the prepared dispersion is in the region of colloidal instability. This suggests that the dispersed nanoparticles tend to form larger agglomerates, which could further explain why the average size measured by DLS is much higher than the one obtained by SEM. Table 4.1 summarizes the average size of the Fe_3O_4 nanoparticles determined by SEM and DLS as well as the ζ-potential average value.

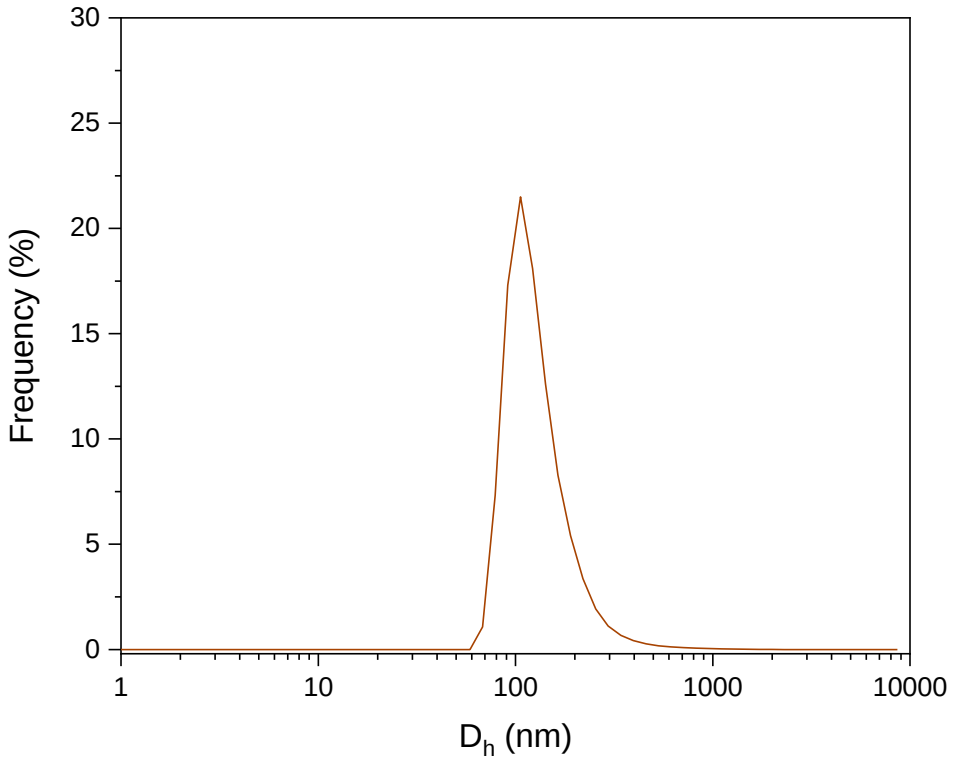

Figure 4.5. Distribution of the hydrodynamic diameter of Fe_3O_4 nanoparticles in solution at 25 ºC.

Table 4.1. Average particle size determined by SEM and DLS, and ζ-potential value at pH = 7.08.

***ζ*-potential /mV**	***D*$_{h\ DLS}$ /nm**	***d*$_{SEM}$ /nm**
-10 ± 2	134 ± 14	19 ± 4

4.2. MIL-53(Fe)-based magnetic composite

4.2.1. PXRD

The synthesis of the magnetic composite of MIL-53(Fe) resulted in two products with distinct colours, so to distinguish them, they were denominated as MIL-53Y (yellow) and MIL-53R (red) and characterized in separate. Their crystalline structures were analysed by PXRD and the resulting patterns were compared with the experimental data obtained for pristine MIL-53(Fe) and Fe_3O_4 nanoparticles, as illustrated in Figure 4.6.

An examination of the XRD patterns of the two composite materials in the 2θ range of 5-27º revealed that all diffraction peaks assigned to the characteristic Bragg reflections of the starting MOF were preserved. This indicates that the introduction of MNPs into the reactional mixture did not had a significative influence in the formation of the MIL-53(Fe) crystalline phases.[140]

At higher 2θ angles (> 30º), additional diffraction peaks are observed related to the main reflections of the Fe_3O_4 nanoparticles in the pattern of MIL-53R, while in the MIL-53Y pattern no diffraction peaks were detected. This suggests that, during MIL-53Y synthesis, the MOF framework was successfully formed around the MNPs resulting in their encapsulation into the framework structure, while in MIL-53R products, the MNPs were preferentially attached to the surface of the MOF rather than inside the porous structure.[208]

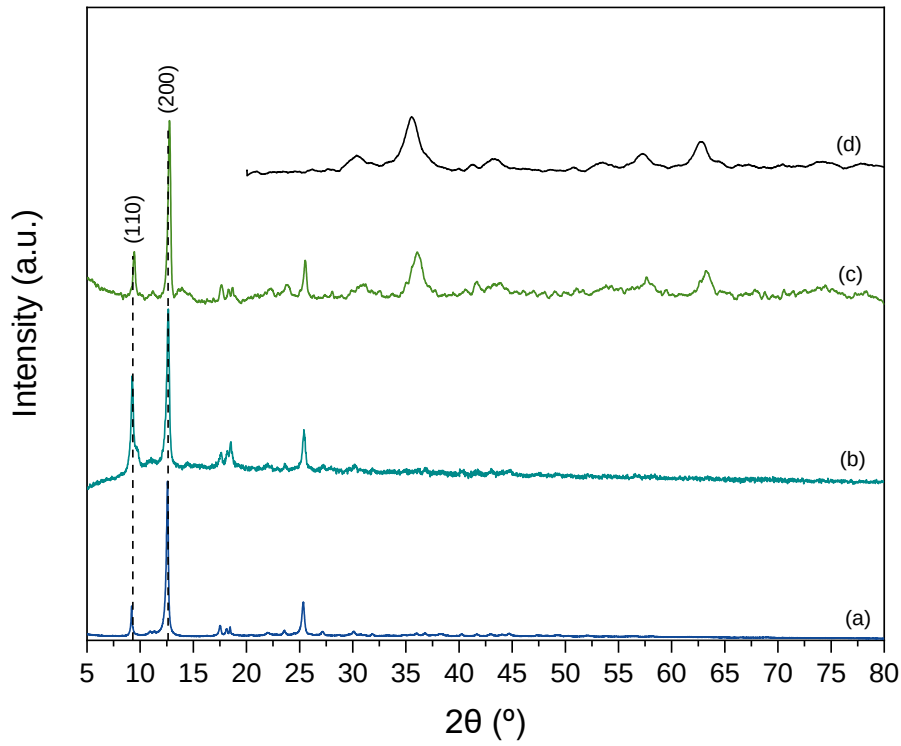

Figure 4.6. PXRD pattern of (a) pristine MIL-53(Fe), (b) MIL-53Y, (c) MIL-53R and (d) Fe_3O_4 nanoparticles.

4.2.2. FT-IR

The molecular structure of both magnetic composites was characterized by FT-IR and the obtained spectra were compared with the infrared spectrum of the starting MOF, as demonstrated in Figure 4.7. Both materials present typical vibrational bands of the parent MOF, although some differences were detected in the absorption bands regarding their position, shape and intensity, that can provide some insight about the molecular interactions between the framework and the MNPs. The two intense absorption peaks at 1537 cm^{-1} and 1394 cm^{-1} can be assigned to the asymmetric and symmetric stretching of the O–C–O bond of the coordinated carboxylate groups in the MIL-53R and pristine MIL-53(Fe) spectra. In the MIL-53Y spectrum, the absorption peak corresponding to the asymmetric stretching vibrational mode of the carboxyl groups is shifted towards higher energies (1550 cm^{-1}). This could be due to the influence of hydrogen bonding interactions between the carboxylic groups of the framework and the hydroxyl groups at the surface of the MNPs. The absorption peak at 748 cm^{-1} observed in both composite spectra can be assigned to =C-H bending vibrational mode of the benzene rings from the organic linkers, and their relative intensities are weaker than in the spectrum of the starting MOF.[140, 193]

The vibrational band attributed to the Fe–O stretching vibrational mode of the metal-oxo clusters in the spectrum of MIL-53R seems to be broader and shifted by 27 cm^{-1} to higher wavenumber. This may have been caused by the overlap with the characteristic vibrational band assigned to the stretching vibrations of the Fe–O bond of the MNPs, that usually appear around 580 cm^{-1}.[140] Therefore, the results of XRD combined with the information gathered from the obtained infrared spectra confirm the co-existence of Fe_3O_4 and MIL-53(Fe) components in the magnetic composites.

The MIL-53R spectrum also presents an additional intense vibrational band at 1693 cm^{-1} that can be attributed to the stretching vibrational mode of the carbonyl group, from protonated terephthalic acid molecules. This suggests the existence of free organic linkers that were not removed by the purification process.[185]

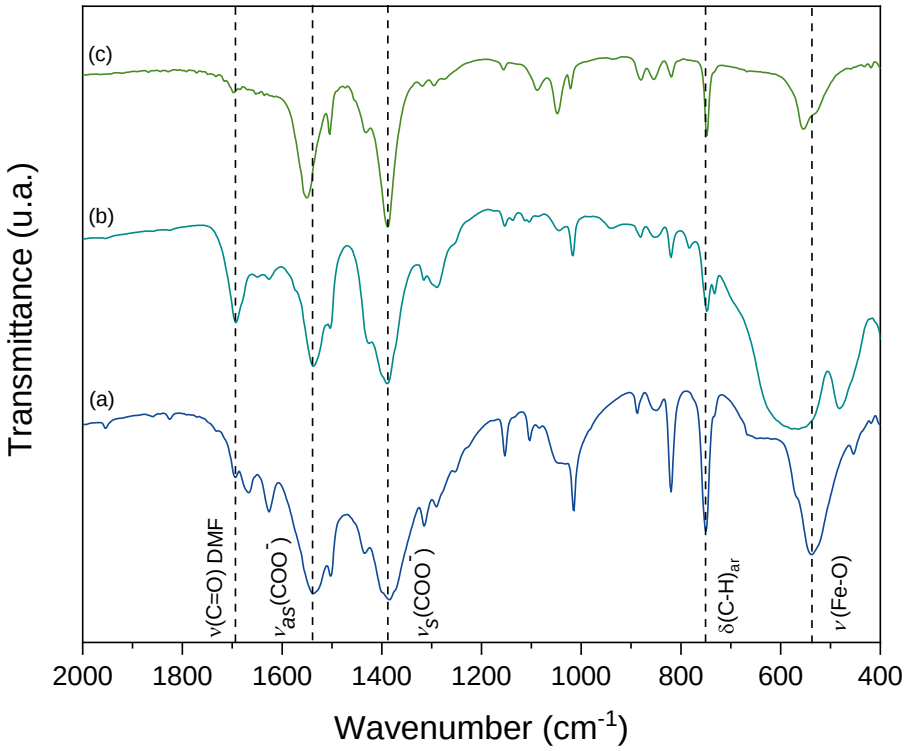

Figure 4.7. FT-IR spectrum of (a) pristine MIL-53(Fe), (b) MIL-53R and (c) MIL-53Y.

4.2.3. TGA

The thermal stability of the magnetic composites MIL-53Y and MIL-53R was also investigated and the resulting TG curves are represented in Figure 4.8 and 4.9, respectively. Both thermogravimetric profiles are very similar to the one of the parent MOF shown in Figure 3.19, revealing that both composites are thermally stable up to 250 ºC, as the pristine MIL-53(Fe). However, for MIL-53R a total mass loss of ~18% was only observed, while MIL-53Y revealed a total mass loss of ~62%. Previously reported studies have proven that the Fe_3O_4 nanoparticles are thermally stable up to 800 ºC. Thus, the amount of mass losses observed in both composite materials are probably only due to the MOF component and the release of guest molecules, suggesting that MIL-53R sample presented less content of MOF than the MIL-53Y composite. [209]

Through a further analysis of the TG curves of both composites, minor mass losses were observed below 250 ºC, which could correspond to the release of water and DMF guest molecules physiosorbed at the materials surface. As the temperature increased up to 500 ºC, it led to mass losses of ~41% in MIL-53Y and ~14% in MIL-53R, which could be attributed to the decomposition of the coordinated terephthalate linkers and subsequent collapse of the framework structure. Above 500 ºC, further mass losses were

detected, which could be due to the decomposition of the remaining organic content and formation of iron oxides from the inorganic building units.[193-194]

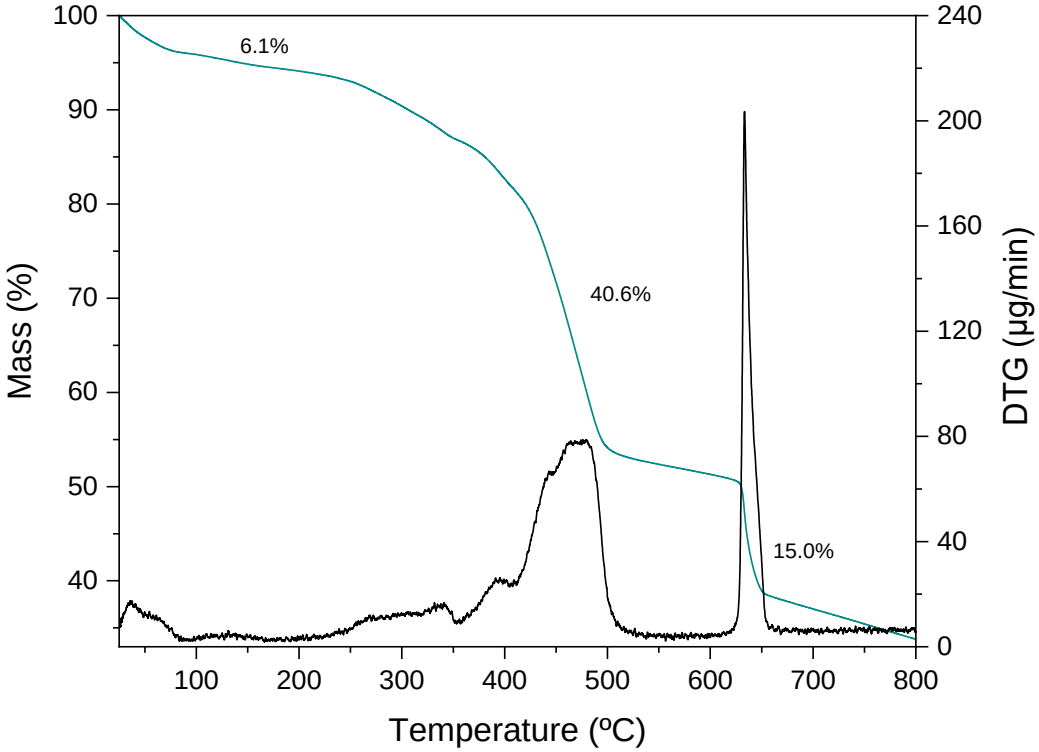

Figure 4.8. TG and DTG curves of MIL-53Y.

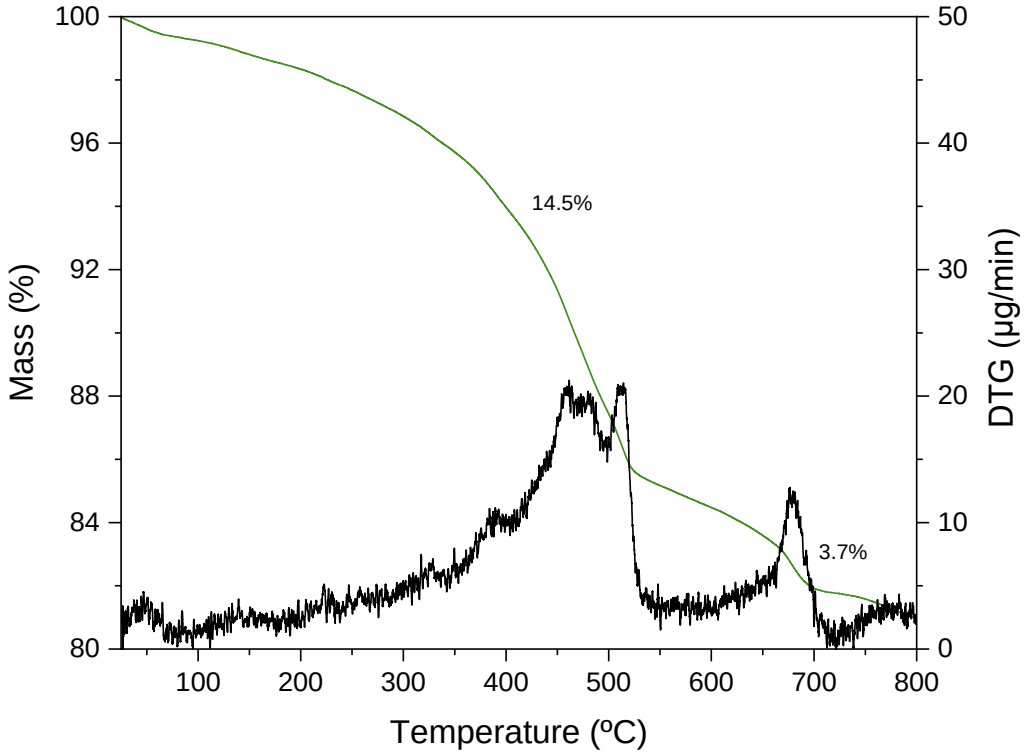

Figure 4.9. TG and DTG curves of MIL-53R.

4.2.4. SEM/EDS

The SEM characterization of both magnetic composites provided valuable information regarding the differences between their morphology, particle size and distribution of the MNPs over the sample.

The SEM micrographs of the MIL-53R composite displayed in Figure 4.10 revealed a wide diversity of particles with different sizes and shapes. Some particles presented the typical morphology of the parent MOF demonstrated in section 3.4.4., with an average length of 15.0 ± 9.0 µm and width of 7.1 ± 5.0 µm. The average size of the composite particles is lower than the previously reported values for the pristine MOF (43.8 ± 18.0 µm in length and 17.6 ± 6.0 µm in width), which could be an indicator that the MNPs presence affected the extent of the self-assembly process of the framework, leading to a decrease of the particles size in comparison with the starting MOF. The other portion of the sample is constituted by smaller particles with nearly spherical shape, at a nanometric scale, widely distributed throughout the sample. These nanoparticles were either attached to the surface of the MOF particles or agglomerated into clusters with different sizes and shapes.

In contrast with what was observed for MIL-53R, the SEM micrographs of MIL-53Y (Figure 4.12) revealed a uniform distribution of rod-like shaped particles and almost none MNPs attached to the microrods surface, suggesting that the encapsulation of the nanoparticles was favoured. The morphology of the magnetic composite MIL-53Y was very similar to the one observed for the pristine MIL-53(Fe). The average particle size was 21.7 ± 4.0 µm in length and 3.9 ± 1.0 µm in width, which is also lower than the dimensions observed for the parent MOF.

The results gathered though the micrographs seem to be in agreement with the ones obtained through XRD and TGA, confirming that the MNPs are in fact spread over the surface of the MOF in MIL-53R composite rather than inside the porous framework as in MIL-53Y. It was also revealed that the MOF/MNPs ratio appear to be lower in the MIL-53R sample than in MIL-53Y, which further explains the considerable difference between the total percentage of mass loss observed in both composites.

The chemical composition of each composite was assessed by EDS and the corresponding spectra of MIL-53R and MIL-53Y are represented in figure 4.11 and 4.13, respectively. The EDS analysis revealed that both composites had similar elemental compositions, being mainly composed by iron, carbon, and oxygen, as expected. However, given that the micrographs of MIL-53R uncovered the existence of two different components, an EDS analysis was performed for each region. The resulting spectra showed that both components were composed by iron, but the spectrum corresponding

to the region where the nanostructures were more abundant revealed that that area had a higher relative abundance of iron than the region related to the elongated structures.

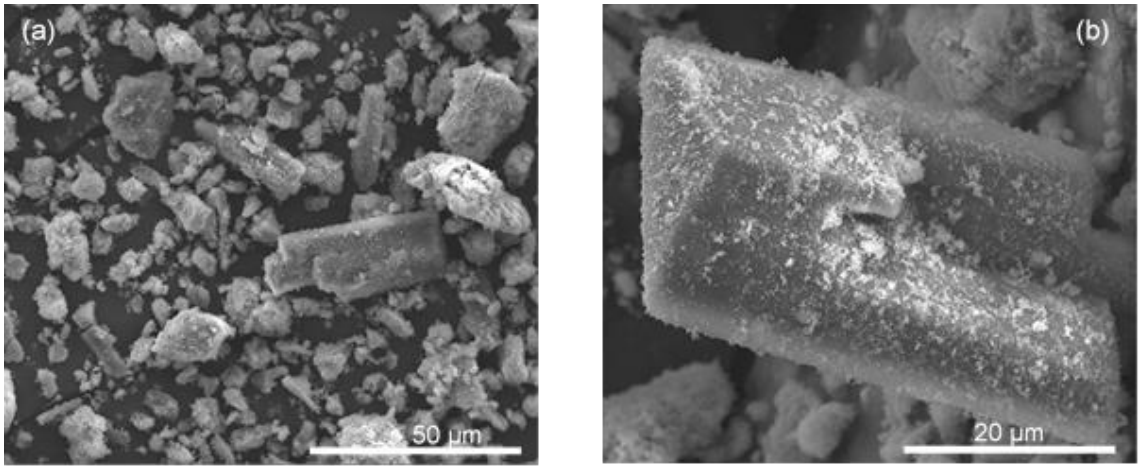

Figure 4.10. SEM micrographs of MIL-53R at different magnifications (a) 2,000x and (b) 5,000x.

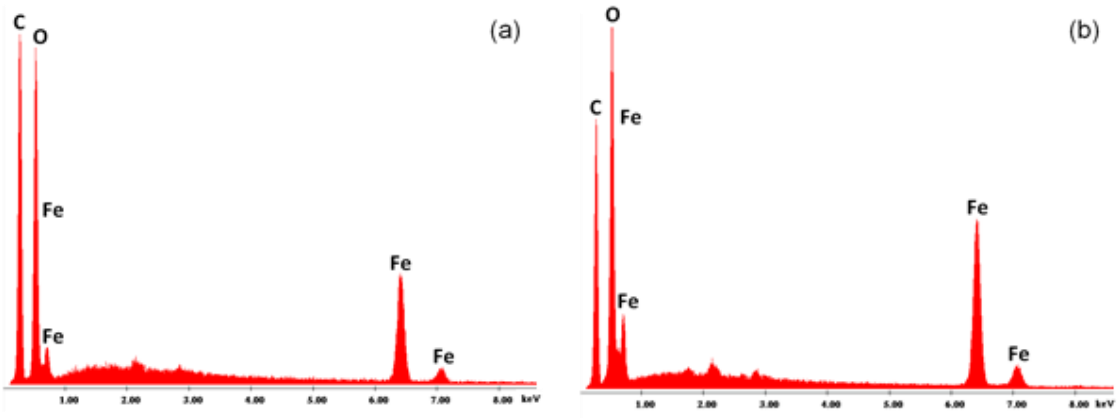

Figure 4.11. EDS spectra of two different regions in MIL-53R composite (a) microrods and (b) nanospheres.

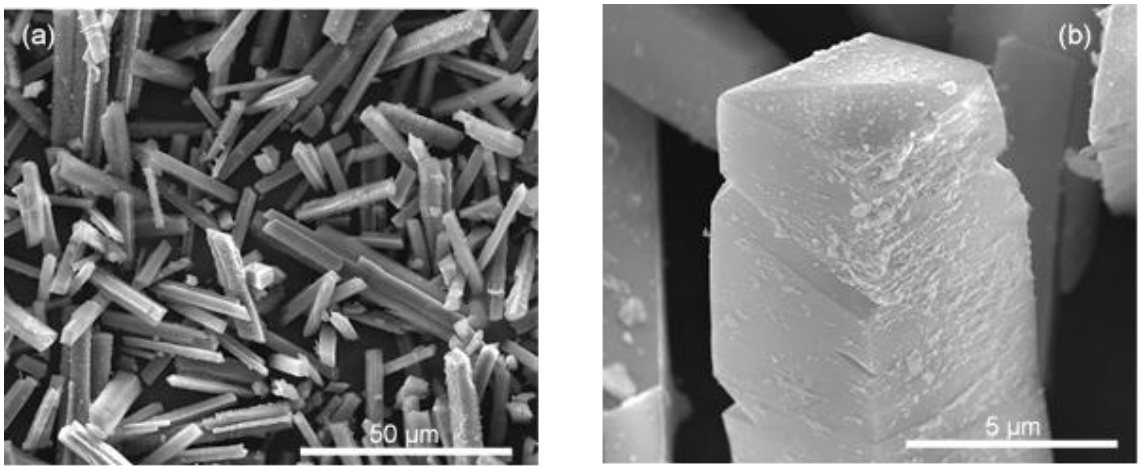

Figure 4.12. SEM micrographs of MIL-53Y at different magnifications (a) 2,000x and (b) 20,000x.

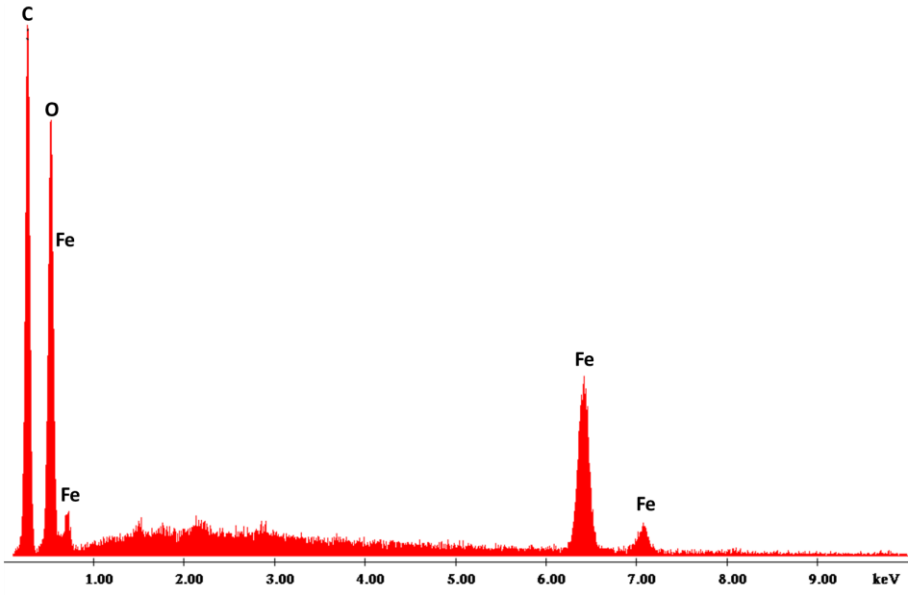

Figure 4.13. EDS spectrum of MIL-53Y composite.

4.3. ZIF-derived porous carbon

4.3.1. PXRD

The pyrolysis of ZIF-67(Co), at 600 ºC under inert atmosphere, resulted in a cobalt/N-doped porous carbon composite and was denominated as ZIF-DPC. The crystallographic structure of the material was characterized by PXRD and the resulting experimental pattern was compared with the simulated patterns of pure graphite and cobalt crystals, as shown in Figure 4.14.

The broad peak at 2θ = 26.5º is attributed to the typical (002) interlayer plane reflection of graphitic carbon, confirming the formation of a carbon matrix with a graphitic structure from the organic content of ZIF-67(Co) upon heating to 600 ºC. The intense diffraction peak at 2θ of 44.5º and the less intense diffraction peaks at 51.9º and 76.5º correspond to the (111), (101) and (211) crystallographic reflections, respectively. These reflections are characteristic of cobalt face centred cubic (*fcc*) structures, indicating the presence of metallic cobalt crystals in the composite material. The gathered results confirmed that the pyrolysis of ZIF-67(Co) led to the successful formation of a composite material composed by graphitic carbon matrix and crystalline metallic cobalt particles.[144, 210]

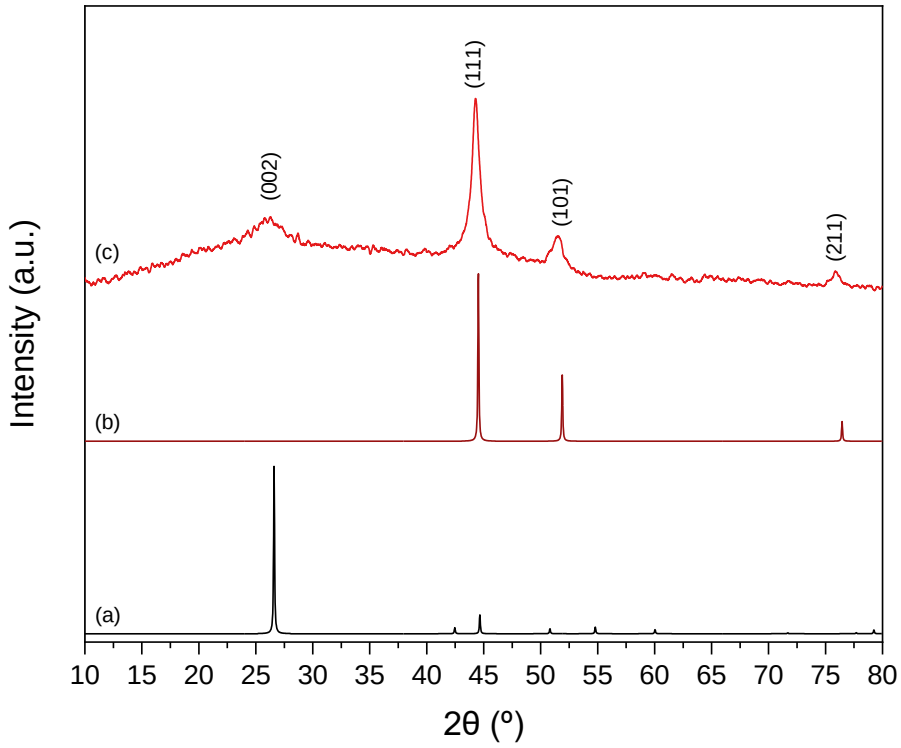

Figure 4.14. PXRD patterns of (a) simulated graphitic carbon structure, (b) simulated pure cobalt crystals and (c) ZIF-DPC.

4.3.2. FT-IR

The prepared ZIF-DPC was characterized by FT-IR in order to investigate its molecular structure and compare the resulting infrared spectrum with the one from the precursor ZIF-67(Co) (Figure 4.15). All the vibrational bands that belong to the fingerprint region assigned to the molecular structure of ZIF-67(Co) disappeared after the thermal treatment, indicating that the carbonization of the functional groups present in the ZIF-67(Co) structure was effective. The appearance of broad and weak vibrational bands was observed instead, as a result of the small differences between the electronegativity of the chemical elements in the C–C and C–N bonds, that lead to weak dipole moments and consequently result in low absorptions of the infrared radiation. [211]

The sharp band at 1386 cm^{-1} can be assigned to the bending vibrational mode of the O–H bond from physiosorbed water molecules at the surface of the material.[212] The broad vibrational bands at 1622 cm^{-1} and 1040 cm^{-1} can be ascribed to the stretching vibrational mode of the C=C and C–N bonds, respectively.[213-214] This confirms that the pyrolysis of ZIF-67(Co) resulted in a N-doped carbon matrix. Moreover, the broad absorption peak at 600 cm^{-1} can be attributed to the stretching vibrational mode of the Co–O bonds. This could have resulted from a partial oxidization of the Co particles, owing to their mild reactive behaviour when exposed to oxygen.[144]

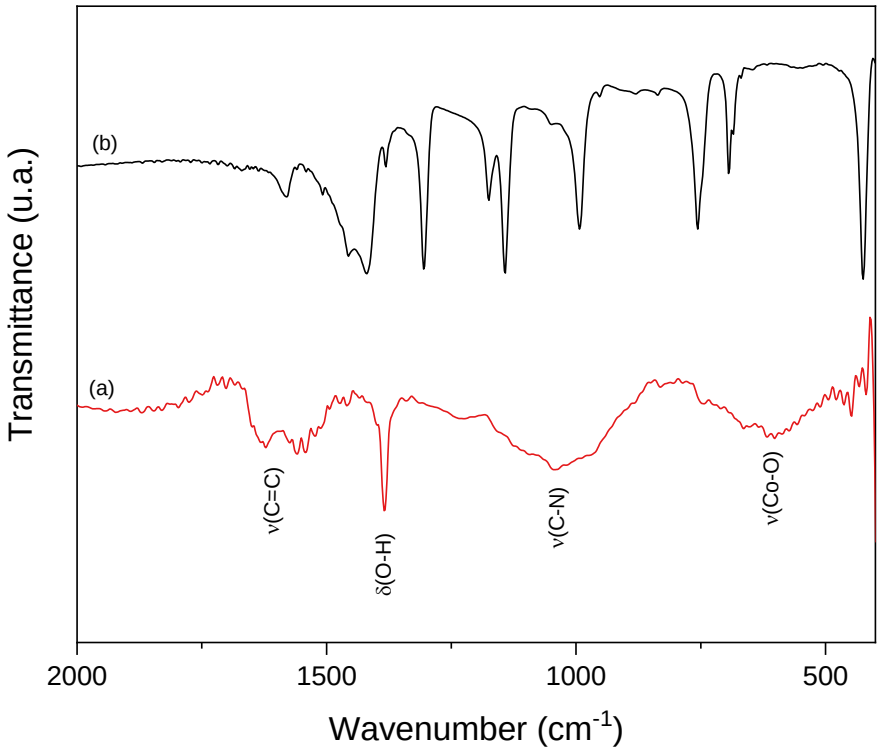

Figure 4.15. FTIR spectrum of (a) ZIF-DPC and (b) ZIF-67(Co).

4.3.3. TGA

The thermal behaviour of ZIF-DPC was assessed by TGA and the resulting TG and respective DTG curves are presented in Figure 4.16. As the temperature increases up to 800 ºC, a two-stepped total mass loss of ~22% can be observed. The first mass loss of ~8% occurred between 25 ºC and 120 ºC and could be assigned to the volatilization of water molecules adsorbed at the surface and inside of the material cavities. The second mass loss stage occurred from 400 ºC up to 800 ºC and could be attributed to the decomposition of residual amounts of 2-methylimidazolate linker from ZIF-67(Co) material that was not completely carbonized in the pyrolysis process along with the formation of metallic cobalt particles resulting in ~17 % of mass loss.

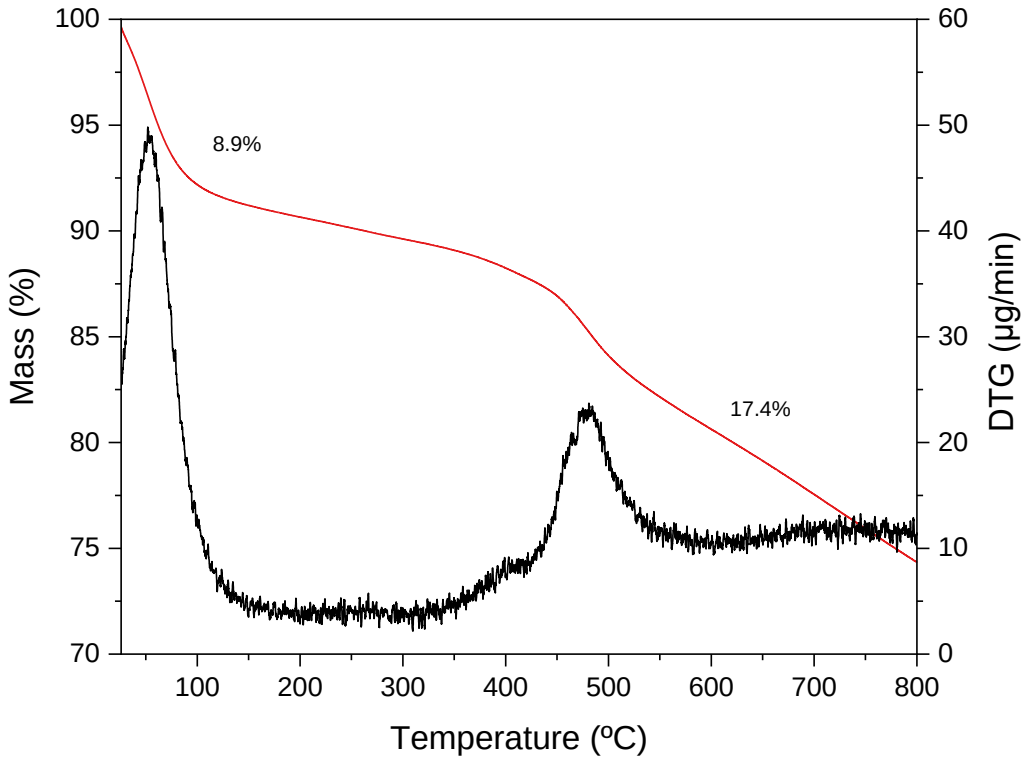

Figure 4.16. TG and DTG curves of ZIF-DPC.

4.3.4. SEM/EDS

The morphology and particle size of ZIF-DPC was characterized by SEM and the resulting micrographs are displayed in Figure 4.17. The obtained micrographs revealed that the ZIF-DPC particles partially maintained the rhombic dodecahedral morphology of the ZIF-67(Co) precursor. The average particle size was 4.9 ± 2.0 µm, which is considerably lower than the average size of ZIF-67(Co) particles (19.1 ± 6.0 µm). This could be due to the partial collapse of the particle framework structure during the pyrolysis process, thus leading to a decrease of the overall average size of the particles. The gathered results are in good agreement with previously reported works, confirming the successful preparation of the material.[144, 210, 213]

The chemical composition of the sample was acquired through EDS analysis and the resulting spectrum is presented in Figure 4.18. The EDS analysis revealed the presence of cobalt and nitrogen, which are unequivocally attributed to the chemical composition of the sample, confirming the successful preparation of Co/N-doped carbon materials. The high relative abundance of the carbon could be a consequence of the presence of the graphite structures that were identified in the experimental PXRD patten. However, given that the sample was fixed in a double-sided carbon tape, the carbon relative abundance cannot be only assigned to the material composition. Moreover, the presence of oxygen

in the sample, could be a result of partially oxidized Co particles, since they are described in the literature as moderately reactive species and tend to form cobalt monoxide when exposed to an oxidizing atmosphere.[144]

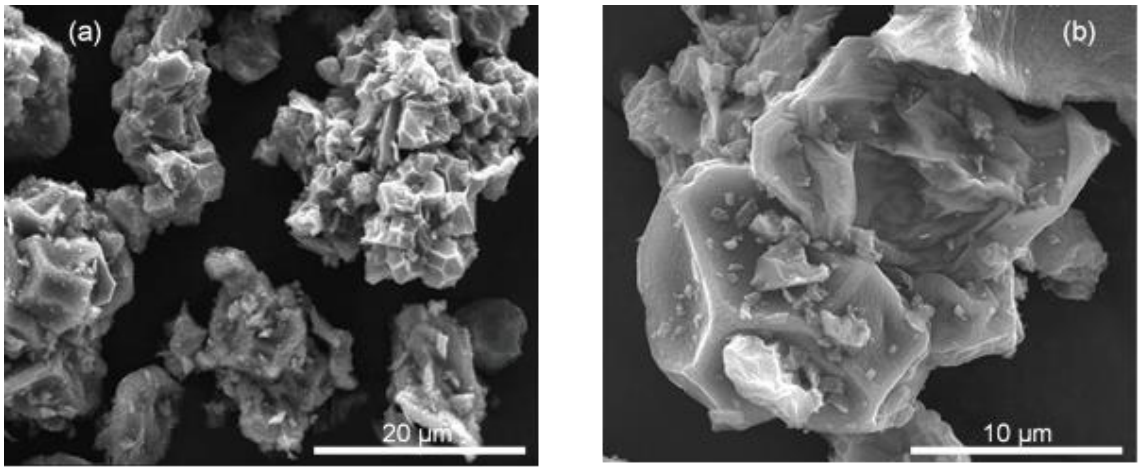

Figure 4.17. SEM micrographs of ZIF-DPC at different magnifications (a) 5,000x and (b) 10,000x.

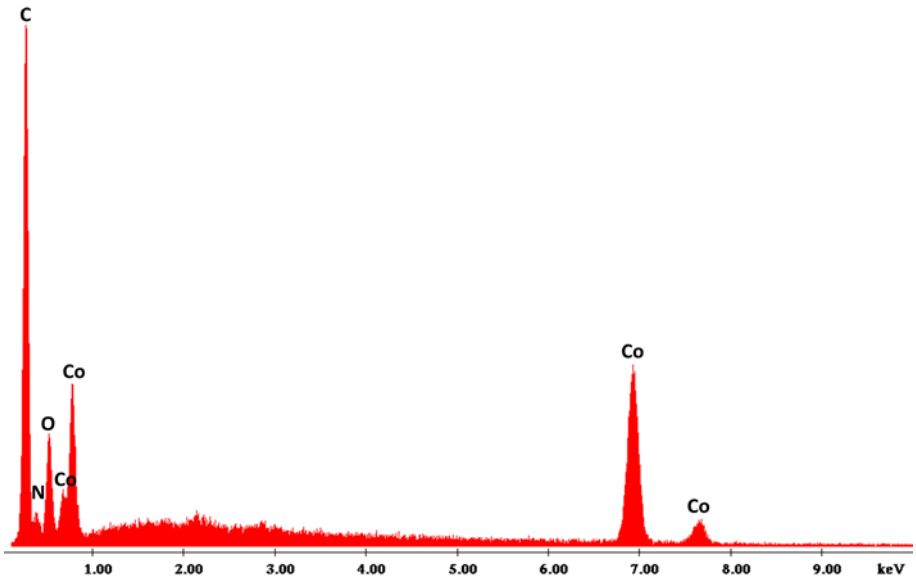

Figure 4.18. EDS spectrum of ZIF-DPC.

5. Heavy metal adsorption studies

5.1. Adsorbents characterization

Besides knowing the chemical nature of the adsorbate, it is important to study the physicochemical properties of the adsorbents, such as their surface charges and specific surface areas, since it may have a major influence on their adsorption capacities towards different adsorbates. Moreover, the study of these properties is useful to gather further insight into the most plausible mechanisms through which the adsorption processes occur. Thus, before the adsorption studies *per se,* the specific surface area and surface charge of the materials were evaluated through N_2 adsorption/desorption studies and by the determination of the pH at point of zero charge (pH_{ZPC}), respectively.

From all synthetized and characterized materials, MIL-88B(Fe), MIL-53(Fe), MIL-100(Fe), ZIF-67(Co) and ZIF-DPC were selected as adsorbents to pursue the adsorption studies. Their higher yielding syntheses over MIL-88A(Fe), MIL-53Y and MIL-53R, provided sufficient amount of sample to carry out all adsorption experiments.

5.1.1. pH at point of zero charge (pH_{ZPC})

Whenever adsorption studies are performed, it is important to be aware of the solution pH and the corresponding surface charge of the adsorbent material, especially when the adsorbates in study are charged species, such as heavy metal ions.

The pH_{ZPC} is described as the pH at which the surface charge density of a given material equals zero, i.e., when there are equivalent amounts of positive and negative charges at the surface of the material. Therefore, this parameter can give us valuable insights regarding the acidity/basicity and surface charge of the material upon varying the initial pH of the solution. If the solution pH is below the pH_{ZPC} value of a given material, its surface is positively charged, and if it is above, it is negatively charged.

The pH_{ZPC} value of each adsorbent was determined through the experimental procedure previously mentioned in section 2.4.1. Then, the differences between the final and initial pH values were evaluated within an initial pH range of 2-10. Afterwards, the gathered data was plotted against the initial pH and then, the pH_{ZPC} values were calculated by interpolation, through a linear regression model adjusted to each curve.

Figure 5.1 represents the ΔpH vs $pH_{initial}$ curves of MIL-88B(Fe), MIL-100(Fe), MIL-53(Fe), ZIF-67(Co) and ZIF-DPC and the corresponding pH_{ZPC} values are summarized in Table 5.1. There is an evident difference between the pH_{ZPC} values of the materials composed by carboxylate-based linkers, such as MIL-88B(Fe) (pH_{ZPC} = 2.9), MIL-

100(Fe) (pH_{ZPC} = 4.5) and MIL-53(Fe) (pH_{ZPC} = 4.2), and the ones containing nitrogen-based groups in their structure, such as ZIF-67(Co) (pH_{ZPC} = 9.1) and ZIF-DPC (pH_{ZPC} = 7.6). This phenomenon could be due to the difference between the acid/base properties of the organic moieties present in the framework of these materials. Usually, the carboxylic acid groups are associated with low pK_a values, meaning that the deprotonation of the hydroxyl groups occurs at pH values below 7. As a consequence, the pH_{ZPC} values of the carboxylate-based MOFs appear at low pH. On the other hand, the amine group of the 2-methylimidazole linker of ZIF-67(Co) is only deprotonated at pH values above 7, thus the pH_{ZPC} value associated to this material is shifted towards alkaline pH values. Moreover, the pyrolysis of ZIF-67(Co) led to a decrease of its $pH_{ZPC,}$ from 9.1 to 7.6.

Furthermore, the structure of ZIF-67(Co) revealed to be very susceptible to chemical degradation during the experimental work under acidic conditions, probably due to the hydrolysis of the Co–N bond, causing a total collapse of the crystal structure and subsequent dissolution of the respective precursors. This phenomenon has made it impossible to apply ZIF-67(Co) in the adsorption studies, due to the incompatibility between its chemical stability and the pH range at which the studies were performed.

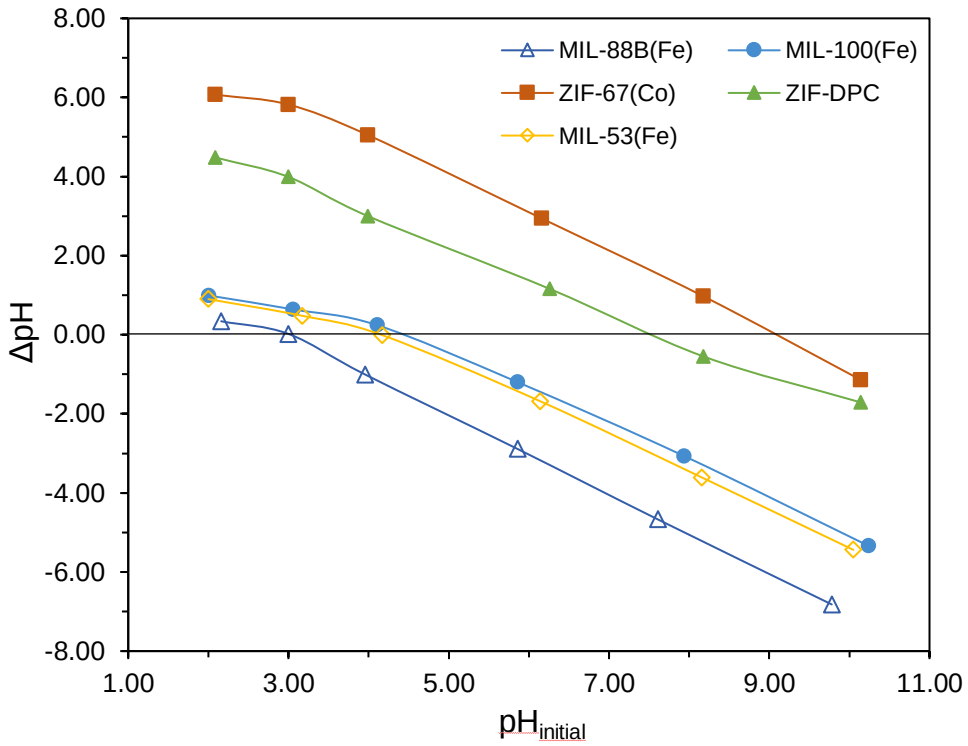

Figure 5.1. Graphical representation of the ΔpH vs $pH_{initial}$ curves of MIL-88B(Fe), MIL-100(Fe), MIL-53(Fe), ZIF-67(Co) and ZIF-DPC

Table 5.1. pH_{ZPC} values and respective standard deviation of each material.

Material	pH_{ZPC}
MIL-88B(Fe)	2.9 ± 0.1
MIL-53(Fe)	4.2 ± 0.2
MIL-100(Fe)	4.5 ± 0.2
ZIF-DPC	7.6 ± 0.3
ZIF-67(Co)	9.1 ± 0.3

5.1.2. N_2 adsorption/desorption isotherms

N_2 adsorption/desorption studies were conducted in order to evaluate the specific surface area and total pore volume of the adsorbents. The N_2 adsorption/desorption isotherms of MIL-100(Fe) and ZIF-DPC are displayed in Figure 5.3 and 5.4, respectively, represented by the amount of N_2 adsorbed, n_{ads} (mmol/g) *vs.* relative pressure (p/p^o). Table 5.2 summarizes the $A_{s,BET}$, V_p and D_p values determined by equations 11 ,12 and 13. Since MIL-88B(Fe) and MIL-53(Fe) revealed low specific surface areas, the presented $A_{s,BET}$ values were estimated from the gathered experimental data, and the small quantity of sample available did not allow to accurately determine the respective V_p and D_p values. Despite these results, we cannot state that MIL-88B(Fe) and MIL-53(Fe) have poor porosity features. The framework structures of these materials are well known by their large breathing behaviour, revealing drastic variations in their cell volumes between dehydrated and hydrated forms without loss of crystallinity or bond breaking, thus keeping their underlying topology.

Given that, before the N_2 adsorption/desorption experiments, the samples went through extensive outgassing procedures (see section 2.5.5.), this could have led to structural transformations in both MIL-88B(Fe) and MIL-53(Fe) frameworks between open pore form (hydrated by physiosorbed water) and closed pore form (dehydrated) (Figure 5.2). According to previously reported studies, the dehydrated form of MIL-53(Fe) is characterized by very narrow pores without accessible porosity to most gases.[101] Moreover, MIL-88B(Fe) upon dehydration exhibits a large contraction behaviour that reduces by 135% its pore volume in comparison with its hydrated form, thus leading to low accessible porosity as well.[215]

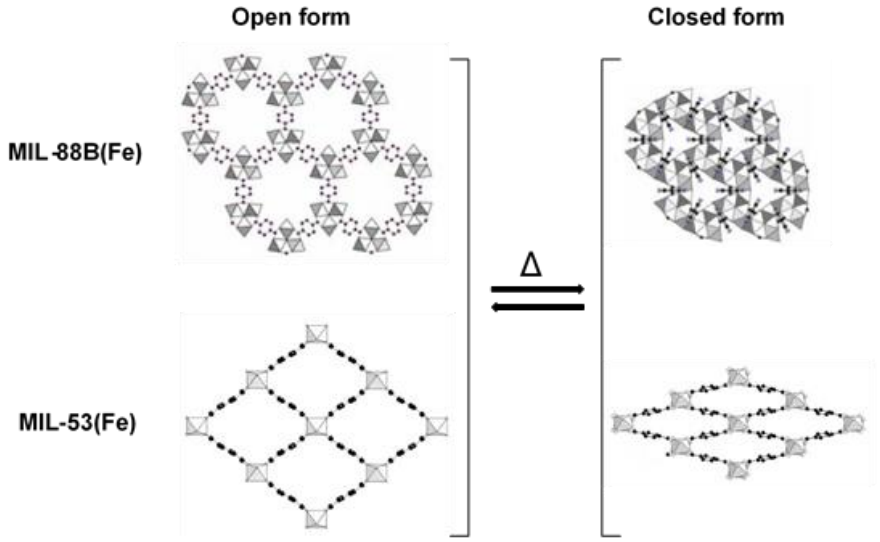

Figure 5.2. Representation of open and closed forms of MIL-88B(Fe) and MIL-53(Fe). Adapted from[132, 216].

The N_2 adsorption/desorption curves of MIL-100(Fe) and ZIF-DPC revealed type IV isotherms, typical of mesoporous materials, with H4 type hysteresis loops characteristic of an edge-shaped pores with a slight microporosity character.[160] Both determined $A_{s,BET}$ and V_p values of each material are in agreement with previously reported works.[136, 144, 168, 174, 217]

Moreover, the ZIF-DPC showed a considerably lower $A_{s,BET}$ value than the corresponding value reported for the ZIF-67(Co) precursor, namely specific surface areas above 1000 m^2/g and total pore volumes at *ca*. 0.80 cm^3/g.[144, 196] As expected, the carbonization procedure leads to a reduction of both specific surface area and total pore volume, 255 m^2/g and 0.14 cm^3/g, respectively.[144] Nevertheless, ZIF-DPC is still a material with promising textural properties, namely high porosity and surface area.

Table 5.2. Summary of the $A_{s,BET}$, V_p and D_p values of each adsorbent.

Material	$A_{s,BET}$ **(m^2/g)**	V_p **at** p/p^o **= 0.95 (cm^3/g)**	D_p **(nm)**
MIL-100(Fe)	1674	0.77	1.8
ZIF-DPC	255	0.14	2.2
MIL-88B(Fe)	40	-	-
MIL-53(Fe)	12	-	-

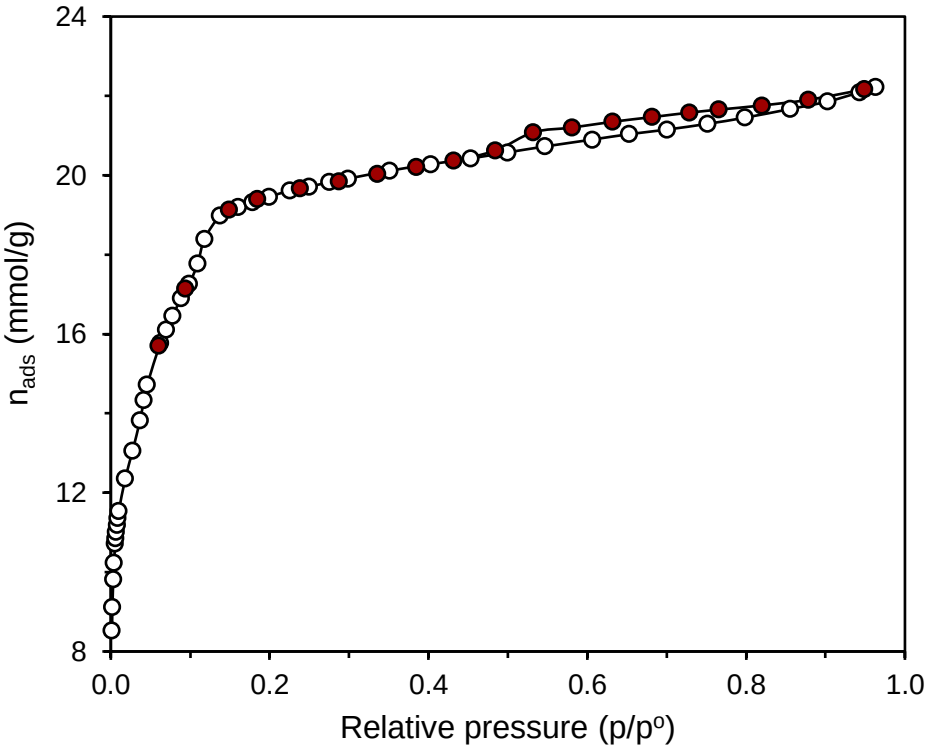

Figure 5.3. N_2 adsorption/desorption isotherm at -196 ºC of MIL-100(Fe). Filled and unfilled symbols represent the adsorption and desorption process, respectively.

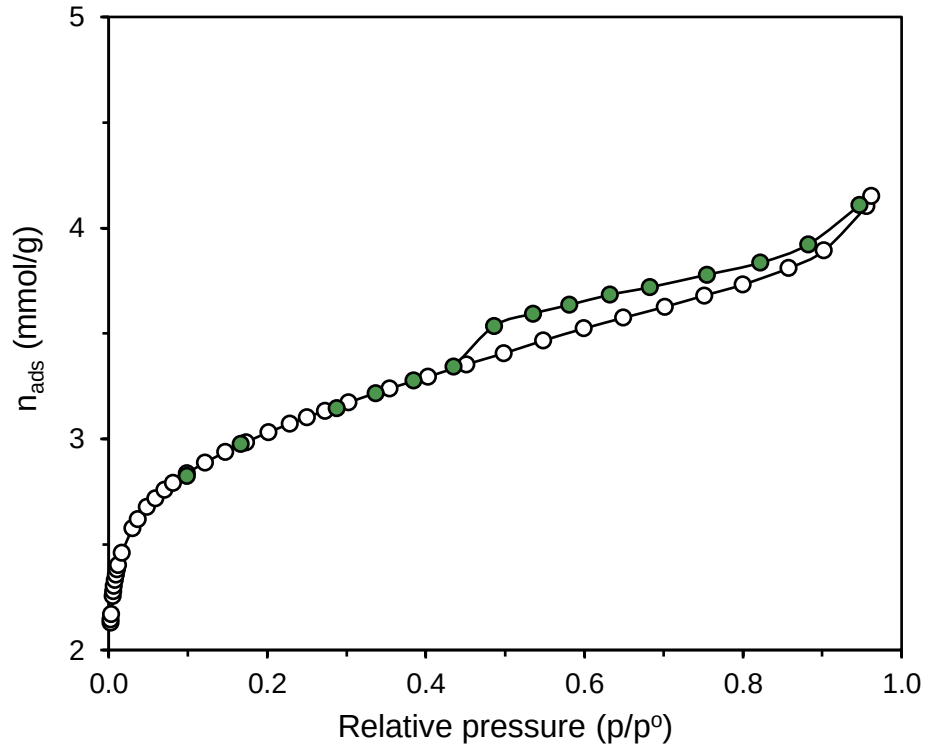

Figure 5.4. N_2 adsorption/desorption isotherm at -196 ºC of ZIF-DPC. Filled and unfilled symbols represent the adsorption and desorption process, respectively.

5.2. Adsorption studies

5.2.1. Effect of adsorbent dosage

The adsorbent dosage is an important parameter that affects the adsorption efficiency of a given material. It is necessary to evaluate the most favourable adsorbent dosage, so that the adsorbent-adsorbate interactions can be maximized, thus avoiding overconsumption of the adsorbent. Usually, the increase of the adsorbent dosage results in higher removal efficiencies, due to the increasing number of available active sites. However, above a certain threshold, the number of accessible adsorption sites exceeds by far the adsorbate amount and the removal efficiency remains constant.[218]

In order to individually study the effect of the adsorbent dosage on the Cu^{2+} ions removal efficiency, other experimental factors, such as solution pH, time of contact and initial concentration of copper ions, were fixed. The removal efficiencies obtained for each material are shown in Figure 5.5 and summarized in Table 5.3.

At first glance, the variation of the adsorbent dosage seems to have a significant influence on the removal efficiencies obtained for MIL-88B(Fe), MIL-100(Fe) and ZIF-DPC, while for MIL-53(Fe) the increase of the adsorbent dosage did not result in considerable changes. As the adsorbent dosage was raised, both MIL-100(Fe) and ZIF-DPC revealed a gradual increase on their adsorption performance, achieving similar maximum Cu^{2+} ion uptake for 1.00 g/L of adsorbent. On the other hand, MIL-88B(Fe) presented low removal efficiencies for both 0.25 g/L and 0.50 g/L adsorbent dosages, although for 1.00 g/L, a very significant increase of removal efficiency could be observed, even surpassing the previous materials

Moreover, MIL-53(Fe) revealed low removal efficiencies and almost no variation along the adsorbent dosages tested. This outcome could probably mean that the number of available adsorption sites in MIL-53(Fe) is much lower than the amount of copper ions in solution, thus resulting in a readily saturation of the active sites by only a small amount of copper ions, while the majority remained in solution.

From the gathered results, we concluded that the adsorbent dosage of 1.00 g/L was the one that reflected the most promising adsorption efficiencies for all materials, and was, therefore selected to be used in further adsorption experiments.

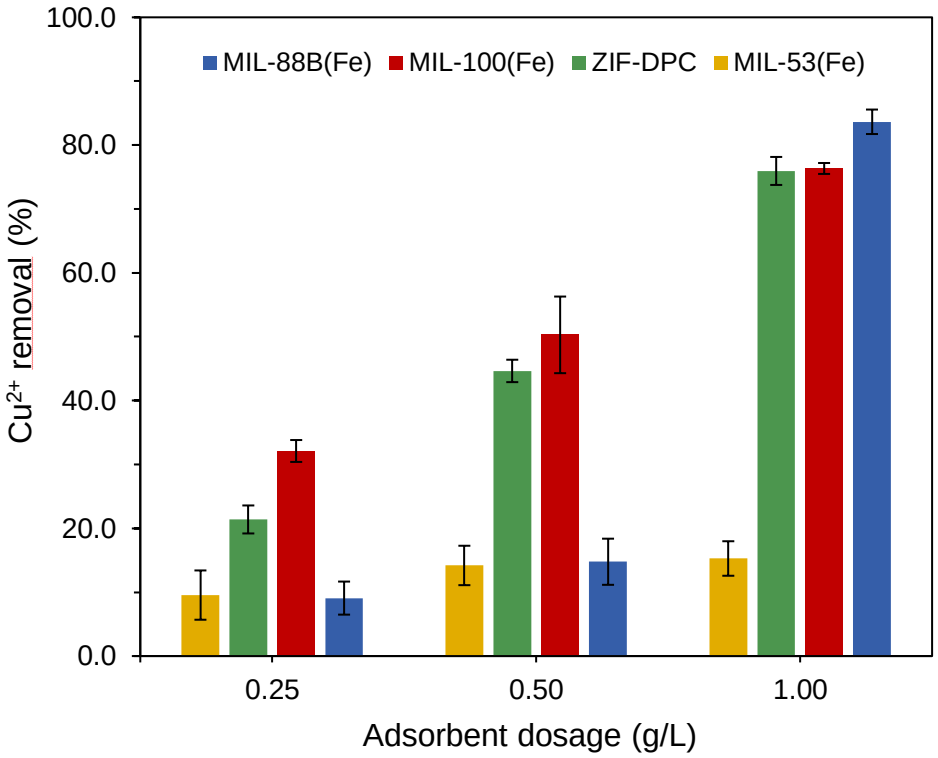

Figure 5.5. Effect of the adsorbent dosage on the removal efficiency of Cu^{2+} for different adsorbents, using 10.0 mg/L of initial concentration of Cu^{2+} at pH 5.50 (average values, n = 2).

Table 5.3. Summary of the removal efficiencies of Cu^{2+} ions obtained for each material at different adsorbent dosages (average value ± standard deviation, n = 2).

Adsorbent Dosage (g/L)	**Removal of Cu^{2+} (%)**			
	MIL-88B(Fe)	MIL-100(Fe)	ZIF-DPC	MIL-53(Fe)
0.25	9 ± 3	32 ± 2	21 ± 2	10 ± 4
0.50	15 ± 4	50 ± 6	45 ± 2	14 ± 3
1.00	84 ± 2	76 ± 1	76 ± 2	15 ± 3

5.2.2. Effect of pH

The solution pH is one of the main factors affecting the adsorption of heavy metal ions. It not only influences the chemical speciation of the metal ions, but also the surface charge of the adsorbent, given it has acidic or basic moieties, as previously discussed in section 5.1.1.

Usually, metal ions are completely soluble under strong acidic conditions, however, as the pH increases, they tend to react with the OH^- ions in solution and precipitate as metal hydroxides, thus impairing the adsorption process. In order to avoid the formation of these chemical species, the pH range must be judiciously selected taking into account their solubility product constants. For instance, copper is present in the Cu^{2+} form as the dominant species at pH values below 6, while above this threshold the formation of $Cu(OH)_2$ occurs.[48] Keeping this phenomenon in mind, the study of the influence of pH in the adsorption process was performed under acidic conditions, from 3.50 up to 5.50 to avoid significant interferences of the metal hydroxide precipitation. Moreover, other parameters that could also affect the adsorption process, such as contact time, initial concentration of copper ions and adsorbent dosage, were maintained constant throughout the experiments.

The removal efficiencies obtained for each material are displayed in Figure 5.6 and summarized in Table 5.4. One can state that for all adsorbents, the increase of pH favoured the uptake of copper ions from the solution. This result could be mainly due to the fact that, under strong acidic conditions, there is a significant concentration of protons (H^+) in solution, which can compete with the copper cations for the active sites of the adsorbents.[59] Thus, given that, with the increase of pH, the concentration of H^+ decreases, an overall increase in the uptake of the metal cations is attained. Besides this, based on the obtained pH_{ZPC} values, at pH 3.50, all the materials present positively charged surfaces, except MIL-88B(Fe). As a consequence of the surface of MIL-88B(Fe) being negatively charged at this pH, its removal efficiency is lower than in the other materials, which could suggest that it is establishing strong electrostatic interactions with H^+ rather than with the copper ions, further confirming the previous statement.

As the pH increases to 4.50, the surface charges of MIL-100(Fe) and MIL-53(Fe) turn negative and their removal efficiencies increase in comparison to the ones observed at pH 3.50, but there is still a considerable influence of the free H^+ ions competing with the Cu^{2+} ions for the active sites. When the pH of the solution reaches 5.50, there was a drastic increase on removal efficiencies obtained for MIL-100(Fe) and MIL-88B(Fe), suggesting that the influence of the H^+ ions decreased considerably, and thus allowing a greater copper uptake. This could have resulted due to stronger electrostatic interactions between the Cu^{2+} and the negatively charged surfaces of MIL-88B(Fe) and MIL-100(Fe). On the other hand, the removal efficiencies associated to MIL-53(Fe) remained low, further suggesting the lack of available adsorption sites for copper adsorption.

Interestingly, even though ZIF-DPC presented a positively charged surface throughout the studied pH range, it revealed removal efficiencies close to those observed

for the other materials, which had negatively charged surfaces. This may suggest that the main mechanism by which the copper uptake occurs may not rely on electrostatic interactions.

The gathered results indicate that the copper ions uptake was enhanced at a solution pH of 5.50, making it the selected pH for the further adsorption experiments.

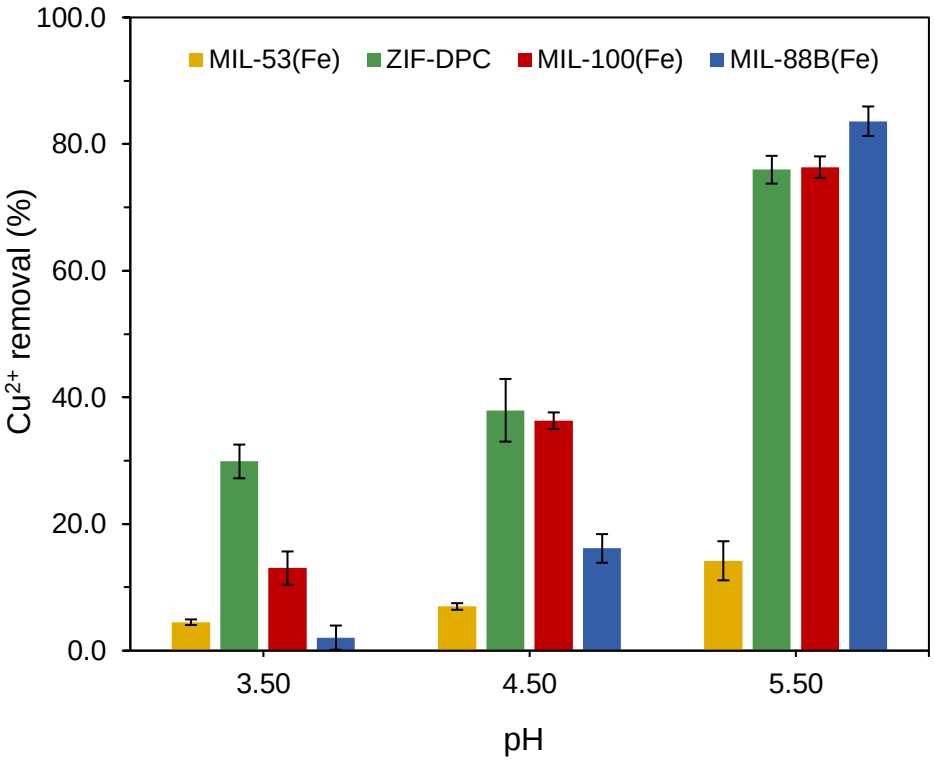

Figure 5.6. Effect of the solution pH on the removal efficiency of Cu^{2+} ions for different pH values, using 10.0 mg/L of initial concentration of Cu^{2+} and 1.00 g/L of adsorbent (average values, n = 2).

Table 5.4. Summary of the removal efficiencies of Cu^{2+} ions obtained for each material at different pH values (average value ± standard deviation, n = 2).

pH	**Removal of Cu^{2+} (%)**			
	MIL-88B(Fe)	MIL-100(Fe)	ZIF-DPC	MIL-53(Fe)
3.50	2 ± 2	13 ± 3	30 ± 3	4 ± 1
4.50	16 ± 2	36 ± 1	38 ± 5	7 ± 1
5.50	84 ± 2	76 ± 2	76 ± 2	14 ± 3

5.2.3. Adsorption kinetics

The kinetics of an adsorption process assumes an important role in the selection and design of the best operation conditions for a given adsorbent/adsorbate system. Adsorption is a multistep mass transfer process that can be roughly divided into 3 stages. The first step is known as external diffusion, which consists in the transference of the adsorbate from the bulk solution to the external surface of the adsorbent. The difference between the adsorbate concentration in the two phases is the main driving force for this step to occur. The second step is the internal diffusion, which describes the entrance of the adsorbate into the pores of the adsorbent and, finally, the third step concerns the adsorption of the adsorbate in the active sites of the adsorbent.[44, 219]

Since the rate at which the overall adsorption process occurs is defined by the slowest step, kinetic studies can provide valuable insights not only about the contact time required to the process to reach equilibrium, but also regarding the rate-limiting steps of the process. For that reason, mathematical models have been developed to describe the kinetics of the adsorption processes.[115, 219]

In this study, we applied two mathematical models to fit the experimental data, the PFO and PSO models, which were previously discussed in section 2.4.4. In general, PFO model fits better adsorption kinetics in which the rate-limiting step is related to the availability of active adsorption sites in the adsorbent for physical interactions. On the other hand, PSO model presents better fittings for adsorption kinetics in which the adsorption rate is dependent of the presence of energetically heterogeneous sites on the adsorbent, usually associated to a chemisorption process. Nevertheless, one cannot accurately deduce the mechanisms by which the adsorption occurs only through kinetic modelling.[48, 115, 219-220]

The best-fitted model was chosen based on the values of the determination coefficient (R^2) and the standard error of the regression (SE). Moreover, when the difference between these values was not evident, an F-test was conducted, according to the equations 15 and 16, to analyse if there were any statistically relevant differences between the two models or not.

$$F = \frac{s_A^2}{s_B^2} \; or \; \frac{s_B^2}{s_A^2} \geq 1 \tag{15}$$

where s_A^2 and s_B^2 are the variances of the model A and B, respectively. Each one was calculated by the following expression:

$$s^2 = \frac{\sum_{i=1}^{N}(q_{exp} - q_{cal})^2}{N - w} \tag{16}$$

where q_{exp} is the experimental value of q, q_{cal} is the predicted value according to each model, N is the number of points and w is the number of estimated parameters in the model.

Moreover, besides the influence of the contact time and adsorbate-adsorbent interactions, adsorption kinetics can also be affected by other parameters, such as solution pH, initial concentration of the adsorbate and adsorbent dose.[61] Therefore, they were maintained constant throughout the experimental procedures, as pH 5.50, 10.0 mg/L of initial concentration of copper ions and 1.00 g/L of adsorbent dose, while the contact time was changed. The studies regarding adsorption kinetics were performed for MIL-88B(Fe), MIL-100(Fe) and ZIF-DPC and will be discussed below.

5.2.3.1. MIL-88B(Fe)

Figure 5.7 displays the experimental data obtained for the adsorption kinetics of MIL-88B(Fe) together with the respective curves of the PFO and PSO fitting models.

It can be seen that the adsorption rate quickly increased within 60 min of contact time, owing to the large number of available adsorption sites at the initial stage of the adsorption process. Thereafter, the availability of adsorption sites decreases, leading to a decrease of the adsorption rate and a plateau is observed, indicating that the equilibrium was reached. The amount of copper ions adsorbed at equilibrium, $q_{e,exp}$, was calculated as the arithmetic mean of all experimental points in the plateau, resulting in 8.4 ± 0.2 mg/g, which correspond to an average removal efficiency of 88 ± 2%.

Table 5.5 presents the estimated parameters determined from both modelled curves, and the corresponding R^2 and SE values. Based on these values, the PFO model seems to better fit the experimental data than the PSO model, due to its higher value of R^2 and lower value of SE.

Regardless, the variances provided by the two model regressions were statistically compared through F-test at a 95% confidence level which indicated that there were no significant statistical differences between them. This suggests that both models can describe the adsorption kinetics of Cu^{2+}. The $q_{e,cal}$ values predicted by PFO (8.44 ± 0.03 mg/g) and PSO (8.9 ± 0.1 mg/g) were relatively close to the experimental value. These results suggest that both chemical and physical interactions between MIL-88B(Fe) and Cu^{2+} ions might be involved in the adsorption process as rate-controlling steps.[221]

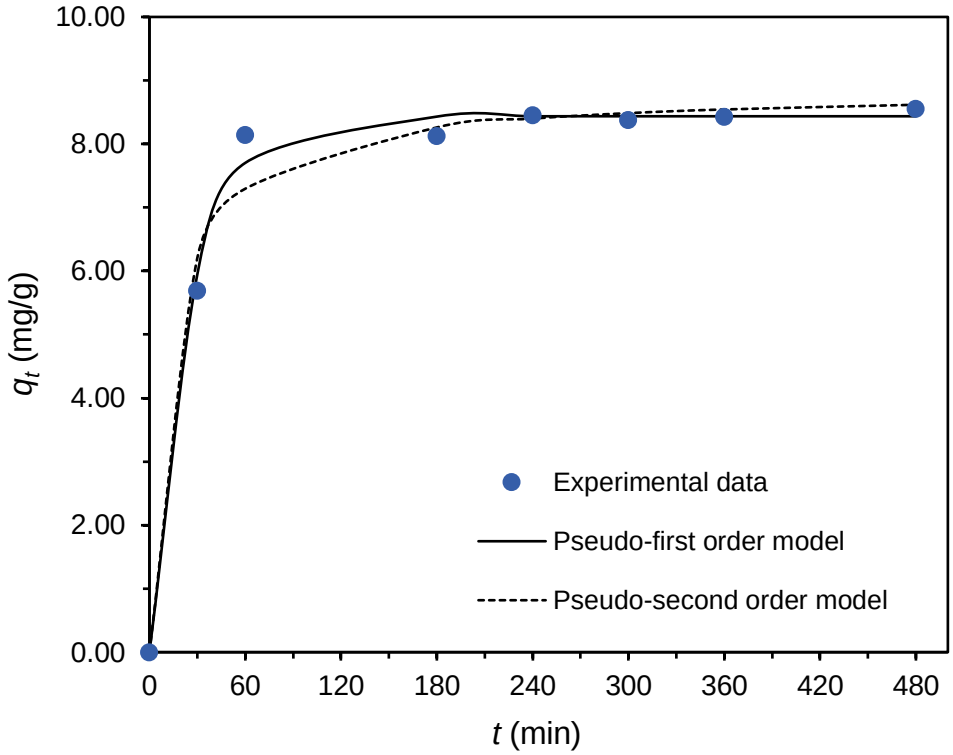

Figure 5.7. Effect of contact time on the adsorption of Cu^{2+} by MIL-88B(Fe) and the corresponding PFO and PSO modelling (average values, n = 2).

Table 5.5. Kinetic parameters of PFO and PSO modelling for the adsorption of Cu^{2+} by MIL-88B(Fe) (average value ± standard deviation, n = 2).

Pseudo-first order model			
$k_1 \times 10^2$ (min^{-1})	$q_{e,cal}$ (mg/g)	R^2	SE (mg/g)
4.1 ± 0.3	8.44 ± 0.03	0.994	0.248
Pseudo-second order model			
$k_2 \times 10^3$ (g/(mg.min))	$q_{e,cal}$ (mg/g)	R^2	SE (mg/g)
9 ± 1	8.9 ± 0.1	0.983	0.415

5.2.3.2. MIL-100(Fe)

The experimental data obtained for the adsorption kinetics of MIL-100(Fe) and the respective modelled curves of PFO and PSO are presented in Figure 5.8.

The kinetic curve of MIL-100(Fe) showed a fast adsorption rate in the first 30 min of contact time, due to the large availability of active sites at the beginning of the adsorption process. Then, the adsorption rate gradually slowed down up to 180 min, owing to the

reduced number of accessible/available adsorption sites as the concentration of adsorbed Cu^{2+} increases. From this point onwards, a plateau is observed, implying that the adsorption equilibrium has been reached after 180 min of contact time. The experimental q_e value was 8.1 ± 0.1 mg/g, which corresponds to an average removal efficiency of 83 ± 1%.

Table 5.6 displays the predicted parameters obtained from both PFO and PSO modelling curves as well as the respective R^2 and SE values. The R^2 and SE values for the PFO were 0.995 and 0.214, while for PSO were 0.998 and 0.131, respectively. Since both models presented high R^2 values and low SE values, it is not evident which model better fits the adsorption kinetic data. Therefore, in order to further analyse if there were any differences between the variances provided by the two model regressions, an F-test at a 95% confidence level was conducted. The F-test revealed no significant differences between them, indicating that both models can be used to describe the experimental data of the adsorption kinetics of Cu^{2+}. The $q_{e,cal}$ values estimated by PFO (8.0 ± 0.1 mg/g) and PSO (8.50 ± 0.04 mg/g) were in agreement with the experimental q_e value.

Similarly to MIL-88B(Fe), the obtained results for the adsorption kinetics of MIL-100(Fe) suggest that the controlling steps of the adsorption rate of Cu^{2+} could be related with chemical and physical adsorbate-adsorbent interactions.

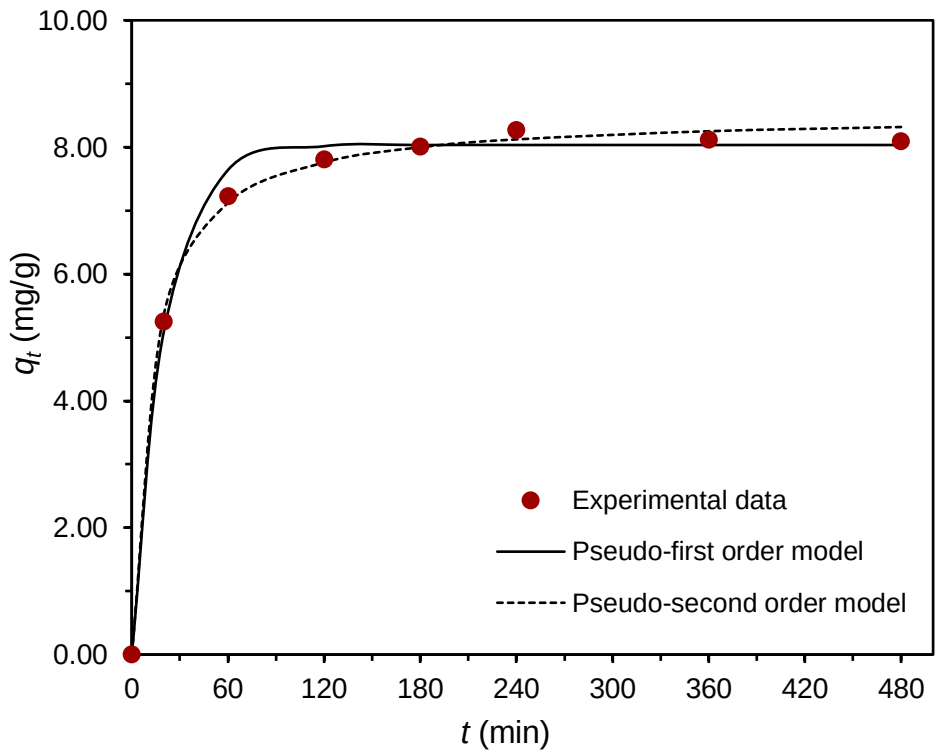

Figure 5.8. Effect of contact time on the adsorption of Cu^{2+} by MIL-100(Fe) and the corresponding PFO and PSO modelling (average values, n = 2).

Table 5.6. Kinetic parameters of PFO and PSO modelling for the adsorption of Cu^{2+} by MIL-100(Fe) (average value ± standard deviation, n = 2).

Pseudo-first order model			
$k_1 \times 10^2$ **(min^{-1})**	$q_{e,cal}$ **(mg/g)**	**R^2**	**SE (mg/g)**
4.9 ± 0.8	8.0 ± 0.1	0.995	0.214
Pseudo-second order model			
$k_2 \times 10^3$ **(g/(mg.min))**	$q_{e,cal}$ **(mg/g)**	**R^2**	**SE (mg/g)**
10 ± 2	8.50 ± 0.04	0.998	0.131

5.2.3.3. ZIF-DPC

The effect of contact time in the adsorption of Cu^{2+} ions by ZIF-DPC was evaluated. The obtained experimental data reveal the adsorption kinetic process whose results are shown in Figure 5.9, together with the respective curves of the PFO and PSO models. It can be observed that the adsorption process of Cu^{2+} by ZIF-DPC required considerably more time to reach the equilibrium compared to the other materials, which consequently lead to a slower adsorption rate.

The adsorption kinetic curve showed a gradual increase of the amount of Cu^{2+} adsorbed up to 360 min of contact time, and after that, the adsorption equilibrium was reached. This behaviour may have resulted from electrostatic repulsive interactions between the copper cations and the positively charged surface of ZIF-DPC. Thus, the exchange of Cu^{2+} from the bulk solution to the adsorbent was slowed down, shifting the adsorption equilibrium towards longer contact times. The experimental q_e value was 8.8 ± 0.1 mg/g, which correspond to an average removal efficiency of 93 ± 3%. Such values are surprisingly higher than the MIL-88B(Fe) and MIL-100(Fe), considering the obtained textural properties ($A_{s,BET}$; V_p) and its positively charged surface.

The parameters obtained through PFO and PSO modelling, along with the respective R^2 and SE values are presented in Table 5.7. As it can be observed, high R^2 and low SE values were obtained for the PFO and PSO models, suggesting that both models could be used to describe the adsorption kinetics. Hence, to confirm this statement, the F-test at a 95% confidence level was performed to evaluate any differences between the variances provided by both model fittings. From the gathered results of F-test we concluded that there were no significant differences between them, indicating that the fitting of both models cannot be differentiated statistically. Nonetheless, the $q_{e,cal}$ value

predicted by PFO modelling (8.7 ± 0.1 mg/g) was closer to the experimental q_e value than the one estimated by the PSO modelling (10.8 ± 0.1 mg/g).

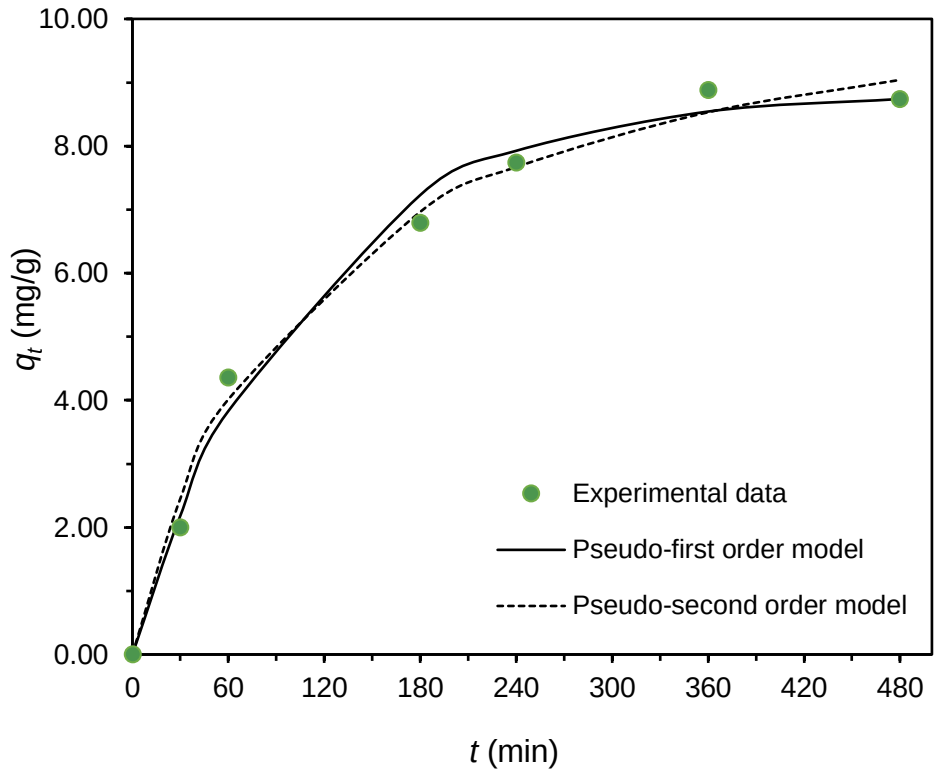

Figure 5.9. Effect of contact time on the adsorption of Cu^{2+} by ZIF-DPC and the corresponding PFO and PSO modelling (average values, n = 2).

Table 5.7. Kinetic parameters of PFO and PSO modelling for the adsorption of Cu^{2+} by ZIF-DPC (average value ± standard deviation, n = 2).

Pseudo-first order model			
$k_1 \times 10^2$ (min^{-1})	$q_{e,cal}$ (mg/g)	R^2	SE (mg/g)
1.0 ± 0.1	8.7 ± 0.1	0.990	0.373
Pseudo-second order model			
$k_2 \times 10^3$ (g/(mg.min))	$q_{e,cal}$ (mg/g)	R^2	SE (mg/g)
0.9 ± 0.1	10.8 ± 0.1	0.992	0.348

Table 5.8 summarizes the obtained values of $q_{e,exp}$ and the corresponding adsorption efficiencies at the end of the kinetic study for each adsorbent material.

Table 5.8. Summary of $q_{e,exp}$ and removal efficiency values of each adsorbent at an initial concentration of Cu^{2+} of 10.0 mg/L (average values ± standard deviation, n = 2).

Material	$q_{e,exp}$ (mg/g)	Removal efficiency (%)
MIL-88(Fe)	8.4 ± 0.2	88 ± 2
MIL-100(Fe)	8.1 ± 0.1	83 ± 1
ZIF-DPC	8.8 ± 0.1	93 ± 3

5.2.4. Adsorption equilibrium

The study of adsorption equilibrium is essential in the design of adsorption systems since it can provide useful information about the interactions between the adsorbent and the adsorbate. In general, the adsorption capacity on a given adsorbent increases rapidly with increasing concentration of initial adsorbate, owing to the high driving force of the mass transfer, resultant from the elevated concentration gradient. However, above a certain threshold, the adsorption capacity slowly reaches a plateau due to the saturation of the adsorption sites on the adsorbent. This phenomenon indicates that the adsorption equilibrium was attained and the amount of adsorbate being adsorbed onto the adsorbent is equal to the amount being desorbed, suggesting that the adsorbent achieved its maximum adsorption capacity towards a specific adsorbate.[222-223]

The behaviour of an adsorption process in equilibrium can be described by several isotherm models, that can provide valuable information about the performance of the adsorbents. In this study, the experimental data was compared to the Langmuir and Freundlich isotherm models. The mathematical description and basic theoretical assumptions of each model were discussed in section 2.4.5. As in the kinetic studies, evaluation of the best-fitted model was attained by comparing the R^2 and SE associated to each model. Additionally, when the difference between these values was not so notorious, an F-test was also performed to further analyse if there were any significant differences between the variances of both models.

Furthermore, to minimize the influence of other factors besides the difference between the initial concentration of Cu^{2+} on the adsorption process, the solution pH, adsorbent dosage and contact time were maintained throughout the experiments, at 5.50, 1.00 g/L and 6 h, respectively. The adsorption equilibrium studies were performed for MIL-88B(Fe), MIL-100(Fe) and ZIF-DPC.

5.2.4.1. MIL-88B(Fe)

The equilibrium studies for MIL-88B(Fe) were performed by varying the initial concentrations of Cu^{2+} from 10.0 to 800 mg/L to ensure that the equilibrium was achieved. Figure 5.10 presents the obtained experimental data along with the Langmuir and Freundlich isotherm modelling curves. It can be seen that the adsorption capacity of MIL-88B(Fe) at equilibrium increased significantly with the increase of initial Cu^{2+} concentration until 300 mg/g, probably due to the strong affinity of MIL-88B(Fe) towards Cu^{2+} ions. Thereafter, a plateau is observed around 350 mg/g, indicating that the active sites were completely occupied.

Moving on to the isotherm fitting models, it can be readily noted that the Langmuir model describes the experimental data considerably better that the Freundlich model. In Table 5.9 are shown the parameters obtained from each model along with the respective R^2 and SE values. The Langmuir isotherm fitting presented considerably higher R^2 and lower SE values than the Freundlich modelling, confirming that the first model is more suitable to describe the experimental results. The maximum adsorption capacity predicted by the Langmuir modelling was 353 ± 1 mg/g, which is in agreement with the experimental observations. Moreover, the R_L values calculated for all initial Cu^{2+} concentrations tested, were between 0.0981 and 0.0027, indicating that the overall adsorption process was favourable.

Based on the theoretical principles of the Langmuir model, these results suggest that the surface of the MOF presents well-defined and homogeneous active sites with equal adsorption affinities, further implying a monolayer-type adsorption of Cu^{2+}. This behaviour is often reported in the literature regarding heavy metal ions adsorption studies with other MOFs, as a result of their crystalline structure with ordered porosity.[224-226]

Interestingly, MIL-88B(Fe) revealed great adsorption capacity in spite of not having high apparent accessible specific surface area. We could hypothesize that the mechanism by which Cu^{2+} ions are adsorbed might be related to the swelling breathing behaviour characteristic of MIL-88B(Fe) framework. Given that, when exposed to polar solvents, such as water, tends to expand its pore volume, which could further allow a greater uptake of Cu^{2+}, leading to higher maximum adsorption capacities.[132]

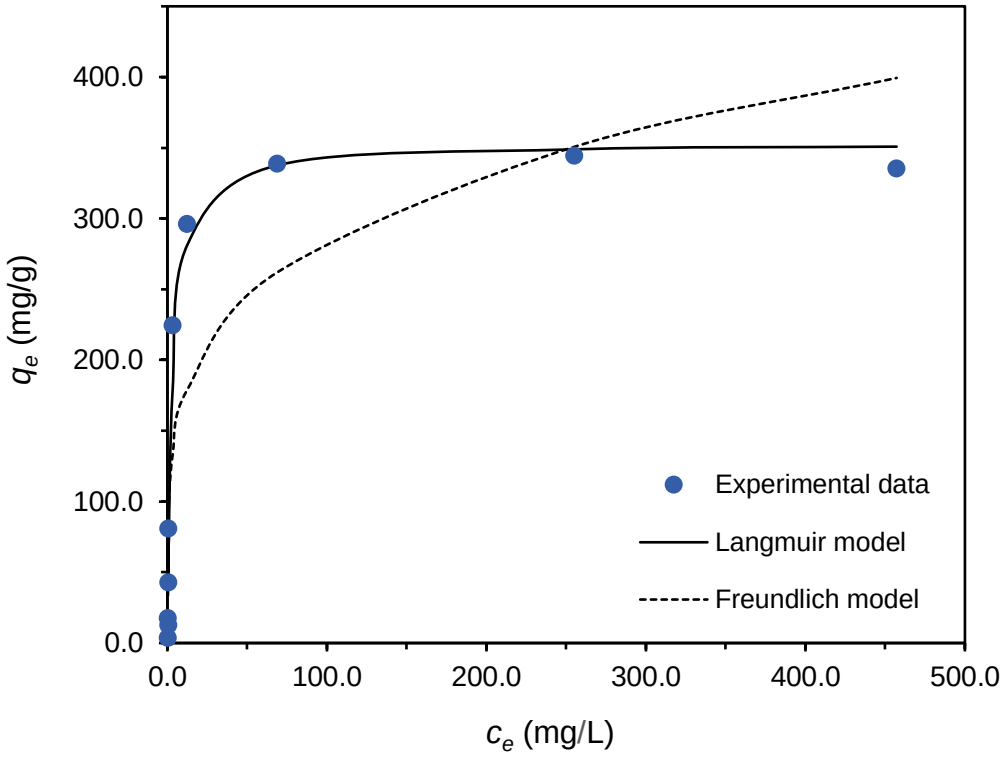

Figure 5.10. Experimental and theoretical equilibrium isotherms of Cu^{2+} adsorption on MIL-88B(Fe) (average values, n = 2).

Table 5.9. Langmuir and Freundlich isotherm parameters of Cu^{2+} adsorption on MIL-88B(Fe) (average value ± standard deviation, n = 2).

Langmuir model			
q_{max} **(mg/g)**	K_L **(L/mg)**	R^2	**SE (mg/g)**
353 ± 1	0.31 ± 0.02	0.991	31.0
Freundlich model			
n	K_F **[((mg/g).(L/mg))$^{1/n}$]**	R^2	**SE (mg/g)**
4.8 ± 0.5	109 ± 12	0.756	80.6

5.2.4.2. MIL-100(Fe)

To study the adsorption maximum capacity of MIL-100(Fe), several solutions were prepared with initial concentrations of Cu^{2+} ranging from 10.0 to 200 mg/L. The obtained experimental data and corresponding Langmuir and Freundlich isotherm modelling curves are shown in Figure 5.11. The equilibrium adsorption capacity of MIL-100(Fe) went through a gradual increase as the initial concentration of Cu^{2+} increased until reaching a plateau at 34.3 mg/g, implying the saturation of the active sites.

The parameters obtained from the Langmuir and Freundlich models along with the corresponding R^2 and SE values are presented in Table 5.10. According to the R^2 and SE values, both models seem to fit well the experimental data. Therefore, an F-test was conducted to evaluate any differences between the variances of both models. The F-value calculated by the equation 15 was below the critical F-value for a confidence level of 95%, indicating that are no significant differences between the predictions of both models. Thus, the experimental equilibrium isotherm of MIL-100(Fe) can be described by both isotherm models.

Despite the fact that these models are based upon different theoretical assumptions, it has been reported that when the experimental data present good fitting for both models, could indicate that there is more than one type of adsorption mechanism. Taking into consideration the structural and chemical features of MIL-100(Fe) with different pore size, we could hypothesize that the Cu^{2+} ions were firstly adsorbed onto the surface of the MOF creating a monolayer and only then, diffused into the pores in a unevenly manner.[227-228]

According to the predicted parameters by the Langmuir modelling, the q_{max} was 36 ± 5 mg/g and the calculated R_L values were within 0.618 and 0.075 for all initial concentrations of Cu^{2+} tested, implying that the adsorption process was favourable. It is interesting to note that MIL-100(Fe) revealed an q_{max} almost ten times lower than the one obtained for MIL-88B(Fe). The n value predicted by the Freundlich model is above 1, further confirming that the adsorption of Cu^{2+} was promoted.

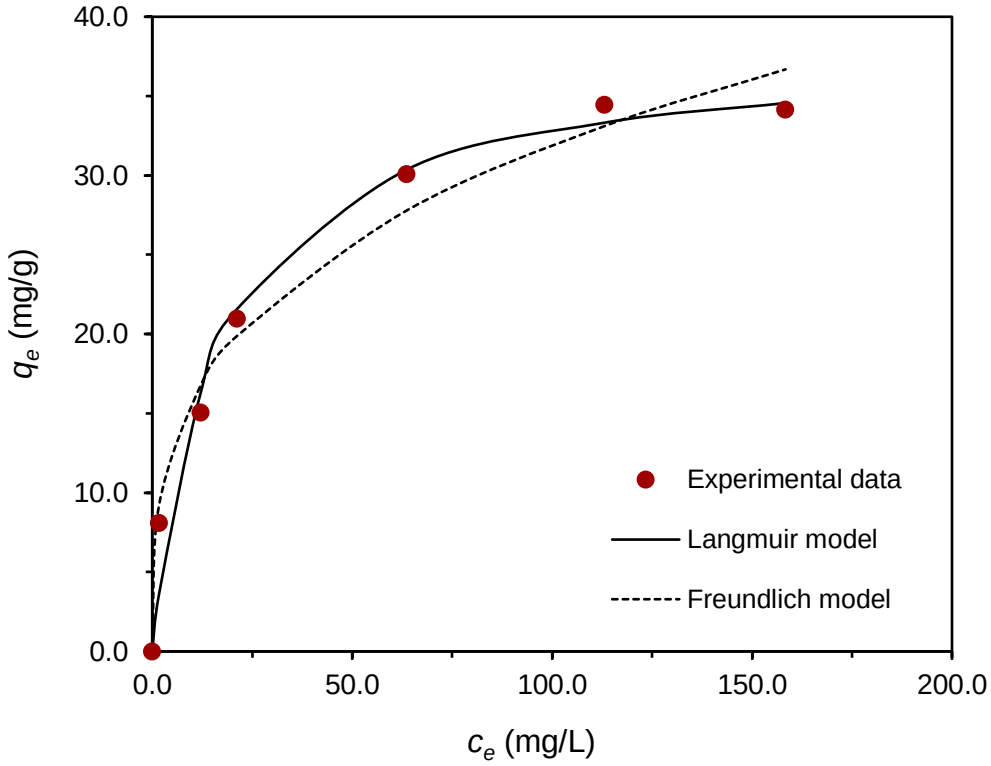

Figure 5.11. Experimental and theoretical equilibrium isotherms of Cu^{2+} adsorption on MIL-100(Fe) (average values, n = 2).

Table 5.10. Langmuir and Freundlich isotherm parameters of Cu^{2+} adsorption on MIL-100(Fe) (average value ± standard deviation, n = 2).

Langmuir model			
q_{max} **(mg/g)**	K_L **(L/mg)**	R^2	**SE (mg/g)**
36 ± 5	0.26 ± 0.03	0.983	2.17
Freundlich model			
n	K_F **[((mg/g).(L/mg))$^{1/n}$]**	R^2	**SE (mg/g)**
5 ± 2	12 ± 6	0.983	1.94

5.2.4.3. ZIF-DPC

In order to investigate the adsorption capacity of ZIF-DPC under equilibrium conditions, solutions with different concentrations of Cu^{2+}, ranging from 5.00 to 200 mg/L were prepared. The experimental equilibrium isotherm and the respective Langmuir and Freundlich isotherm modelling curves are displayed in Figure 5.12. It can be observed that the adsorption capacity of ZIF-DPC increased swiftly as the initial concentration of

Cu^{2+} ions was raised until 15.5 mg/g, owing to the great availability of active sites. Then, the increase of adsorption capacity gradually slowed down, reaching a plateau at 19.7 mg/g, indicating that the accessible active sites were all occupied, and the maximum capacity of the material was achieved.

Focusing on the isotherm modelling results, in Table 5.11 it is summarized the obtained parameters concerning each model accompanied by the respective R^2 and SE values. The Langmuir isotherm seems to have a better correlation with the experimental data than the Freundlich model, due to its higher R^2 and lower SE values. However, due to the fact that both models presented reasonable correlations ($R^2 > 0.9$), an F-test at a 95% confidence level was then performed to examine any statistically relevant differences. The calculated F-value was above the critical F-value, confirming that the Langmuir model predicted the experimental data significantly better that the Freundlich model. Regarding the estimated parameters by the Langmuir model, the q_{max} was 19.4 ± 0.1 mg/g and the R_L values determined for all initial concentrations of Cu^{2+} tested were between 0.143 and 0.035, indicating that the adsorption process was favourable.

The gathered results suggest that the active sites are homogeneously distributed over the ZIF-DPC surface and have equal adsorption performance, leading to a monolayer-type adsorption of the Cu^{2+} ions. However, ZIF-DPC revealed the lowest q_{max} in comparison to the other materials.

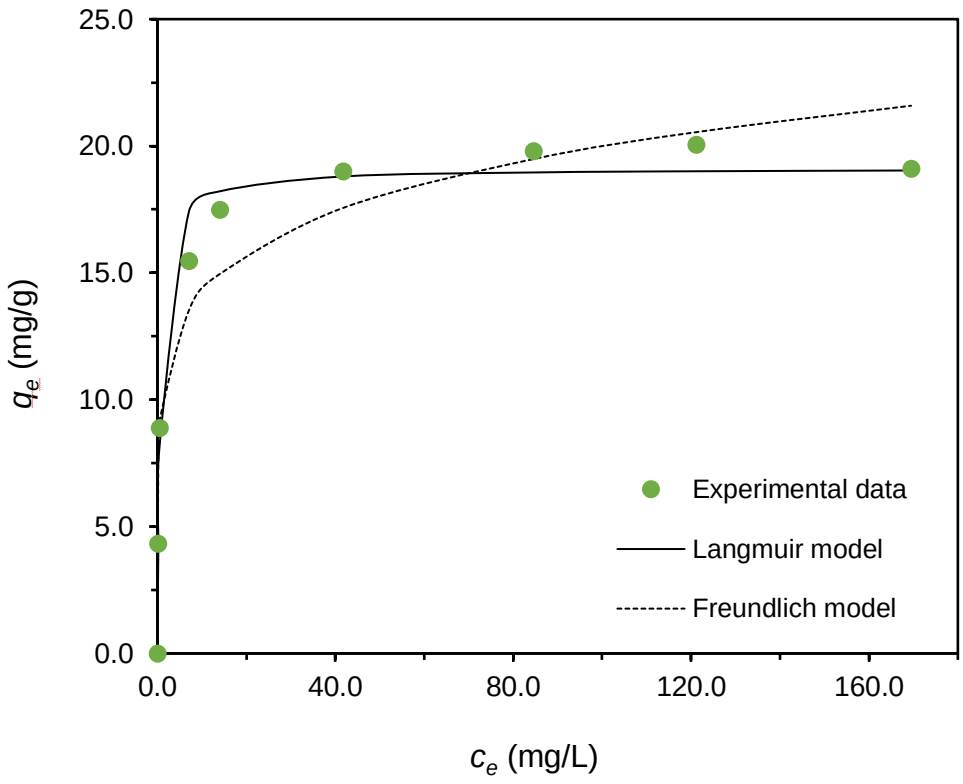

Figure 5.12. Experimental and theoretical equilibrium isotherms of Cu^{2+} adsorption on ZIF-DPC (average values, n = 2).

Table 5.11. Langmuir and Freundlich isotherm parameters of Cu^{2+} adsorption on ZIF-DPC (average value ± standard deviation, n = 2)

Langmuir model			
q_{max} **(mg/g)**	K_L **(L/mg)**	R^2	**SE (mg/g)**
19.4 ± 0.1	1.4 ± 0.1	0.986	1.13
Freundlich model			
n	K_F **[((mg/g).(L/mg))$^{1/n}$]**	R^2	**SE (mg/g)**
6.6 ± 0.2	10.1 ± 0.2	0.930	2.13

5.3. Recycling studies

The ability to recover and reuse adsorbents are important aspects towards sustainable and cost-effective adsorption processes for practical applications. Considering this, recycling experiments were performed using MIL-88B(Fe), since it was the adsorbent material that revealed the most promising Cu^{2+} adsorption efficiencies and the highest q_{max} value. In this study, the first adsorption cycle was performed using 1.00 g/L of adsorbent in the presence of 10.0 mg/L of Cu^{2+} ions at pH 5.50. Thereafter, the adsorbent was recovered and the second cycle experiments were conducted in two different ways, one after the adsorbent regeneration using 0.01 mol/dm^3 of HCl as eluent, while the other was carried out without further desorption treatment. The desorption process with HCl was able to recover 66 ± 2% of the Cu^{2+} ions adsorbed on MIL-88B(Fe).

The resultant adsorption efficiencies at each cycle are displayed in Figure 5.13 and summarized in Table 5.12. It can be seen that the uptake of Cu^{2+} ions slightly decreased from 82 to 76% in the second cycle performed without desorption treatment. This outcome was expected, due to the less availability of unoccupied active sites. Nevertheless, the obtained adsorption efficiency was quite reasonable, given the fact that no desorption treatments were performed, thus confirming the high adsorption capacity of this MOF.

In the second cycle conducted after the desorption process the removal efficiency increased by 10% compared to the first cycle. This could suggest that the HCl treatment may have created defects in the crystalline structure of MIL-88B(Fe), thus introducing more active sites for Cu^{2+} ions to be adsorbed and consequently leading to an increase on the uptake efficiency.

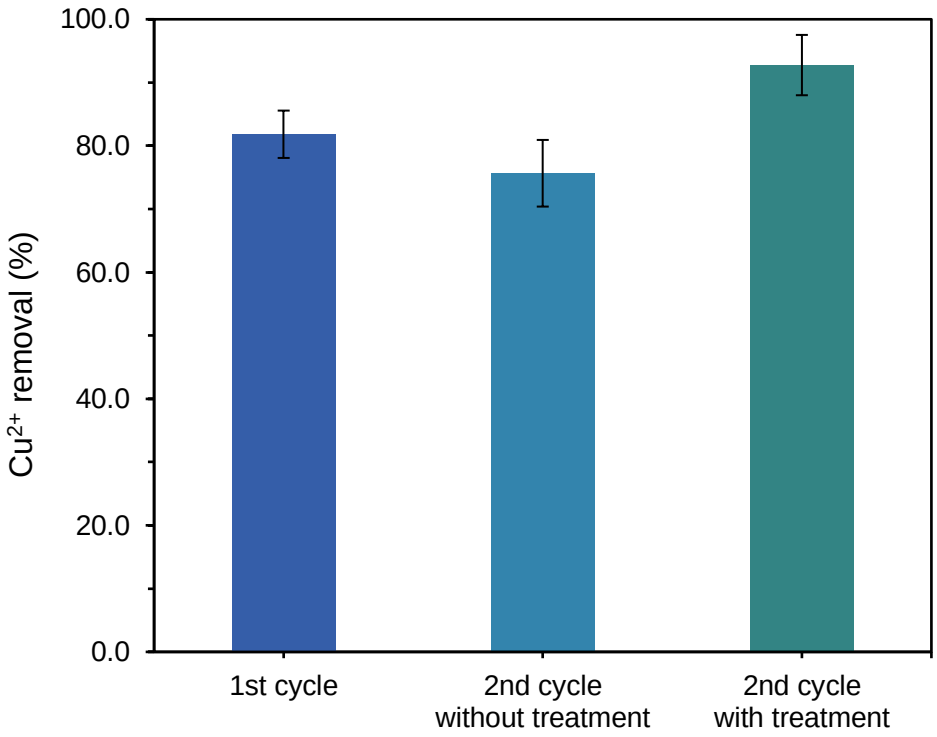

Figure 5.13. Removal efficiencies upon consecutive cycles with and without desorption treatment with HCl (average values, n = 2).

Table 5.12. Summary of the removal efficiencies upon consecutive cycles with and without desorption treatment with HCl (average value ± standard deviation, n = 2).

Cycle	**Removal of Cu^{2+} (%)**
1^{st}	82 ± 4
2^{nd} without treatment	76 ± 5
2^{nd} with treatment	93 ± 5

6. Materials characterization after adsorption studies

After the adsorption studies, the adsorbent materials were characterized by PXRD, FT-IR and SEM/EDS to evaluate their chemical stability throughout the adsorption processes. Moreover, FT-IR technique was also employed to detect any changes on the chemical environment of the functional groups in the presence of copper ions, providing further insights regarding the interactions between the metal ions and the adsorbent structure.

6.1. MIL-88B(Fe)

6.1.1. PXRD

The crystalline structure of MIL-88B(Fe) after the adsorption of Cu^{2+} as well as after the desorption process with HCl was investigated by PXRD and the obtained diffraction patterns were compared to the initial MIL-88B(Fe) pattern (Figure 6.1).

The diffraction pattern of MIL-88B(Fe) after adsorption revealed sharp and intense diffraction peaks, indicating that the material maintained its crystalline nature. Nevertheless, some differences were observed regarding the intensity and position of the diffraction peaks in comparison to the initial PXRD pattern. This phenomenon could be due to the large swelling breathing effect that the MIL-88B(Fe) framework experiences when the pores are filled with guest molecules. The host-guest interactions have the ability to induce large atomic displacements in the framework structure, which even induce changes in its unit cell parameters, and consequently lead to significant changes in the position and intensity of the diffractions peaks.[80, 132]

The desorption process with HCl solution of 0.01 mol/dm^3 seems to have induced a partial collapse of the original framework structure, due to the appearance of a very broad diffraction peak at 2θ of 10.70º.

From the gathered results, we can suggest that MIL-88B(Fe) maintained its crystalline structure throughout the adsorption experiments. This observation allied with its great adsorption performance of Cu^{2+}, suggest that MIL-88(Fe) is a promising adsorbent towards the removal of water contaminants. However, further studies concerning the use of alternative desorption eluents (e.g. EDTA, NaCl) or different concentrations of HCl must be performed, since the desorption process with HCl at 0.01

mol/dm^3 seems to have led to partial degradation or phase change of the framework structure.

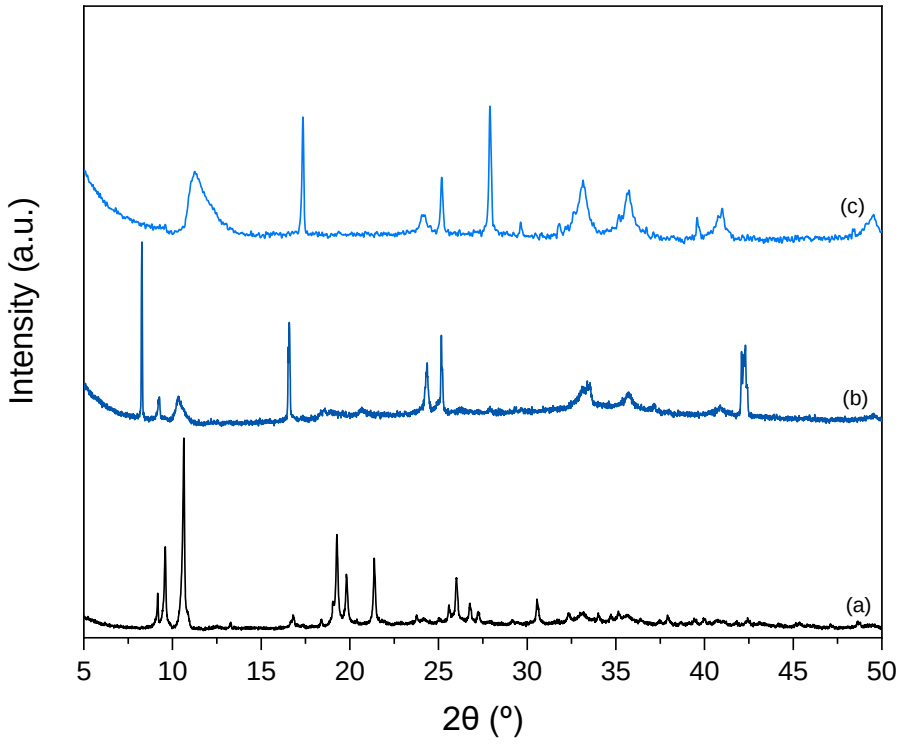

Figure 6.1. PXRD patterns of MIL-88B(Fe) (a) before and (b) after the adsorption of Cu^{2+} and (c) after the desorption process with HCl.

6.1.2. FT-IR

The influence of adsorption and desorption studies in the structural integrity of MIL-88B(Fe) was also investigated by FT-IR, in order to understand the impact of this procedures at a molecular level. The infrared spectra of MIL-88B(Fe) before and after the adsorption and desorption studies, as well as the spectrum of pure terephthalic acid molecules are presented in Figure 6.2.

It can be observed that after the adsorption of Cu^{2+} ions, the material maintained all the characteristic absorption peaks assigned to the vibrational modes of the coordinated terephthalate linkers, confirming that the molecular structure of MIL-88B(Fe) was preserved after being exposed to copper ion solutions. No apparent shifts in the wavenumber values were observed, expect for the vibrational band ascribed to the asymmetric stretching mode of the carboxylate anionic groups, which revealed a minor shift towards higher wavenumbers, from 1602 cm^{-1} to 1610 cm^{-1}, and a drastic intensity decrease. This could suggest that the copper ions might be trapped insight the framework pores, and thus affecting the asymmetric stretching vibrations of the carboxylate groups.

Regarding the spectrum of MIL-88B(Fe) after the desorption process, we can see major shifts in the vibrational bands assigned to the O–C–O asymmetric and symmetric stretching vibrational modes towards lower wavenumber values, from 1602 to 1425 cm^{-1} and from 1392 to 1290 cm^{-1}, respectively. Moreover, the appearance of additional adsorption peaks can also be seen, which the most evident one at 1690 cm^{-1}. Comparing this infrared spectrum with the one of pure terephthalic acid, we can state that these occurrences are mainly due to the presence of non-coordinated ligands, which suggests at least partial structural collapse of the framework after being subjected to the HCl treatment, further confirming the gathered results from PXRD.

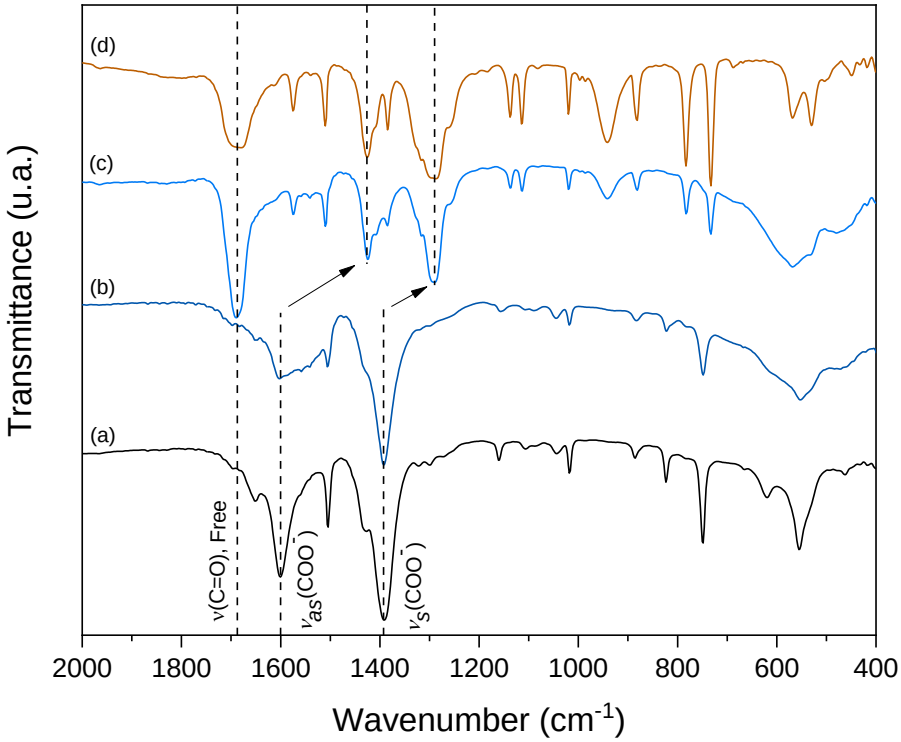

Figure 6.2. FT-IR spectra of MIL-88B(Fe) (a) before adsorption, (b) after adsorption and (c) after HCl desorption treatment; (d) FT-IR spectrum of pure terephthalic acid compound.

6.1.3. SEM/EDS

The SEM micrographs, displayed in Figure 6.3, revealed that after Cu^{2+} adsorption, MIL-88B(Fe) retained its original morphology, as evidenced by the well-defined microrods with hexagonal shape. The particles showed an average length of 1.80 ± 0.30 µm and the average width of 278 ± 45 nm, which seems to be lower than the previously reported values in section 3.3.4. concerning the as-synthetized MOF.

The EDS spectrum shown in Figure 6.4, verified the chemical composition of the MOF, and confirmed the uptake of Cu^{2+} ions by MIL-88B(Fe), owing to the presence of copper element.

The SEM micrographs of MIL-88B(Fe) after the desorption process showed that the morphology of the particles was completely changed in comparison with the starting MOF (Figure 6.5). Instead of hexagonally shaped microrods, small nanostructures could be observed, with an average size of 113 ± 15 nm. This outcome suggests that the framework of MIL-88B(Fe) was indeed destroyed in the presence of HCl. Further confirming the gathered conclusions from PXRD and FT-IR techniques.

The EDS analysis identified the presence of the main chemical elements of the original material (Fe, C and O) and trace amounts of chloride, arising from the HCl solution (Figure 6.6).

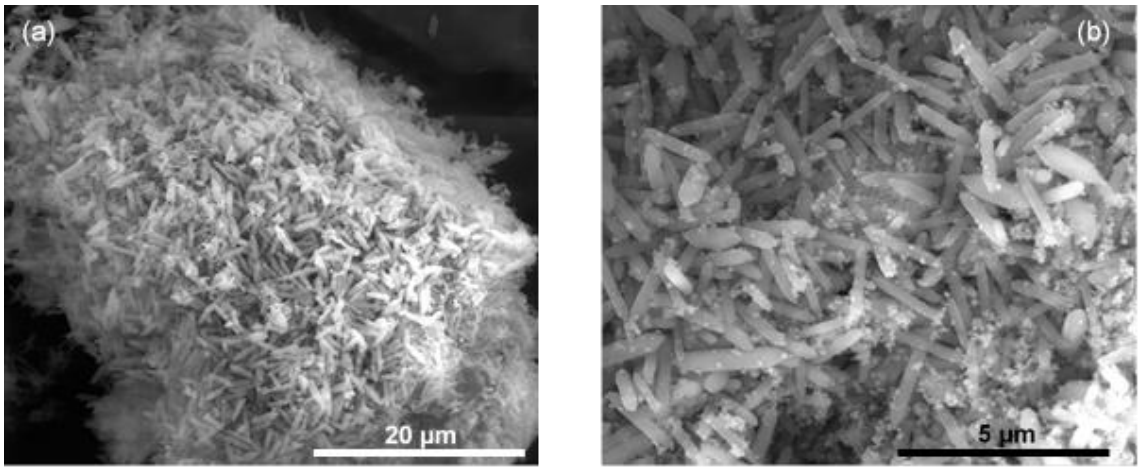

Figure 6.3. SEM micrographs of MIL-88B(Fe) after adsorption studies at different magnifications (a) 5,000x and (b) 20,000x.

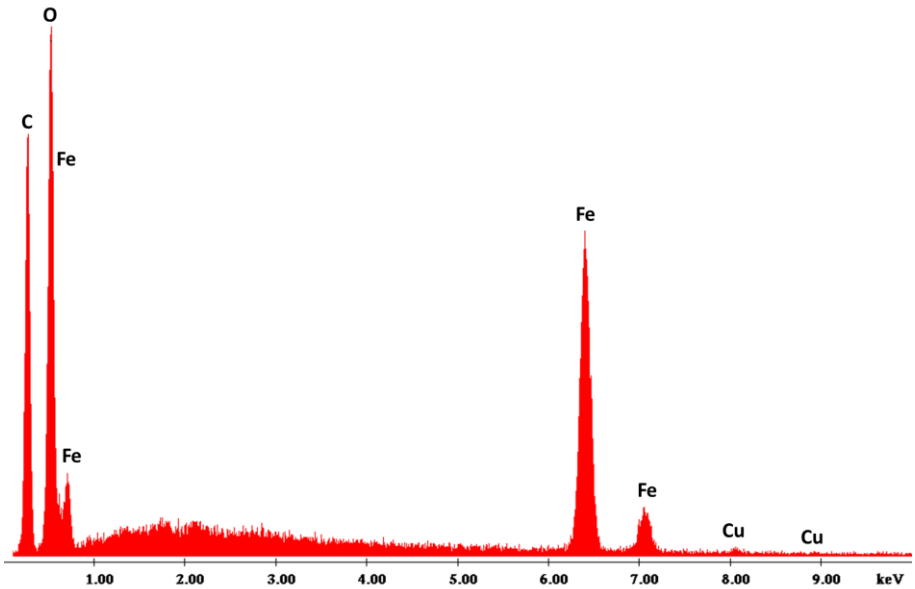

Figure 6.4. EDS spectrum of MIL-88B(Fe) after adsorption of Cu^{2+} ions.

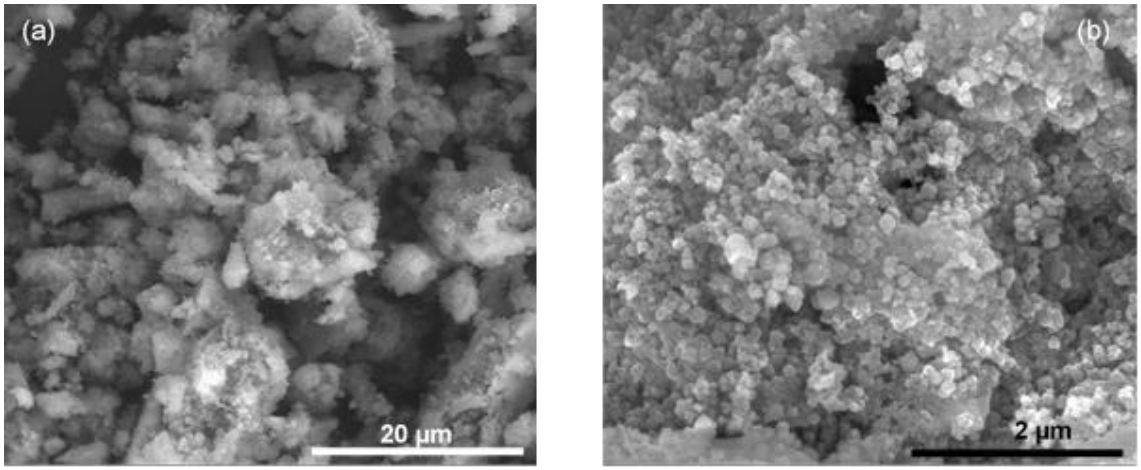

Figure 6.5. SEM micrographs of MIL-88B(Fe) after desorption studies at different magnifications (a) 5,000x and (b) 50,000x.

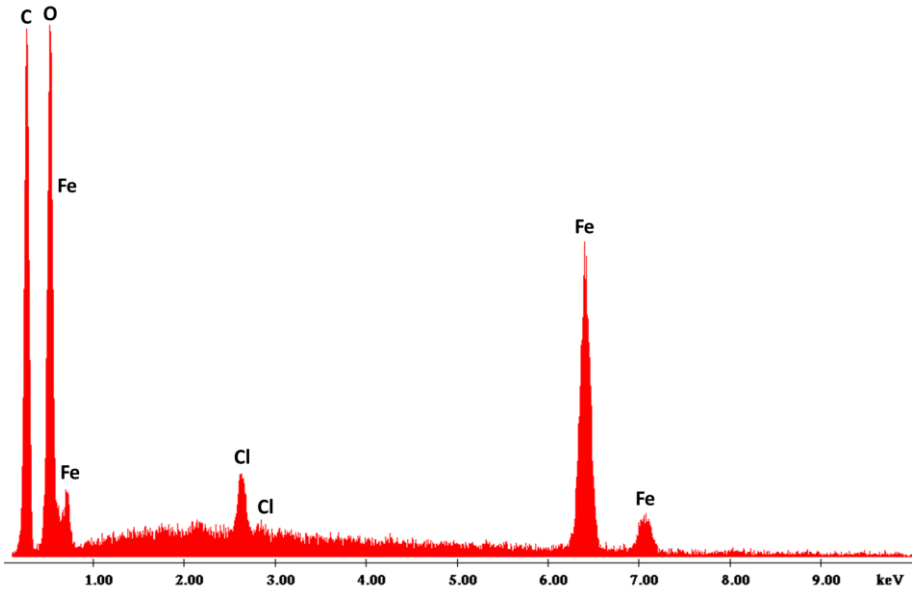

Figure 6.6. EDS spectrum of MIL-88B(Fe) after desorption process with HCl 0.01 mol/dm^3.

6.2. MIL-100(Fe)

6.2.1. PXRD

The chemical stability of MIL-100(Fe) after the adsorption studies, was verified by PXRD. The diffraction patterns of MIL-100(Fe) before and after the adsorption studies are displayed in Figure 6.7. As it can be observed, all the diffraction peaks characteristic of the MIL-100(Fe) crystalline structure were preserved after the adsorption process. Moreover, the appearance of narrow and well-defined peaks indicates that the material

maintained its highly crystalline nature. These results confirm the high chemical stability of the MIL-100(Fe) framework even when exposed to aqueous media.

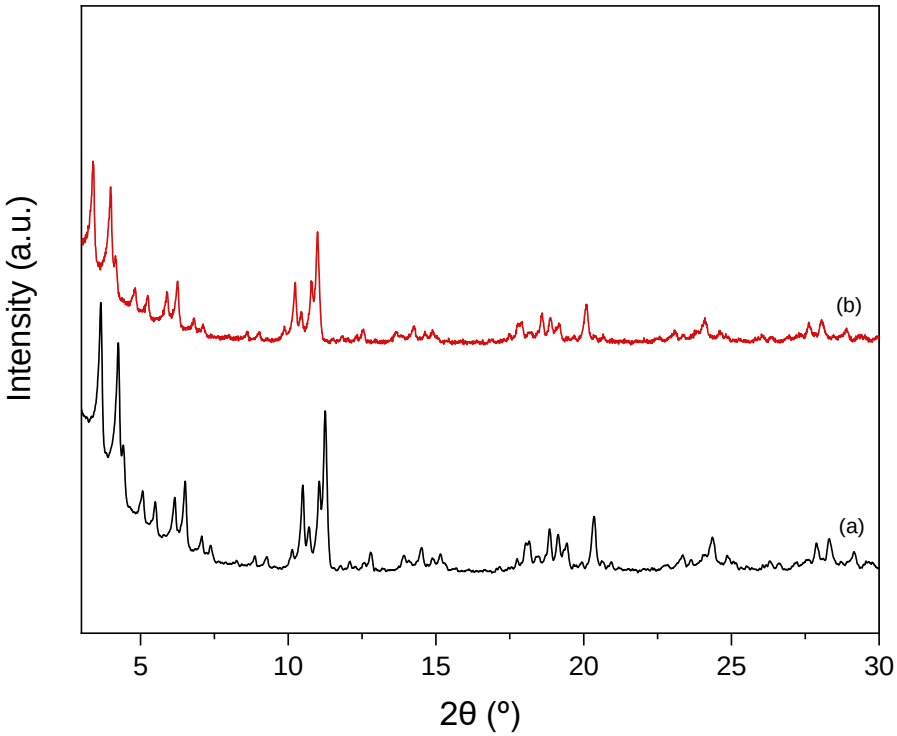

Figure 6.7. PXRD patterns of MIL-100(Fe) (a) before and (b) after adsorption studies.

6.2.2. FT-IR

After the adsorption studies, the molecular structure of MIL-100(Fe) was analysed by FT-IR and the obtained spectrum was compared with the one from the as-synthetized MIL-100(Fe), as demonstrated in Figure 6.8.

As it can be seen, the infrared spectrum of MIL-100(Fe) after adsorption revealed all the characteristic vibrational bands of MIL-100(Fe) framework without apparent shifts in their wavenumbers.

Moreover, the absence of additional vibrational bands at ca. 1710-1720 cm^{-1} attributed to the stretching vibrational mode of the C=O bonds of free carboxyl groups could be a good indicator that hydrolysis did not occur in the Fe–O bonds, otherwise free trimesic acid molecules would be present. Therefore, these observations indicate that MIL-100(Fe) maintained its framework integrity during the adsorption process, which is in agreement with the PXRD results.

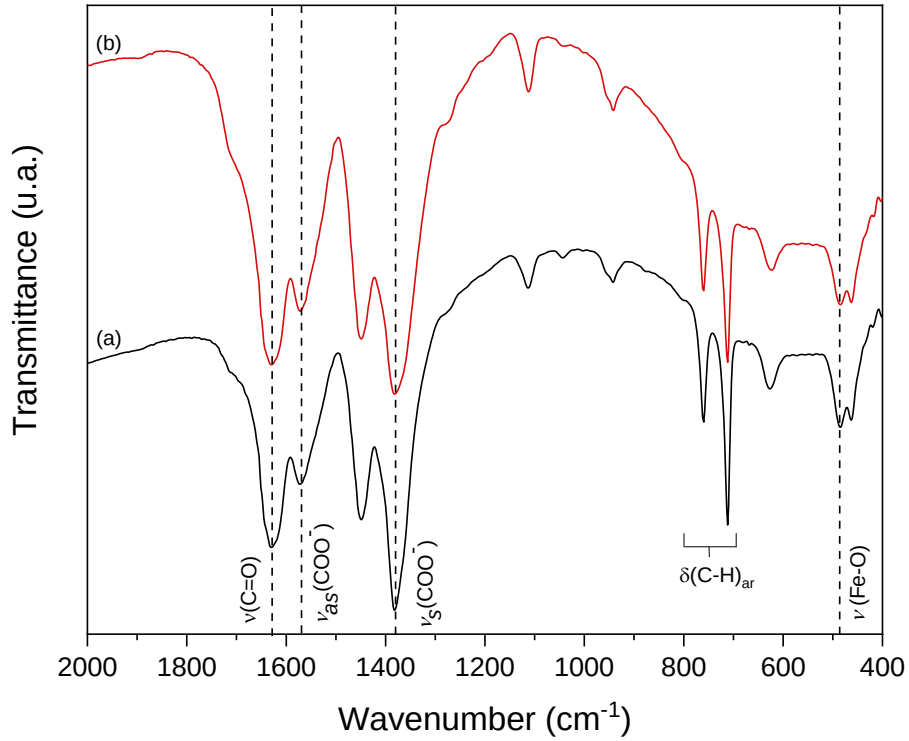

Figure 6.8. FT-IR spectrum of MIL-100(Fe) (a) before and (b) after the adsorption studies.

6.2.3. SEM/EDS

The morphology and particle size of MIL-100(Fe) loaded with Cu^{2+} ions were evaluated by SEM and its chemical composition was assessed by EDS analysis. In Figure 6.9 and 6.10 are represented the obtained micrographs at different magnifications and the EDS spectrum, respectively.

The gathered results from the SEM micrographs revealed that the particles maintained their typical octahedral shape, as observed for the as-synthetized MIL-100(Fe) particles (see section 3.1.4.). The average size of MIL-100(Fe) after adsorption of Cu^{2+} ions was 225 ± 57 nm, which is in the same size range of the pristine MOF.

The EDS analysis allowed for the detection of the main chemical components of the MOF structure, such as iron, carbon and oxygen, as well as for the copper element, confirming that the Cu^{2+} ions were indeed adsorbed at the internal or external surface of the MOF.

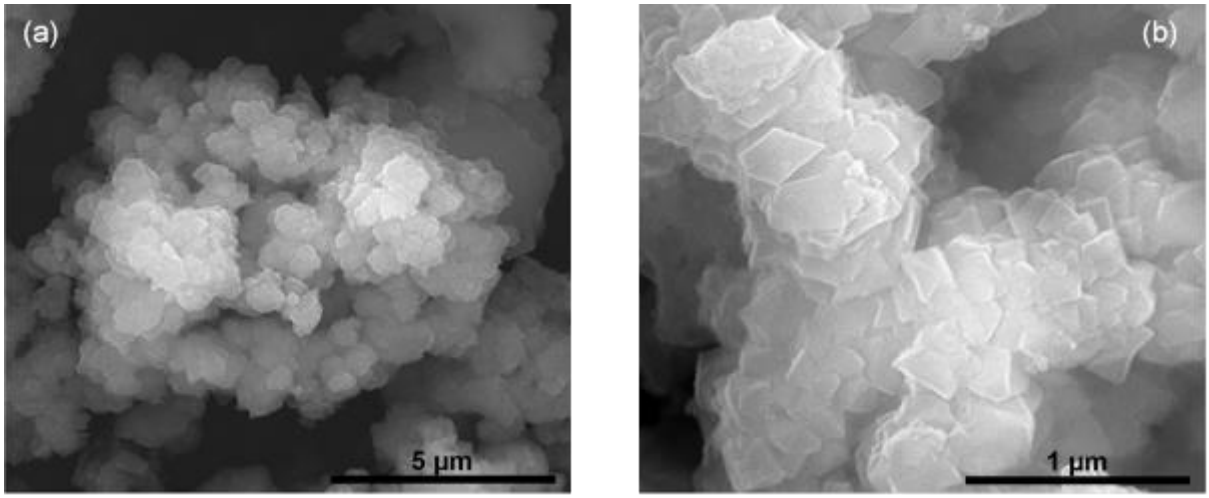

Figure 6.9. SEM micrographs of MIL-100(Fe) after adsorption studies at different magnifications (a) 2,000x and (b) 10,000x.

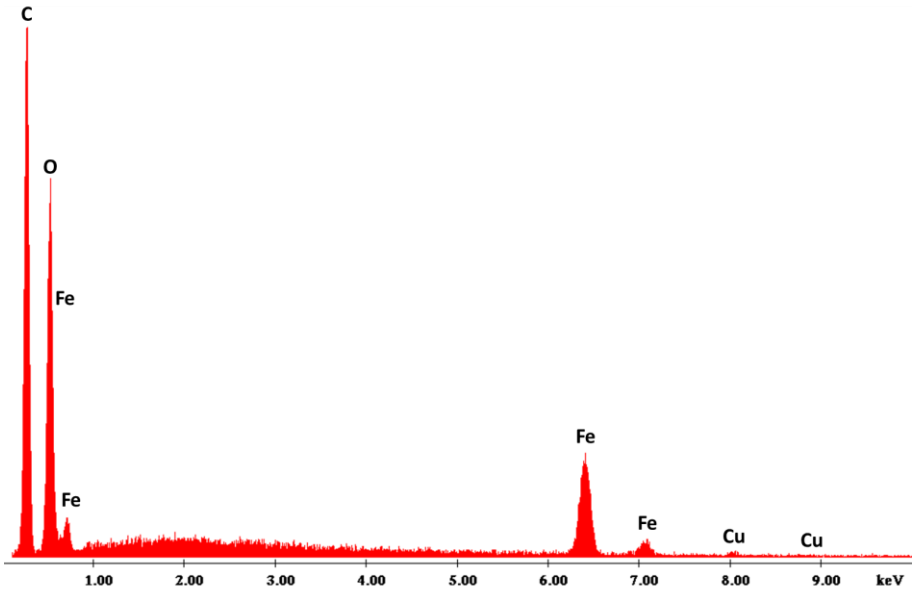

Figure 6.10. EDS spectrum of MIL-100(Fe) after adsorption of Cu^{2+} ions.

6.3. ZIF-DPC

6.3.1. PXRD

In an attempt to evaluate if there were any changes in the crystalline structure of ZIF-DPC after the adsorption studies, a PXRD analysis was conducted. Through comparison of the PXRD patterns of ZIF-DPC before and after adsorption of Cu^{2+} ions (Figure 6.11), it can be observed that all the diffraction peaks related to the graphitic carbon matrix and the metallic cobalt particles were preserved. Thus, confirming that the composite material maintained its structural integrity throughout the adsorption experiments, proving its chemical stability and suitability for application in aqueous solutions.

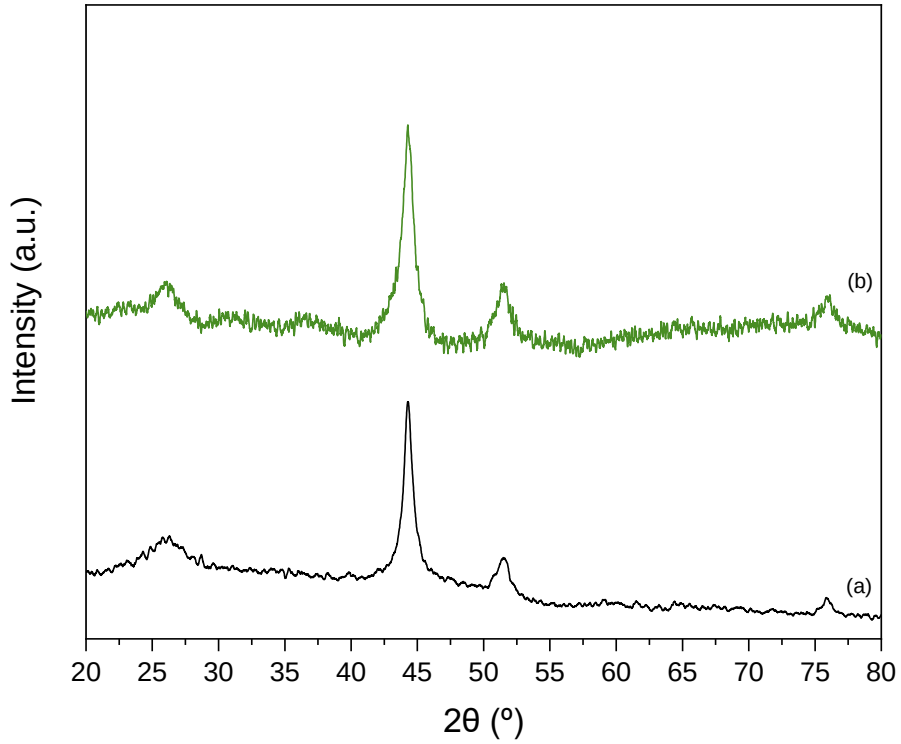

Figure 6.11. PXRD patterns of ZIF-DPC (a) before and (b) after the adsorption of Cu^{2+}.

6.3.2. FT-IR

Figure 6.12 displays the infrared spectra of ZIF-DPC before and after the adsorption of Cu^{2+} ions. Some differences between both spectra can be observed, regarding the intensities and shapes of the vibrational bands. The broad vibrational band at 1040 cm^{-1} assigned to the C–N stretching vibrational mode almost disappeared after the adsorption process, which could be due to the influence of Cu···N–C interactions. Nevertheless,

both infrared absorption profiles are similar, suggesting the structural preservation of ZIF-DPC after the adsorption process.

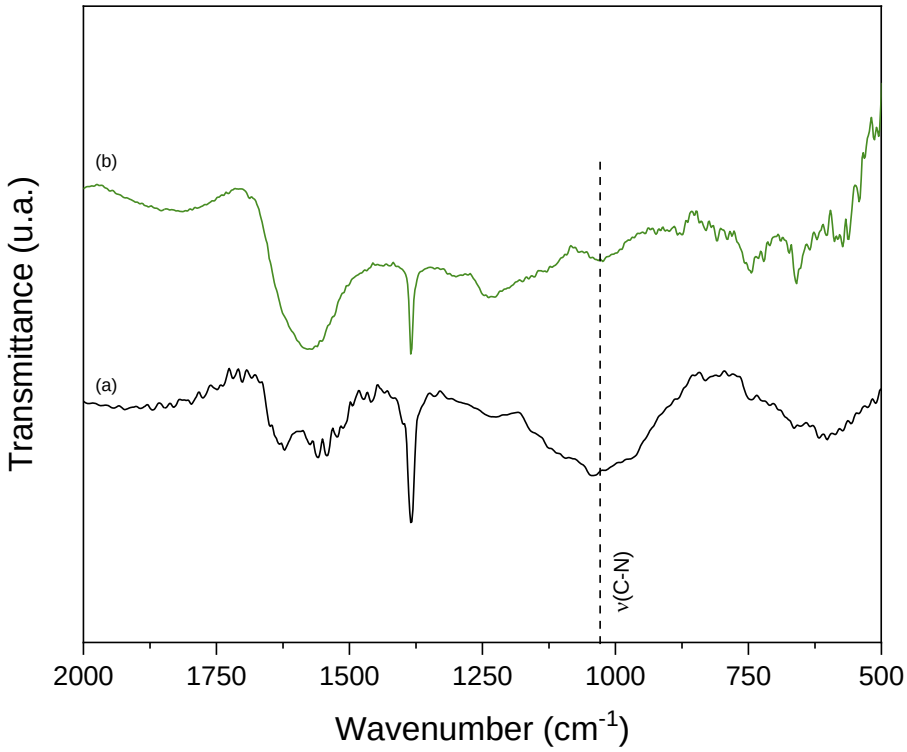

Figure 6.12. FT-IR spectra of ZIF-DPC (a) before and (b) after the adsorption of Cu^{2+} ions.

6.3.3. SEM/EDS

The SEM micrographs (Figure 6.13) revealed that after the adsorption studies, the morphology of ZIF-DPC particles was changed in comparison to the starting material, exhibiting irregular shapes and wide variety of sizes. Similar observations have been reported in the literature concerning materials applied in adsorption studies and this occurrence has been attributed to the mechanical forces that materials are subjected to, when kept under magnetic stirring.[226]

The EDS spectrum confirmed the presence of cobalt and nitrogen elements arising from the composite material. Moreover, the presence of copper was also detected, proving that the Cu^{2+} ions were indeed adsorbed by the material (Figure 6.14).

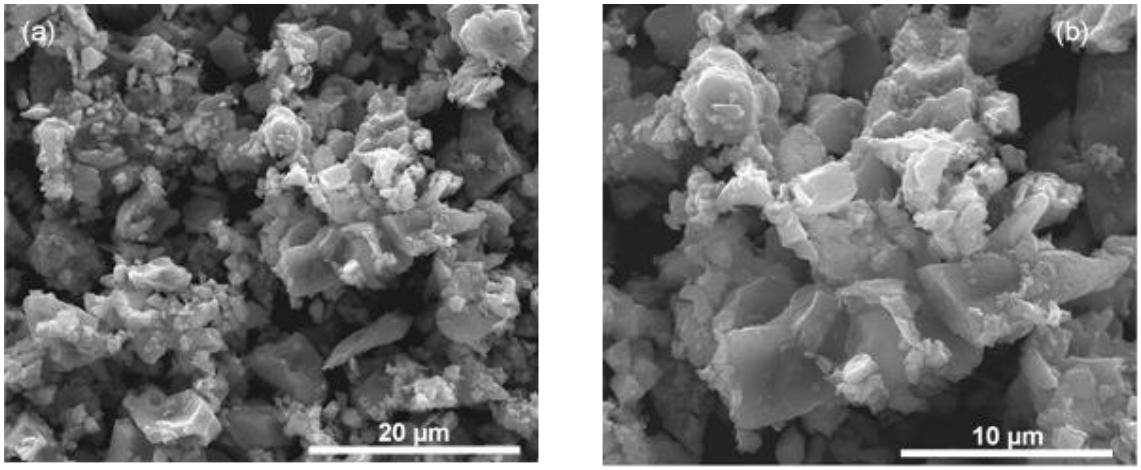

Figure 6.13. SEM micrographs of ZIF-DPC after the adsorption process at different magnifications (a) 5,000x and (b) 10,000x.

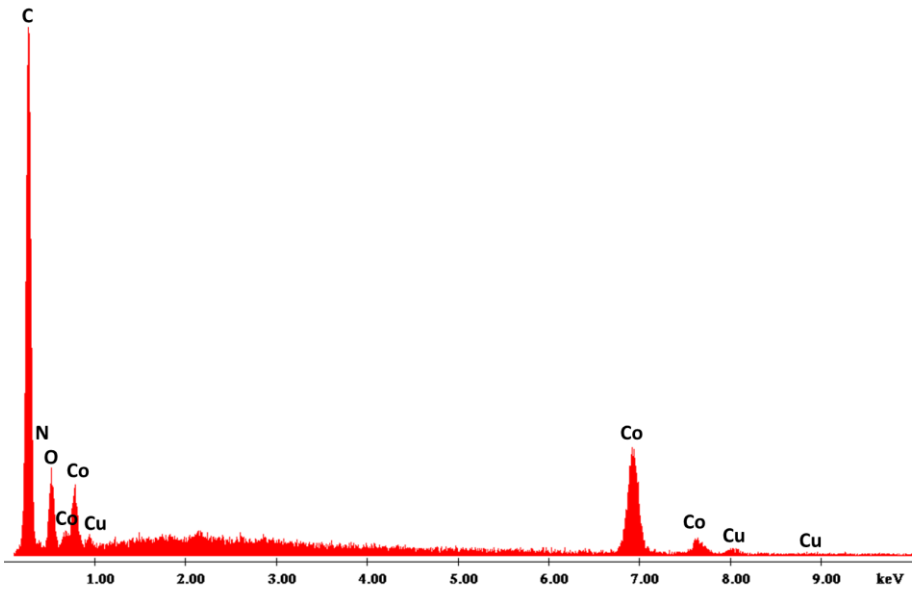

Figure 6.14. EDS spectrum of ZIF-DPC after adsorption of Cu^{2+} ions.

7. Final Conclusions

One of the greatest challenges Humankind is facing in the twenty-first century is water pollution, which poses harmful risks to the whole environment and consequently threatens the sustainability of life on Earth.

Amongst several hazardous wastes that are daily disposed in water sources, heavy metals are the ones that raise the most concern, owing to their high toxicity and persistency in the environment. Henceforth, the development of sustainable and advanced methods for an efficient removal of these substances is of uttermost importance towards environmental balance and preservation.

Nowadays, adsorption is considered one of the most sustainable and eco-friendly techniques towards wastewater treatment, due to its simple, versatile and cost-effective operational conditions. To fulfil these requirements, adsorbents should present well-defined structural properties and high accessible surface area to achieve greater adsorption capacities.

Over the last years, MOFs have revealed to be promising high-performance adsorbents for water purification applications, owing to their robust crystalline frameworks with intrinsic permanent porosity and high specific surface areas. However, there are still some limitations regarding their separation and recycling when applied in aqueous solutions. To circumvent this, one could use MOF-based adsorbents with magnetic properties, that could be elutriated by an external magnetic field.

Keeping this in mind, the scope of this work was focused on three main goals: (i) preparation of iron- and cobalt-based MOFs with different underlying topologies as well as magnetic MOF-based composites through different strategies; (ii) perform complete characterization of the outcome products through well-established techniques (PXRD, FT-IR, SEM/EDS, TGA and N_2 adsorption/desorption isotherms) and (iii) evaluation of their adsorption ability for copper removal from aqueous solutions.

All the prepared materials revealed highly crystalline structures with well-defined morphologies and narrow particle size distribution, confirming the effectiveness of the synthetic routes applied. Moreover, their textural properties were in agreement with their intrinsic structural features and characteristic flexible behaviours upon external stimuli.

In the adsorption studies, we assessed the maximum adsorption capacity of each adsorbent material towards copper ions. To accomplish this, we investigated the effect of key experimental parameters that pose major impacts on the overall adsorption process, such as solution pH, adsorbent dosage (solid/liquid ratio), contact time and initial adsorbate concentration. We have also applied commonly used mathematical models to assess important parameters concerning the kinetics and equilibrium of the

adsorption process in order to evaluate the performance of the adsorbents and potential mechanisms by which the overall process occur.

From the gathered results throughout the experimental work, we concluded that the adsorption of copper ions was promoted under mild acidic conditions at an adsorbent dosage of 1.00 g/L. All tested materials, expect for MIL-53(Fe), revealed high removal efficiencies, emphasizing the great affinity of copper towards the adsorbents surface. MIL-88B(Fe) revealed to be the most promising of the tested materials, owing to its fast adsorption rate and higher maximum adsorption capacity, which was ten-fold better than the other adsorbents.

Moreover, considering the obtained results regarding both surface charge and specific surface area, we can suggest that the adsorption of copper ions by the studied adsorbents is mainly due to the electrostatic interactions and internal diffusion through the porous structures, along with large swelling breathing behaviour from MIL-88B(Fe).

Even though further recycling studies are required in order to assess the best experimental conditions to maximize the cost-effectiveness and viability of the process, the results were very promising and hopeful towards future applications, due to the high adsorption efficiency observed even in the absence of any desorption treatment, together with their enhanced processability (recovery and applicability).

Another positive aspect that we discovered over the course of this project, was the outstanding chemical stability that all adsorbents revealed after the adsorption studies, especially considering that, one of the main challenges of using MOF-based materials in water applications is their relatively low stability when exposed to aqueous solutions, which is a promising indication of their viability for practical applications.

In conclusion, the main objectives of this project were accomplished. We effectively prepared highly crystalline MOFs as well as magnetic MOF-based materials. All key factors influencing adsorption processes were also successfully investigated, thus uncovering high adsorption capacities towards copper ions.

These findings have paved the way for future work concerning the enhancement of the recycling performances of each adsorbent throughout consecutive cycles with and without desorption processes, application of different eluents and evaluation of their desorption efficiencies, as well as their impact on the material structural integrity and finally, assessment of the adsorptive performance of the most promising adsorbents in real water samples.

8. References

1. Vörösmarty, C. J.; McIntyre, P. B.; Gessner, M. O.; Dudgeon, D.; Prusevich, A.; Green, P.; Glidden, S.; Bunn, S. E.; Sullivan, C. A.; Liermann, C. R.; Davies, P. M., Global threats to human water security and river biodiversity. *Nature* **2010**, *467* (7315), 555-561.
2. WHO, *Guidelines for Drinking-Water Quality: Fourth Edition Incorporating the First Addendum*. Geneva **2017**, pp.40-45
3. Li, R.; Zhang, L.; Wang, P., Rational design of nanomaterials for water treatment. *Nanoscale* **2015,** *7* (41), 17167-17194.
4. Giusti, L., A review of waste management practices and their impact on human health. *Waste Management* **2009,** *29* (8), 2227-2239.
5. Mon, M.; Bruno, R.; Ferrando-Soria, J.; Armentano, D.; Pardo, E., Metal–organic framework technologies for water remediation: towards a sustainable ecosystem. *Journal of Materials Chemistry A* **2018,** *6* (12), 4912-4947.
6. Sharma, S.; Bhattacharya, A., Drinking water contamination and treatment techniques. *Applied Water Science* **2017,** *7* (3), 1043-1067.
7. Schwarzenbach, R. P.; Egli, T.; Hofstetter, T. B.; Gunten, U. v.; Wehrli, B., Global Water Pollution and Human Health. *Annual Review of Environment and Resources* **2010,** *35* (1), 109-136.
8. EPA, U. S. Types of Drinking Water Contaminants. https://www.epa.gov/ccl/types-drinking-water-contaminants (accessed March 18th 2020).
9. Chapman, P. M., Determining when contamination is pollution — Weight of evidence determinations for sediments and effluents. *Environment International* **2007,** *33* (4), 492-501.
10. Burakov, A. E.; Galunin, E. V.; Burakova, I. V.; Kucherova, A. E.; Agarwal, S.; Tkachev, A. G.; Gupta, V. K., Adsorption of heavy metals on conventional and nanostructured materials for wastewater treatment purposes: A review. *Ecotoxicology and Environmental Safety* **2018,** *148*, 702-712.
11. Fawell, J.; Nieuwenhuijsen, M. J., Contaminants in drinking water: Environmental pollution and health. *British Medical Bulletin* **2003,** *68* (1), 199-208.
12. Gupta, V. K.; Ali, I.; Saleh, T. A.; Nayak, A.; Agarwal, S., Chemical treatment technologies for waste-water recycling—an overview. *RSC Advances* **2012,** *2* (16), 6380-6388.
13. Hariharan, C., Photocatalytic degradation of organic contaminants in water by ZnO nanoparticles: Revisited. *Applied Catalysis A: General* **2006,** *304*, 55-61.
14. Scott, T. B.; Popescu, I. C.; Crane, R. A.; Noubactep, C., Nano-scale metallic iron for the treatment of solutions containing multiple inorganic contaminants. *Journal of Hazardous Materials* **2011,** *186* (1), 280-287.
15. Fu, F.; Cheng, Z.; Lu, J., Synthesis and use of bimetals and bimetal oxides in contaminants removal from water: a review. *RSC Advances* **2015,** *5* (104), 85395-85409.
16. Fu, F.; Wang, Q., Removal of heavy metal ions from wastewaters: A review. *Journal of Environmental Management* **2011,** *92* (3), 407-418.
17. Jain, C. K.; Malik, D. S.; Yadav, A. K., Applicability of plant based biosorbents in the removal of heavy metals: a review. *Environmental Processes* **2016,** *3* (2), 495-523.
18. O'Connell, D. W.; Birkinshaw, C.; O'Dwyer, T. F., Heavy metal adsorbents prepared from the modification of cellulose: A review. *Bioresource Technology* **2008,** *99* (15), 6709-6724.
19. EPA, U. S. National Primary Drinking Water Regulations. https://www.epa.gov/ground-water-and-drinking-water/national-primary-drinking-water-regulations#Inorganic (accessed March 22nd 2020).
20. Carolin, C. F.; Kumar, P. S.; Saravanan, A.; Joshiba, G. J.; Naushad, M., Efficient techniques for the removal of toxic heavy metals from aquatic environment: A review. *Journal of Environmental Chemical Engineering* **2017,** *5* (3), 2782-2799.

21. John C. Crittenden, R. R. T., David W. Hand, Kerry J. Howe and George Tchobanoglous, Water Quality Management Strategies. In *MWH's Water Treatment: Principles and Design, Third Edition*, John Wiley & Sons, Inc. **2012**, pp 165-224.
22. Peirce, J. J.; Weiner, R. F.; Vesilind, P. A., Chapter 8 - Wastewater Treatment. In *Environmental Pollution and Control (Fourth Edition)*, Peirce, J. J.; Weiner, R. F.; Vesilind, P. A., Eds. Butterworth-Heinemann: Woburn **1998**, pp 105-123.
23. Foresti, E.; Zaiat, M.; Vallero, M., Anaerobic Processes as the Core Technology for Sustainable Domestic Wastewater Treatment: Consolidated Applications, New Trends,Perspectives, and Challenges. *Reviews in Environmental Science and Bio/Technology* **2006,** *5* (1), 3-19.
24. Talarposhti, A. M.; Donnelly, T.; Anderson, G. K., Colour removal from a simulated dye wastewater using a two-phase Anaerobic packed bed reactor. *Water Research* **2001,** *35* (2), 425-432.
25. Wang, L. K.; Hung, Y. T.; Shammas, N. K., *Physicochemical Treatment Processes*. Humana Press: 2007.
26. Aderhold, D.; Williams, C. J.; Edyvean, R. G. J., The removal of heavy-metal ions by seaweeds and their derivatives. *Bioresource Technology* **1996,** *58* (1), 1-6.
27. Shukla, A.; Zhang, Y.-H.; Dubey, P.; Margrave, J. L.; Shukla, S. S., The role of sawdust in the removal of unwanted materials from water. *Journal of Hazardous Materials* **2002,** *95* (1), 137-152.
28. Bilal, M.; Shah, J. A.; Ashfaq, T.; Gardazi, S. M. H.; Tahir, A. A.; Pervez, A.; Haroon, H.; Mahmood, Q., Waste biomass adsorbents for copper removal from industrial wastewater—A review. *Journal of Hazardous Materials* **2013,** *263*, 322-333.
29. Kołodyńska, Z. H. D., Selective Removal of Heavy Metal Ions from Waters and Waste Waters Using Ion Exchange Methods. In *Ion Exchange Technologies*, Kilislioğlu, A., Ed. IntechOpen: 2012.
30. Farooq, U.; Kozinski, J. A.; Khan, M. A.; Athar, M., Biosorption of heavy metal ions using wheat based biosorbents – A review of the recent literature. *Bioresource Technology* **2010,** *101* (14), 5043-5053.
31. Alyüz, B.; Veli, S., Kinetics and equilibrium studies for the removal of nickel and zinc from aqueous solutions by ion exchange resins. *Journal of Hazardous Materials* **2009,** *167* (1), 482-488.
32. John C. Crittenden, R. R. T., David W. Hand, Kerry J. Howe, George Tchobanoglous, Membrane Filtration. In *MWH's Water Treatment: Principles and Design*, 3rd ed.; MWH: 2012.
33. Dlask, O.; Václavíková, N., Electrodialysis with ultrafiltration membranes for peptide separation. *Chemical Papers* **2018,** *72* (2), 261-271.
34. Pearce, G., Introduction to membranes: Filtration for water and wastewater treatment. *Filtration & Separation* **2007,** *44* (2), 24-27.
35. Greenlee, L. F.; Lawler, D. F.; Freeman, B. D.; Marrot, B.; Moulin, P., Reverse osmosis desalination: Water sources, technology, and today's challenges. *Water Research* **2009,** *43* (9), 2317-2348.
36. Rezakazemi, M.; Khajeh, A.; Mesbah, M., Membrane filtration of wastewater from gas and oil production. *Environmental Chemistry Letters* **2018,** *16* (2), 367-388.
37. Yurlova, L.; Kryvoruchko, A.; Kornilovich, B., Removal of Ni(II) ions from wastewater by micellar-enhanced ultrafiltration. *Desalination* **2002,** *144* (1), 255-260.
38. Moran, S., Chapter 7 - Clean water unit operation design: Physical processes. In *An Applied Guide to Water and Effluent Treatment Plant Design*, Moran, S., Ed. Butterworth-Heinemann **2018**, pp 69-100.
39. Baker, R. W.; Low, B. T., Membrane Separation☆. In *Reference Module in Chemistry, Molecular Sciences and Chemical Engineering*, Elsevier **2015**, pp. 120-132
40. Sher, F.; Malik, A.; Liu, H., Industrial polymer effluent treatment by chemical coagulation and flocculation. *Journal of Environmental Chemical Engineering* **2013,** *1* (4), 684-689.

41. Santo, C. E.; Vilar, V. J. P.; Botelho, C. M. S.; Bhatnagar, A.; Kumar, E.; Boaventura, R. A. R., Optimization of coagulation–flocculation and flotation parameters for the treatment of a petroleum refinery effluent from a Portuguese plant. *Chemical Engineering Journal* **2012,** *183*, 117-123.
42. Russell, D. L., Coagulation, Flocculation and Chemical Treatment. In *Practical Wastewater Treatment*, John Wiley & Sons: New Jersey **2006**, pp 255-259.
43. Kurniawan, T. A.; Chan, G. Y. S.; Lo, W.-H.; Babel, S., Physico–chemical treatment techniques for wastewater laden with heavy metals. *Chemical Engineering Journal* **2006,** *118* (1), 83-98.
44. Santos, S. C. R.; Ungureanu, G.; Volf, I.; Boaventura, R. A. R.; Botelho, C. M. S., 3 - Macroalgae Biomass as Sorbent for Metal Ions. In *Biomass as Renewable Raw Material to Obtain Bioproducts of High-Tech Value*, Popa, V.; Volf, I., Eds. Elsevier: 2018; pp 69-112.
45. Dąbrowski, A., Adsorption — from theory to practice. *Advances in Colloid and Interface Science* **2001,** *93* (1), 135-224.
46. Bonilla-Petriciolet, A.; Mendoza-Castillo, D.; Reynel, H., *Adsorption Processes for Water Treatment and Purification*. 2017.
47. Hu, A.; Apblett, A., *Nanotechnology for Water Treatment and Purification*. 2014; Vol. 22.
48. Yagub, M. T.; Sen, T. K.; Afroze, S.; Ang, H. M., Dye and its removal from aqueous solution by adsorption: A review. *Advances in Colloid and Interface Science* **2014,** *209*, 172-184.
49. Sahu, J. N.; Acharya, J.; Meikap, B. C., Response surface modeling and optimization of chromium(VI) removal from aqueous solution using Tamarind wood activated carbon in batch process. *Journal of Hazardous Materials* **2009,** *172* (2), 818-825.
50. Reddy, D. H. K.; Lee, S.-M., Application of magnetic chitosan composites for the removal of toxic metal and dyes from aqueous solutions. *Advances in Colloid and Interface Science* **2013,** *201-202*, 68-93.
51. Ewecharoen, A.; Thiravetyan, P.; Wendel, E.; Bertagnolli, H., Nickel adsorption by sodium polyacrylate-grafted activated carbon. *Journal of Hazardous Materials* **2009,** *171* (1), 335-339.
52. Ali, I., New Generation Adsorbents for Water Treatment. *Chemical Reviews* **2012,** *112* (10), 5073-5091.
53. Ren, X.; Li, J.; Tan, X.; Wang, X., Comparative study of graphene oxide, activated carbon and carbon nanotubes as adsorbents for copper decontamination. *Dalton Transactions* **2013,** *42* (15), 5266-5274.
54. Mignardi, S.; Archilletti, L.; Medeghini, L.; De Vito, C., Valorization of Eggshell Biowaste for Sustainable Environmental Remediation. *Scientific Reports* **2020,** *10* (1), 2436.
55. Sheng, G.; Yang, S.; Sheng, J.; Hu, J.; Tan, X.; Wang, X., Macroscopic and Microscopic Investigation of Ni(II) Sequestration on Diatomite by Batch, XPS, and EXAFS Techniques. *Environmental Science & Technology* **2011,** *45* (18), 7718-7726.
56. Wang, S.; Peng, Y., Natural zeolites as effective adsorbents in water and wastewater treatment. *Chemical Engineering Journal* **2010,** *156* (1), 11-24.
57. Zhang, L.; Zeng, Y.; Cheng, Z., Removal of heavy metal ions using chitosan and modified chitosan: A review. *Journal of Molecular Liquids* **2016,** *214*, 175-191.
58. Crini, G., Non-conventional low-cost adsorbents for dye removal: A review. *Bioresource Technology* **2006,** *97* (9), 1061-1085.
59. Filote, C.; Volf, I.; Santos, S. C. R.; Botelho, C. M. S., Bioadsorptive removal of Pb(II) from aqueous solution by the biorefinery waste of Fucus spiralis. *Science of The Total Environment* **2019,** *648*, 1201-1209.
60. Da'na, E., Adsorption of heavy metals on functionalized-mesoporous silica: A review. *Microporous and Mesoporous Materials* **2017,** *247*, 145-157.
61. Li, J.; Wang, X.; Zhao, G.; Chen, C.; Chai, Z.; Alsaedi, A.; Hayat, T.; Wang, X., Metal–organic framework-based materials: superior adsorbents for the capture of toxic and radioactive metal ions. *Chemical Society Reviews* **2018,** *47* (7), 2322-2356.

62. Howarth, A. J.; Liu, Y.; Hupp, J. T.; Farha, O. K., Metal–organic frameworks for applications in remediation of oxyanion/cation-contaminated water. *CrystEngComm* **2015,** *17* (38), 7245-7253.
63. Gupta, V. K.; Carrott, P. J. M.; Ribeiro Carrott, M. M. L.; Suhas, Low-Cost Adsorbents: Growing Approach to Wastewater Treatment—a Review. *Critical Reviews in Environmental Science and Technology* **2009,** *39* (10), 783-842.
64. Batten, S. R.; Champness, N. R.; Chen, X.-M.; Garcia-Martinez, J.; Kitagawa, S.; Öhrström, L.; O'Keeffe, M.; Suh, M. P.; Reedijk, J., Coordination polymers, metal–organic frameworks and the need for terminology guidelines. *CrystEngComm* **2012,** *14* (9), 3001-3004.
65. Batten, S. R.; Champness, N. R.; Chen, X.-M.; Garcia-Martinez, J.; Kitagawa, S.; Öhrström, L.; O'Keeffe, M.; Suh, M. P.; Reedijk, J., Terminology of metal–organic frameworks and coordination polymers (IUPAC Recommendations 2013) **2013,** *85* (8), 1715.
66. Kitagawa, S.; Kitaura, R.; Noro, S.-i., Functional Porous Coordination Polymers. *Angewandte Chemie International Edition* **2004,** *43* (18), 2334-2375.
67. Ciurtin, D. M.; Smith, M. D.; zur Loye, H.-C., Structural diversity in the Cu(pyrazinecarboxylate)2/CdCl2 system: new one-, two- and three-dimensional mixed metal coordination polymers. *Dalton Transactions* **2003,** (7), 1245-1250.
68. Li, C.-P.; Yu, Q.; Chen, J.; Du, M., Supramolecular Coordination Complexes with 5-Sulfoisophthalic Acid and 2,5-Bipyridyl-1,3,4-Oxadiazole: Specific Sensitivity to Acidity for Cd(II) Species. *Crystal Growth & Design* **2010,** *10* (6), 2650-2660.
69. Chen, X.-M., Chapter 10 - Assembly Chemistry of Coordination Polymers. In *Modern Inorganic Synthetic Chemistry*, Xu, R.; Pang, W.; Huo, Q., Eds. Elsevier: Amsterdam **2011**; pp 207-225.
70. Wang, Q.; Astruc, D., State of the Art and Prospects in Metal–Organic Framework (MOF)-Based and MOF-Derived Nanocatalysis. *Chemical Reviews* **2020,** *120* (2), 1438-1511.
71. Yaghi, O. M.; Li, G.; Li, H., Selective binding and removal of guests in a microporous metal–organic framework. *Nature* **1995,** *378* (6558), 703-706.
72. Li, H.; Eddaoudi, M.; O'Keeffe, M.; Yaghi, O. M., Design and synthesis of an exceptionally stable and highly porous metal-organic framework. *Nature* **1999,** *402* (6759), 276-279.
73. Seth, S.; Matzger, A. J., Metal–Organic Frameworks: Examples, Counterexamples, and an Actionable Definition. *Crystal Growth & Design* **2017,** *17* (8), 4043-4048.
74. Wuttke, S., Introduction to Reticular Chemistry. Metal–Organic Frameworks and Covalent Organic Frameworks By Omar M. Yaghi, Markus J. Kalmutzki, and Christian S. Diercks. *Angewandte Chemie International Edition* **2019,** *58* (40), 14024-14024.
75. Yaghi, O. M.; O'Keeffe, M.; Ockwig, N. W.; Chae, H. K.; Eddaoudi, M.; Kim, J., Reticular synthesis and the design of new materials. *Nature* **2003,** *423* (6941), 705-714.
76. Cook, T. R.; Zheng, Y.-R.; Stang, P. J., Metal–Organic Frameworks and Self-Assembled Supramolecular Coordination Complexes: Comparing and Contrasting the Design, Synthesis, and Functionality of Metal–Organic Materials. *Chemical Reviews* **2013,** *113* (1), 734-777.
77. Chapter 1 Introduction. In *Coordination Polymers: Design, Analysis and Application*, The Royal Society of Chemistry **2009**; pp 1-18.
78. James, S. L., Metal-organic frameworks. *Chemical Society Reviews* **2003,** *32* (5), 276-288.
79. Kalmutzki, M. J.; Hanikel, N.; Yaghi, O. M., Secondary building units as the turning point in the development of the reticular chemistry of MOFs. *Science Advances* **2018,** *4* (10), eaat9180.
80. Férey, G., Hybrid porous solids: past, present, future. *Chemical Society Reviews* **2008,** *37* (1), 191-214.
81. Eubank, M. E. a. J. F., Insight into the Development of Metal-Organic Materials (MOMs): At Zeolite-like Metal-Organic Frameworks (ZMOFs). In *Metal-Organic Frameworks: Design and Application*, MacGillivray, L. R., Ed. John Wiley & Sons, Inc.: Hoboken, New Jersey, 2010.
82. Ellsworth, J. M.; zur Loye, H.-C., Metal and mixed-metal coordination polymers synthesized with pyrazine-2-carboxylate. *Dalton Transactions* **2008,** (43), 5823-5835.

83. Janiak, C.; Vieth, J. K., MOFs, MILs and more: concepts, properties and applications for porous coordination networks (PCNs). *New Journal of Chemistry* **2010,** *34* (11), 2366-2388.
84. Tanabe, K. K.; Cohen, S. M., Postsynthetic modification of metal–organic frameworks—a progress report. *Chemical Society Reviews* **2011,** *40* (2), 498-519.
85. Cohen, S. M., Postsynthetic Methods for the Functionalization of Metal–Organic Frameworks. *Chemical Reviews* **2012,** *112* (2), 970-1000.
86. Baumann, A. E.; Burns, D. A.; Liu, B.; Thoi, V. S., Metal-organic framework functionalization and design strategies for advanced electrochemical energy storage devices. *Communications Chemistry* **2019,** *2* (1), 86.
87. O'Keeffe, M.; Yaghi, O. M., Deconstructing the Crystal Structures of Metal–Organic Frameworks and Related Materials into Their Underlying Nets. *Chemical Reviews* **2012,** *112* (2), 675-702.
88. Wang, Z.; Cohen, S. M., Postsynthetic modification of metal–organic frameworks. *Chemical Society Reviews* **2009,** *38* (5), 1315-1329.
89. Zhang, W.-X.; Liao, P.-Q.; Lin, R.-B.; Wei, Y.-S.; Zeng, M.-H.; Chen, X.-M., Metal cluster-based functional porous coordination polymers. *Coordination Chemistry Reviews* **2015,** *293-294*, 263-278.
90. Furukawa, H.; Cordova, K. E.; O'Keeffe, M.; Yaghi, O. M., The Chemistry and Applications of Metal-Organic Frameworks. *Science* **2013,** *341* (6149), 1230444.
91. Kirchon, A.; Feng, L.; Drake, H. F.; Joseph, E. A.; Zhou, H.-C., From fundamentals to applications: a toolbox for robust and multifunctional MOF materials. *Chemical Society Reviews* **2018,** *47* (23), 8611-8638.
92. Du, M.; Li, C.-P.; Liu, C.-S.; Fang, S.-M., Design and construction of coordination polymers with mixed-ligand synthetic strategy. *Coordination Chemistry Reviews* **2013,** *257* (7), 1282-1305.
93. Helal, A.; Yamani, Z. H.; Cordova, K. E.; Yaghi, O. M., Multivariate metal-organic frameworks. *National Science Review* **2017,** *4* (3), 296-298.
94. Horike, S.; Shimomura, S.; Kitagawa, S., Soft porous crystals. *Nature Chemistry* **2009,** *1* (9), 695-704.
95. Susumu, K.; Mitsuru, K., Functional Micropore Chemistry of Crystalline Metal Complex-Assembled Compounds. *Bulletin of the Chemical Society of Japan* **1998,** *71* (8), 1739-1753.
96. Liu, J.; Chen, L.; Cui, H.; Zhang, J.; Zhang, L.; Su, C.-Y., Applications of metal–organic frameworks in heterogeneous supramolecular catalysis. *Chemical Society Reviews* **2014,** *43* (16), 6011-6061.
97. Kitagawa, S.; Uemura, K., Dynamic porous properties of coordination polymers inspired by hydrogen bonds. *Chemical Society Reviews* **2005,** *34* (2), 109-119.
98. Schneemann, A.; Bon, V.; Schwedler, I.; Senkovska, I.; Kaskel, S.; Fischer, R. A., Flexible metal–organic frameworks. *Chemical Society Reviews* **2014,** *43* (16), 6062-6096.
99. Lee, J. H.; Jeoung, S.; Chung, Y. G.; Moon, H. R., Elucidation of flexible metal-organic frameworks: Research progresses and recent developments. *Coordination Chemistry Reviews* **2019,** *389*, 161-188.
100. Millange, F.; Serre, C.; Férey, G., Synthesis, structure determination and properties of MIL-53as and MIL-53ht: the first Criii hybrid inorganic–organic microporous solids: Criii(OH)·{O2C–C6H4–CO2}·{HO2C–C_6H_4–CO2H}x. *Chemical Communications* **2002,** (8), 822-823.
101. Llewellyn, P. L.; Horcajada, P.; Maurin, G.; Devic, T.; Rosenbach, N.; Bourrelly, S.; Serre, C.; Vincent, D.; Loera-Serna, S.; Filinchuk, Y.; Férey, G., Complex Adsorption of Short Linear Alkanes in the Flexible Metal-Organic-Framework MIL-53(Fe). *Journal of the American Chemical Society* **2009,** *131* (36), 13002-13008.
102. Férey, G.; Serre, C., Large breathing effects in three-dimensional porous hybrid matter: facts, analyses, rules and consequences. *Chemical Society Reviews* **2009,** *38* (5), 1380-1399.
103. Stock, N.; Biswas, S., Synthesis of Metal-Organic Frameworks (MOFs): Routes to Various MOF Topologies, Morphologies, and Composites. *Chemical Reviews* **2012,** *112* (2), 933-969.

104. Van Vleet, M. J.; Weng, T.; Li, X.; Schmidt, J. R., In Situ, Time-Resolved, and Mechanistic Studies of Metal–Organic Framework Nucleation and Growth. *Chemical Reviews* **2018,** *118* (7), 3681-3721.
105. Dey, C.; Kundu, T.; Biswal, B.; Mallick, A.; Banerjee, R., ChemInform Abstract: Crystalline Metal-Organic Frameworks (MOFs): Synthesis, Structure and Function. *Acta crystallographica. Section B, Structural science* **2014,** *70*, 3-10.
106. Seoane, B.; Castellanos, S.; Dikhtiarenko, A.; Kapteijn, F.; Gascon, J., Multi-scale crystal engineering of metal organic frameworks. *Coordination Chemistry Reviews* **2016,** *307*, 147-187.
107. Seetharaj, R.; Vandana, P. V.; Arya, P.; Mathew, S., Dependence of solvents, pH, molar ratio and temperature in tuning metal organic framework architecture. *Arabian Journal of Chemistry* **2019,** *12* (3), 295-315.
108. Rowsell, J. L. C.; Yaghi, O. M., Metal–organic frameworks: a new class of porous materials. *Microporous and Mesoporous Materials* **2004,** *73* (1), 3-14.
109. Long, L.-S., pH effect on the assembly of metal–organic architectures. *CrystEngComm* **2010,** *12* (5), 1354-1365.
110. Remya, V. R.; Kurian, M., Synthesis and catalytic applications of metal–organic frameworks: a review on recent literature. *International Nano Letters* **2019,** *9* (1), 17-29.
111. Butova, V.; Soldatov, M.; Guda, A.; Lomachenko, K.; Lamberti, C., Metal-organic frameworks: structure, properties, methods of synthesis, and characterization. *Russian Chemical Reviews* **2016,** *85*, 280-307.
112. Safaei, M.; Foroughi, M. M.; Ebrahimpoor, N.; Jahani, S.; Omidi, A.; Khatami, M., A review on metal-organic frameworks: Synthesis and applications. *TrAC Trends in Analytical Chemistry* **2019,** *118*, 401-425.
113. Sun, Y.; Zhou, H.-C., Recent progress in the synthesis of metal–organic frameworks. *Science and Technology of Advanced Materials* **2015,** *16* (5), 054202.
114. Dhaka, S.; Kumar, R.; Deep, A.; Kurade, M. B.; Ji, S.-W.; Jeon, B.-H., Metal–organic frameworks (MOFs) for the removal of emerging contaminants from aquatic environments. *Coordination Chemistry Reviews* **2019,** *380*, 330-352.
115. Wu, Y.; Pang, H.; Liu, Y.; Wang, X.; Yu, S.; Fu, D.; Chen, J.; Wang, X., Environmental remediation of heavy metal ions by novel-nanomaterials: A review. *Environmental Pollution* **2019,** *246*, 608-620.
116. Hasan, Z.; Jhung, S. H., Removal of hazardous organics from water using metal-organic frameworks (MOFs): Plausible mechanisms for selective adsorptions. *Journal of Hazardous Materials* **2015,** *283*, 329-339.
117. Ramanayaka, S.; Vithanage, M.; Sarmah, A.; An, T.; Kim, K.-H.; Ok, Y. S., Performance of metal–organic frameworks for the adsorptive removal of potentially toxic elements in a water system: a critical review. *RSC Advances* **2019,** *9* (59), 34359-34376.
118. Ding, M.; Cai, X.; Jiang, H.-L., Improving MOF stability: approaches and applications. *Chemical Science* **2019,** *10* (44), 10209-10230.
119. Yuan, S.; Feng, L.; Wang, K.; Pang, J.; Bosch, M.; Lollar, C.; Sun, Y.; Qin, J.; Yang, X.; Zhang, P.; Wang, Q.; Zou, L.; Zhang, Y.; Zhang, L.; Fang, Y.; Li, J.; Zhou, H.-C., Stable Metal–Organic Frameworks: Design, Synthesis, and Applications. *Advanced Materials* **2018,** *30* (37), 1704303.
120. Serre, G. M. S. W. C., The Stability of Metal–Organic Frameworks. In *Metal-Organic Frameworks* **2018**; pp 1-28.
121. Maya, F.; Palomino Cabello, C.; Frizzarin, R. M.; Estela, J. M.; Turnes Palomino, G.; Cerdà, V., Magnetic solid-phase extraction using metal-organic frameworks (MOFs) and their derived carbons. *TrAC Trends in Analytical Chemistry* **2017,** *90*, 142-152.
122. Dong, Z.; Le, X.; Liu, Y.; Dong, C.; Ma, J., Metal organic framework derived magnetic porous carbon composite supported gold and palladium nanoparticles as highly efficient and recyclable catalysts for reduction of 4-nitrophenol and hydrodechlorination of 4-chlorophenol. *Journal of Materials Chemistry A* **2014,** *2* (44), 18775-18785.

123. Ma, Y. J.; Jiang, X. X.; Lv, Y. K., Recent Advances in Preparation and Applications of Magnetic Framework Composites. *Chemistry – An Asian Journal* **2019,** *14* (20), 3515-3530.
124. Ricco, R.; Malfatti, L.; Takahashi, M.; Hill, A. J.; Falcaro, P., Applications of magnetic metal–organic framework composites. *Journal of Materials Chemistry A* **2013,** *1* (42), 13033-13045.
125. Gao, Y.; Liu, G.; Gao, M.; Huang, X.; Xu, D., Recent Advances and Applications of Magnetic Metal-Organic Frameworks in Adsorption and Enrichment Removal of Food and Environmental Pollutants. *Critical Reviews in Analytical Chemistry* **2019**, 1-13.
126. Wang, J.; Wang, Y.; Hu, H.; Yang, Q.; Cai, J., From metal–organic frameworks to porous carbon materials: recent progress and prospects from energy and environmental perspectives. *Nanoscale* **2020,** *12* (7), 4238-4268.
127. Chen, Y.-Z.; Zhang, R.; Jiao, L.; Jiang, H.-L., Metal–organic framework-derived porous materials for catalysis. *Coordination Chemistry Reviews* **2018,** *362*, 1-23.
128. Zhang, Y.; Yang, L.; Yan, L.; Wang, G.; Liu, A., Recent advances in the synthesis of spherical and nanoMOF-derived multifunctional porous carbon for nanomedicine applications. *Coordination Chemistry Reviews* **2019,** *391*, 69-89.
129. Lee, K. J.; Lee, J. H.; Jeoung, S.; Moon, H. R., Transformation of Metal–Organic Frameworks/Coordination Polymers into Functional Nanostructured Materials: Experimental Approaches Based on Mechanistic Insights. *Accounts of Chemical Research* **2017,** *50* (11), 2684-2692.
130. Wu, W.; Lin, F.; Yang, X.; Wang, B.; Lu, X.; Chen, Q.; Ye, F.; Zhao, S., Facile synthesis of magnetic carbon nanotubes derived from ZIF-67 and application to magnetic solid-phase extraction of profens from human serum. *Talanta* **2020,** *207*, 120284.
131. Millange, F.; Guillou, N.; Walton, R. I.; Grenèche, J.-M.; Margiolaki, I.; Férey, G., Effect of the nature of the metal on the breathing steps in MOFs with dynamic frameworks. *Chemical Communications* **2008,** (39), 4732-4734.
132. Serre, C.; Mellot-Draznieks, C.; Surblé, S.; Audebrand, N.; Filinchuk, Y.; Férey, G., Role of Solvent-Host Interactions That Lead to Very Large Swelling of Hybrid Frameworks. *Science* **2007,** *315* (5820), 1828.
133. Surblé, S.; Serre, C.; Mellot-Draznieks, C.; Millange, F.; Férey, G., A new isoreticular class of metal-organic-frameworks with the MIL-88 topology. *Chemical Communications* **2006,** (3), 284-286.
134. Horcajada, P.; Surblé, S.; Serre, C.; Hong, D.-Y.; Seo, Y.-K.; Chang, J.-S.; Grenèche, J.-M.; Margiolaki, I.; Férey, G., Synthesis and catalytic properties of MIL-100(Fe), an iron(iii) carboxylate with large pores. *Chemical Communications* **2007,** (27), 2820-2822.
135. Kwon, H. T.; Jeong, H.-K.; Lee, A. S.; An, H. S.; Lee, J. S., Heteroepitaxially Grown Zeolitic Imidazolate Framework Membranes with Unprecedented Propylene/Propane Separation Performances. *Journal of the American Chemical Society* **2015,** *137* (38), 12304-12311.
136. Tian, H.; Peng, J.; Du, Q.; Hui, X.; He, H., One-pot sustainable synthesis of magnetic MIL-100(Fe) with novel Fe3O4 morphology and its application in heterogeneous degradation. *Dalton Transactions* **2018,** *47* (10), 3417-3424.
137. Andrew Lin, K.-Y.; Hsu, F.-K., Magnetic iron/carbon nanorods derived from a metal organic framework as an efficient heterogeneous catalyst for the chemical oxidation process in water. *RSC Advances* **2015,** *5* (63), 50790-50800.
138. Xu, W. T.; Ma, L.; Ke, F.; Peng, F. M.; Xu, G. S.; Shen, Y. H.; Zhu, J. F.; Qiu, L. G.; Yuan, Y. P., Metal-organic frameworks MIL-88A hexagonal microrods as a new photocatalyst for efficient decolorization of methylene blue dye. *Dalton transactions* **2014,** *43* (9), 3792-8.
139. An, B.; Cheng, K.; Wang, C.; Wang, Y.; Lin, W., Pyrolysis of Metal–Organic Frameworks to Fe3O4@Fe5C2 Core–Shell Nanoparticles for Fischer–Tropsch Synthesis. *ACS Catalysis* **2016,** *6* (6), 3610-3618.

140. Zhang, C.; Ai, L.; Jiang, J., Solvothermal synthesis of MIL–53(Fe) hybrid magnetic composites for photoelectrochemical water oxidation and organic pollutant photodegradation under visible light. *Journal of Materials Chemistry A* **2015,** *3* (6), 3074-3081.
141. Ai, L.; Li, L.; Zhang, C.; Fu, J.; Jiang, J., MIL-53(Fe): A Metal–Organic Framework with Intrinsic Peroxidase-Like Catalytic Activity for Colorimetric Biosensing. *Chemistry – A European Journal* **2013,** *19* (45), 15105-15108.
142. Xia, W.; Zhu, J.; Guo, W.; An, L.; Xia, D.; Zou, R., Well-defined carbon polyhedrons prepared from nano metal–organic frameworks for oxygen reduction. *Journal of Materials Chemistry A* **2014,** *2* (30), 11606-11613.
143. Pereira, C.; Pereira, A. M.; Quaresma, P.; Tavares, P. B.; Pereira, E.; Araújo, J. P.; Freire, C., Superparamagnetic γ-Fe2O3@SiO2 nanoparticles: a novel support for the immobilization of [VO(acac)2]. *Dalton Transactions* **2010,** *39* (11), 2842-2854.
144. Torad, N. L.; Hu, M.; Ishihara, S.; Sukegawa, H.; Belik, A. A.; Imura, M.; Ariga, K.; Sakka, Y.; Yamauchi, Y., Direct Synthesis of MOF-Derived Nanoporous Carbon with Magnetic Co Nanoparticles toward Efficient Water Treatment. *Small* **2014,** *10* (10), 2096-2107.
145. Bouzid, J.; Elouear, Z.; Ksibi, M.; Feki, M.; Montiel, A., A study on removal characteristics of copper from aqueous solution by sewage sludge and pomace ashes. *Journal of Hazardous Materials* **2008,** *152* (2), 838-845.
146. Guo, X.; Wang, J., A general kinetic model for adsorption: Theoretical analysis and modeling. *Journal of Molecular Liquids* **2019,** *288*, 111100.
147. Foo, K. Y.; Hameed, B. H., Insights into the modeling of adsorption isotherm systems. *Chemical Engineering Journal* **2010,** *156* (1), 2-10.
148. Rahman, N.; Haseen, U., Equilibrium Modeling, Kinetic, and Thermodynamic Studies on Adsorption of Pb(II) by a Hybrid Inorganic–Organic Material: Polyacrylamide Zirconium(IV) Iodate. *Industrial & Engineering Chemistry Research* **2014,** *53* (19), 8198-8207.
149. Wang, J.; Guo, X., Adsorption isotherm models: Classification, physical meaning, application and solving method. *Chemosphere* **2020,** *258*, 127279.
150. Zaheer, Z.; AbuBaker Bawazir, W.; Al-Bukhari, S. M.; Basaleh, A. S., Adsorption, equilibrium isotherm, and thermodynamic studies to the removal of acid orange 7. *Materials Chemistry and Physics* **2019,** *232*, 109-120.
151. Leng, Y., *Materials Characterization: Introduction to Microscopic and Spectroscopic Methods*. Wiley-VCH: Weinheim, Germany **2013**.
152. Singh, A. K., Chapter 4 - Experimental Methodologies for the Characterization of Nanoparticles. In *Engineered Nanoparticles*, Singh, A. K., Ed. Academic Press: Boston **2016**; pp 125-170.
153. Pavia, D. L.; Lampman, G. M.; Kriz, G. S.; Vyvyan, J. A., *Introduction to Spectroscopy*. Cengage Learning: 2008.
154. Goldstein, J.; Newbury, D.; Joy, D.; Lyman, C.; Echlin, P.; Lifshin, E.; Sawyer, L.; Michael, J., *Scanning Electron Microscopy and X-ray Microanalysis ISBN: 0306472929*. 2003; Vol. XIX.
155. Vyazovkin, S., Thermogravimetric Analysis. In *Characterization of Materials* **2012**; pp 1-12.
156. Zhou, H.; Long, Y.; Meng, A.; Chen, S.; Li, Q.; Zhang, Y., A novel method for kinetics analysis of pyrolysis of hemicellulose, cellulose, and lignin in TGA and macro-TGA. *RSC Advances* **2015,** *5* (34), 26509-26516.
157. Thommes, M.; Kaneko, K.; Neimark, A. V.; Olivier, J. P.; Rodriguez-Reinoso, F.; Rouquerol, J.; Sing, K. S. W., Physisorption of gases, with special reference to the evaluation of surface area and pore size distribution (IUPAC Technical Report). *Pure and Applied Chemistry* **2015,** *87* (9-10), 1051.
158. Reporting Physisorption Data for Gas/Solid Systems. In *Handbook of Heterogeneous Catalysis*, pp 1217-1230.
159. Brunauer, S.; Emmett, P. H.; Teller, E., Adsorption of Gases in Multimolecular Layers. *Journal of the American Chemical Society* **1938,** *60* (2), 309-319.

160. Sing, K. S. W., Reporting physisorption data for gas/solid systems with special reference to the determination of surface area and porosity (Recommendations 1984). *Pure and Applied Chemistry* **1985,** *57* (4), 603.
161. Twyman, R. M., ATOMIC EMISSION SPECTROMETRY | Interferences and Background Correction **2005**; pp 198-203.
162. Fernández, B.; Lobo, L.; Pereiro, R., Atomic Absorption Spectrometry: Fundamentals, Instrumentation and Capabilities **2018**, pp. 160-175
163. Farrukh, M. A., *Atomic Absorption Spectroscopy* **2012**, pp.70-86
164. Loveland, P., P.J. Potts A Handbook of Silicate Rock Analysis. Blackie & Son (USA: Chapman & Hall), 1987. x + 622 pp. Price £128. ISBN: 0216917948 (USA 0412 008815). *Clay Minerals* **1987,** *22* (1), 119-120.
165. Faanu, A.; Ephraim, J. H.; Darko, E. O., Assessment of public exposure to naturally occurring radioactive materials from mining and mineral processing activities of Tarkwa Goldmine in Ghana. *Environmental Monitoring and Assessment* **2011**, *180* (1), 15-29.
166. Fang, Q.; Zhu, G.; Xue, M.; Sun, J.; Wei, Y.; Qiu, S.; Xu, R., A Metal–Organic Framework with the Zeolite MTN Topology Containing Large Cages of Volume 2.5 nm3 *Angewandte Chemie International Edition* **2005,** *44* (25), 3845-3848.
167. Lu, W.; Wei, Z.; Gu, Z.-Y.; Liu, T.-F.; Park, J.; Park, J.; Tian, J.; Zhang, M.; Zhang, Q.; Gentle Iii, T.; Bosch, M.; Zhou, H.-C., Tuning the structure and function of metal–organic frameworks via linker design. *Chemical Society Reviews* **2014,** *43* (16), 5561-5593.
168. Nehra, M.; Dilbaghi, N.; Singhal, N. K.; Hassan, A. A.; Kim, K.-H.; Kumar, S., Metal organic frameworks MIL-100(Fe) as an efficient adsorptive material for phosphate management. *Environmental Research* **2019,** *169*, 229-236.
169. Seo, Y.-K.; Yoon, J. W.; Lee, J. S.; Lee, U. H.; Hwang, Y. K.; Jun, C.-H.; Horcajada, P.; Serre, C.; Chang, J.-S., Large scale fluorine-free synthesis of hierarchically porous iron(III) trimesate MIL-100(Fe) with a zeolite MTN topology. *Microporous and Mesoporous Materials* **2012,** *157*, 137-145.
170. Wan, H.; Chen, C.; Wu, Z.; Que, Y.; Feng, Y.; Wang, W.; Wang, L.; Guan, G.; Liu, X., Encapsulation of Heteropolyanion-Based Ionic Liquid within the Metal–Organic Framework MIL-100(Fe) for Biodiesel Production. *ChemCatChem* **2015,** *7* (3), 441-449.
171. Huang, S.; Yang, K.-L.; Liu, X.-F.; Pan, H.; Zhang, H.; Yang, S., MIL-100(Fe)-catalyzed efficient conversion of hexoses to lactic acid. *RSC Advances* **2017,** *7* (10), 5621-5627.
172. Multia, J.; Khayyami, A.; Heiska, J.; Karppinen, M., Low-pressure thermogravimetric analysis for finding sublimation temperatures for organic precursors in atomic/molecular layer deposition. *Journal of Vacuum Science & Technology A* **2020,** *38* (5), 052406.
173. Zhou, D.; Chen, X.; Liang, B.; Fan, X.; Wei, X.; Liang, J.; Wang, L., Embedding MIL-100(Fe) with magnetically recyclable Fe3O4 nanoparticles for highly efficient esterification of diterpene resin acids and the associated kinetics. *Microporous and Mesoporous Materials* **2019,** *289*, 109615.
174. Simon, M. A.; Anggraeni, E.; Soetaredjo, F. E.; Santoso, S. P.; Irawaty, W.; Thanh, T. C.; Hartono, S. B.; Yuliana, M.; Ismadji, S., Hydrothermal Synthesize of HF-Free MIL-100(Fe) for Isoniazid-Drug Delivery. *Scientific Reports* **2019,** *9* (1), 16907.
175. Serre, C.; Millange, F.; Surblé, S.; Férey, G., A route to the synthesis of trivalent transition-metal porous carboxylates with trimeric secondary building units. *Angewandte Chemie (International ed. in English)* **2004,** *43* (46), 6285-9.
176. Wang, L.; Zhang, Y.; Li, X.; Xie, Y.; He, J.; Yu, J.; Song, Y., The MIL-88A-Derived Fe3O4-Carbon Hierarchical Nanocomposites for Electrochemical Sensing. *Scientific Reports* **2015,** *5* (1), 14341.
177. Liao, X.; Wang, F.; Wang, F.; Cai, Y.; Yao, Y.; Teng, B.-T.; Hao, Q.; Shuxiang, L., Synthesis of (100) surface oriented MIL-88A-Fe with rod-like structure and its enhanced fenton-like performance for phenol removal. *Applied Catalysis B: Environmental* **2019,** *259*, 118064.

178. Gholizadeh Khasevani, S.; Gholami, M. R., Engineering a highly dispersed core@shell structure for efficient photocatalysis: A case study of ternary novel BiOI@MIL-88A(Fe)@g-C3N4 nanocomposite. *Materials Research Bulletin* **2018,** *106*, 93-102.
179. Liu, N.; Huang, W.; Zhang, X.; Tang, L.; Wang, L.; Wang, Y.; Wu, M., Ultrathin graphene oxide encapsulated in uniform MIL-88A(Fe) for enhanced visible light-driven photodegradation of RhB. *Applied Catalysis B: Environmental* **2018,** *221*, 119-128.
180. Cao, Y.-Q.; Zhu, L.; Li, X.; Cao, Z.-Y.; Wu, D.; Li, A.-D., Growth characteristics of Ti-based fumaric acid hybrid thin films by molecular layer deposition. *Dalton Transactions* **2015,** *44* (33), 14782-14792.
181. Scherb, C.; Schödel, A.; Bein, T., Directing the Structure of Metal–Organic Frameworks by Oriented Surface Growth on an Organic Monolayer. *Angewandte Chemie International Edition* **2008,** *47* (31), 5777-5779.
182. Li, X.; Guo, W.; Liu, Z.; Wang, R.; Liu, H., Fe-based MOFs for efficient adsorption and degradation of acid orange 7 in aqueous solution via persulfate activation. *Applied Surface Science* **2016,** *369*, 130-136.
183. Zhao, K.; Zhang, Z.; Feng, Y.; Lin, S.; Li, H.; Gao, X., Surface oxygen vacancy modified Bi2MoO6/MIL-88B(Fe) heterostructure with enhanced spatial charge separation at the bulk & interface. *Applied Catalysis B: Environmental* **2020,** *268*, 118740.
184. Xie, D.; Ma, Y.; Gu, Y.; Zhou, H.; Zhang, H.; Wang, G.; Zhang, Y.; Zhao, H., Bifunctional NH2-MIL-88(Fe) metal–organic framework nanooctahedra for highly sensitive detection and efficient removal of arsenate in aqueous media. *Journal of Materials Chemistry A* **2017,** *5* (45), 23794-23804.
185. Hu, Y.; Huang, Z.; Liao, J.; Li, G., Chemical Bonding Approach for Fabrication of Hybrid Magnetic Metal–Organic Framework-5: High Efficient Adsorbents for Magnetic Enrichment of Trace Analytes. *Analytical Chemistry* **2013,** *85* (14), 6885-6893.
186. Jin, Y.; Zhao, C.; Lin, Y.; Wang, D.; Chen, L.; Shen, C., Fe-Based Metal-Organic Framework and Its Derivatives for Reversible Lithium Storage. *Journal of Materials Science & Technology* **2017,** *33* (8), 768-774.
187. Hou, S.; Wu, Y.-n.; Feng, L.; Chen, W.; Wang, Y.; Morlay, C.; Li, F., Green synthesis and evaluation of an iron-based metal–organic framework MIL-88B for efficient decontamination of arsenate from water. *Dalton Transactions* **2018,** *47* (7), 2222-2231.
188. Sompornpailin, D.; Ratanatawanate, C.; Sattayanon, C.; Namuangruk, S.; Punyapalakul, P., Selective adsorption mechanisms of pharmaceuticals on benzene-1,4-dicarboxylic acid-based MOFs: Effects of a flexible framework, adsorptive interactions and the DFT study. *Science of The Total Environment* **2020,** *720*, 137449.
189. Serre, C.; Millange, F.; Thouvenot, C.; Noguès, M.; Marsolier, G.; Louër, D.; Férey, G., Very Large Breathing Effect in the First Nanoporous Chromium(III)-Based Solids: MIL-53 or CrIII(OH)·{O2C−C6H4−CO2}·{HO2C−C6H4−CO2H}x·H2Oy. *Journal of the American Chemical Society* **2002,** *124* (45), 13519-13526.
190. Kriesten, M.; Hoffmann, K.; Hartmann, M., Comment on “Insight into the reversible structural crystalline-state transformation from MIL-53(Al) to MIL-68(Al)” by A. Perea-Cachero, E. Romero, C. Téllez and J. Coronas, CrystEngComm, 2018, 20, 402. *CrystEngComm* **2018,** *20* (22), 3117-3119.
191. Millange, F.; Serre, C.; Guillou, N.; Férey, G.; Walton, R. I., Structural Effects of Solvents on the Breathing of Metal–Organic Frameworks: An In Situ Diffraction Study. *Angewandte Chemie International Edition* **2008,** *47* (22), 4100-4105.
192. Liang, R.; Jing, F.; Shen, L.; Qin, N.; Wu, L., MIL-53(Fe) as a highly efficient bifunctional photocatalyst for the simultaneous reduction of Cr(VI) and oxidation of dyes. *Journal of Hazardous Materials* **2015,** *287*, 364-372.
193. Panda, R.; Rahut, S.; Basu, J. K., Preparation of a Fe2O3/MIL-53(Fe) composite by partial thermal decomposition of MIL-53(Fe) nanorods and their photocatalytic activity. *RSC Advances* **2016,** *6* (84), 80981-80985.

194. Sun, Q.; Liu, M.; Li, K.; Han, Y.; Zuo, Y.; Wang, J.; Song, C.; Zhang, G.; Guo, X., Controlled synthesis of mixed-valent Fe-containing metal organic frameworks for the degradation of phenol under mild conditions. *Dalton Transactions* **2016,** *45* (19), 7952-7959.
195. Li, X.; Gao, X.; Ai, L.; Jiang, J., Mechanistic insight into the interaction and adsorption of Cr(VI) with zeolitic imidazolate framework-67 microcrystals from aqueous solution. *Chemical Engineering Journal* **2015,** *274*, 238-246.
196. Ammar, M.; Jiang, S.; Ji, S., Heteropoly acid encapsulated into zeolite imidazolate framework (ZIF-67) cage as an efficient heterogeneous catalyst for Friedel–Crafts acylation. *Journal of Solid State Chemistry* **2016,** *233*, 303-310.
197. Lin, K.-Y. A.; Chang, H.-A., Ultra-high adsorption capacity of zeolitic imidazole framework-67 (ZIF-67) for removal of malachite green from water. *Chemosphere* **2015,** *139*, 624-631.
198. Hu, Y.; Kazemian, H.; Rohani, S.; Huang, Y.; Song, Y., In situ high pressure study of ZIF-8 by FTIR spectroscopy. *Chemical Communications* **2011,** *47* (47), 12694-12696.
199. Tran, U. P. N.; Le, K. K. A.; Phan, N. T. S., Expanding Applications of Metal−Organic Frameworks: Zeolite Imidazolate Framework ZIF-8 as an Efficient Heterogeneous Catalyst for the Knoevenagel Reaction. *ACS Catalysis* **2011,** *1* (2), 120-127.
200. Zhou, Q.; Zhu, L.; Xia, X.; Tang, H., The water – resistant zeolite imidazolate framework 67 is a viable solid phase sorbent for fluoroquinolones while efficiently excluding macromolecules. *Microchimica Acta* **2016,** *183* (6), 1839-1846.
201. Shao, J.; Wan, Z.; Liu, H.; Zheng, H.; Gao, T.; Shen, M.; Qu, Q.; Zheng, H., Metal organic frameworks-derived Co3O4 hollow dodecahedrons with controllable interiors as outstanding anodes for Li storage. *Journal of Materials Chemistry A* **2014,** *2* (31), 12194-12200.
202. Tu, M.; Wiktor, C.; Rösler, C.; Fischer, R. A., Rapid room temperature syntheses of zeolitic-imidazolate framework (ZIF) nanocrystals. *Chemical Communications* **2014,** *50* (87), 13258-13260.
203. Tripathi, M.; Dwivedi, R.; Kumar, D.; Roy, P. K., Thermal Activation of Mendable Epoxy through Inclusion of Microcapsules and Imidazole Complexes. *Polymer-Plastics Technology and Engineering* **2016,** *55* (2), 129-137.
204. Gross, A. F.; Sherman, E.; Vajo, J. J., Aqueous room temperature synthesis of cobalt and zinc sodalite zeolitic imidizolate frameworks. *Dalton Transactions* **2012,** *41* (18), 5458-5460.
205. Pereira, C.; Pereira, A. M.; Rocha, M.; Freire, C.; Geraldes, C. F. G. C., Architectured design of superparamagnetic Fe3O4 nanoparticles for application as MRI contrast agents: mastering size and magnetism for enhanced relaxivity. *Journal of Materials Chemistry B* **2015,** *3* (30), 6261-6273.
206. Das, M.; Mishra, D.; Dhak, P.; Gupta, S.; Maiti, T. K.; Basak, A.; Pramanik, P., Biofunctionalized, Phosphonate-Grafted, Ultrasmall Iron Oxide Nanoparticles for Combined Targeted Cancer Therapy and Multimodal Imaging. *Small* **2009,** *5* (24), 2883-2893.
207. Stetefeld, J.; McKenna, S. A.; Patel, T. R., Dynamic light scattering: a practical guide and applications in biomedical sciences. *Biophysical Reviews* **2016,** *8* (4), 409-427.
208. Julião, D.; Gomes, A. C.; Pillinger, M.; Valença, R.; Ribeiro, J. C.; de Castro, B.; Gonçalves, I. S.; Cunha Silva, L.; Balula, S. S., Zinc-Substituted Polyoxotungstate@amino-MIL-101(Al) – An Efficient Catalyst for the Sustainable Desulfurization of Model and Real Diesels. *European Journal of Inorganic Chemistry* **2016,** *2016* (32), 5114-5122.
209. Unal, B.; Durmus, Z.; Kavas, H.; Baykal, A.; Toprak, M. S., Synthesis, conductivity and dielectric characterization of salicylic acid–Fe3O4 nanocomposite. *Materials Chemistry and Physics* **2010,** *123* (1), 184-190.
210. Gao, Y.; Han, Z.; Hong, S.; Wu, T.; Li, X.; Qiu, J.; Sun, Z., ZIF-67-Derived Cobalt/Nitrogen-Doped Carbon Composites for Efficient Electrocatalytic N2 Reduction. *ACS Applied Energy Materials* **2019,** *2* (8), 6071-6077.

211. Liu, X.; Wang, C.; Wu, Q.; Wang, Z., Metal-organic framework-templated synthesis of magnetic nanoporous carbon as an efficient absorbent for enrichment of phenylurea herbicides. *Analytica Chimica Acta* **2015,** *870*, 67-74.
212. Kumar, M. P.; Kesavan, T.; Kalita, G.; Ragupathy, P.; Narayanan, T. N.; Pattanayak, D. K., On the large capacitance of nitrogen doped graphene derived by a facile route. *RSC Advances* **2014,** *4* (73), 38689-38697.
213. Li, X.; Qiao, Y.; Wang, C.; Shen, T.; Zhang, X.; Wang, H.; Li, Y.; Gao, W., MOF-derived Co/C nanocomposites encapsulated by Ni(OH)2 ultrathin nanosheets shell for high performance supercapacitors. *Journal of Alloys and Compounds* **2019,** *770*, 803-812.
214. Xu, X.; Yuan, T.; Zhou, Y.; Li, Y.; Lu, J.; Tian, X.; Wang, D.; Wang, J., Facile synthesis of boron and nitrogen-doped graphene as efficient electrocatalyst for the oxygen reduction reaction in alkaline media. *International Journal of Hydrogen Energy* **2014,** *39* (28), 16043-16052.
215. Horcajada, P.; Salles, F.; Wuttke, S.; Devic, T.; Heurtaux, D.; Maurin, G.; Vimont, A.; Daturi, M.; David, O.; Magnier, E.; Stock, N.; Filinchuk, Y.; Popov, D.; Riekel, C.; Férey, G.; Serre, C., How Linker's Modification Controls Swelling Properties of Highly Flexible Iron(III) Dicarboxylates MIL-88. *Journal of the American Chemical Society* **2011,** *133* (44), 17839-17847.
216. Loiseau, T.; Serre, C.; Huguenard, C.; Fink, G.; Taulelle, F.; Henry, M.; Bataille, T.; Férey, G., A Rationale for the Large Breathing of the Porous Aluminum Terephthalate (MIL-53) Upon Hydration. *Chemistry – A European Journal* **2004,** *10* (6), 1373-1382.
217. Qadir, N. U.; Said, S. A. M.; Mansour, R. B.; Mezghani, K.; Ul-Hamid, A., Synthesis, characterization, and water adsorption properties of a novel multi-walled carbon nanotube/MIL-100(Fe) composite. *Dalton Transactions* **2016,** *45* (39), 15621-15633.
218. Pooresmaeil, M.; Namazi, H., Chapter 14 - Application of polysaccharide-based hydrogels for water treatments. In *Hydrogels Based on Natural Polymers*, Chen, Y., Ed. Elsevier: 2020; pp 411-455.
219. Wang, J.; Guo, X., Adsorption kinetic models: Physical meanings, applications, and solving methods. *Journal of Hazardous Materials* **2020,** *390*, 122156.
220. Mercado-Borrayo, B. M.; Schouwenaars, R.; Litter, M. I.; Montoya-Bautista, C. V.; Ramírez-Zamora, R. M., 5 - Metallurgical Slag as an Efficient and Economical Adsorbent of Arsenic. In *Water Reclamation and Sustainability*, Ahuja, S., Ed. Elsevier: Boston, 2014; pp 95-114.
221. Li, K.; Li, J.-j.; Zhao, N.; Xie, T.-t.; Di, B.; Xu, L.-l., Thioether-based recyclable metal–organic frameworks for selective and efficient removal of Hg2+ from water. *Dalton Transactions* **2019,** *48* (48), 17800-17809.
222. Gimbert, F.; Morin-Crini, N.; Renault, F.; Badot, P.-M.; Crini, G., Adsorption isotherm models for dye removal by cationized starch-based material in a single component system: Error analysis. *Journal of Hazardous Materials* **2008,** *157* (1), 34-46.
223. Wang, L.; Shi, C.; Wang, L.; Pan, L.; Zhang, X.; Zou, J.-J., Rational design, synthesis, adsorption principles and applications of metal oxide adsorbents: a review. *Nanoscale* **2020,** *12* (8), 4790-4815.
224. Zhu, H.; Yuan, J.; Tan, X.; Zhang, W.; Fang, M.; Wang, X., Efficient removal of Pb2+ by Tb-MOFs: identifying the adsorption mechanism through experimental and theoretical investigations. *Environmental Science: Nano* **2019,** *6* (1), 261-272.
225. Esrafili, L.; Gharib, M.; Morsali, A., The targeted design of dual-functional metal–organic frameworks (DF-MOFs) as highly efficient adsorbents for Hg2+ ions: synthesis for purpose. *Dalton Transactions* **2019,** *48* (48), 17831-17839.
226. Luo, F.; Chen, J. L.; Dang, L. L.; Zhou, W. N.; Lin, H. L.; Li, J. Q.; Liu, S. J.; Luo, M. B., High-performance Hg2+ removal from ultra-low-concentration aqueous solution using both acylamide- and hydroxyl-functionalized metal–organic framework. *Journal of Materials Chemistry A* **2015,** *3* (18), 9616-9620.

227. Alnajrani, M. N.; Alsager, O. A., Removal of Antibiotics from Water by Polymer of Intrinsic Microporosity: Isotherms, Kinetics, Thermodynamics, and Adsorption Mechanism. *Scientific Reports* **2020,** *10* (1), 794.
228. Nasr, M. F.; Abo El-Ola, S. M.; Ramadan, A.; Hashem, A., A Comparative Study Between the Adsorption Behavior of Activated Carbon Fiber and Modified Alginate I. Basic Dyes Adsorption. *Polymer-Plastics Technology and Engineering* **2006,** *45* (3), 335-340.

Appendix

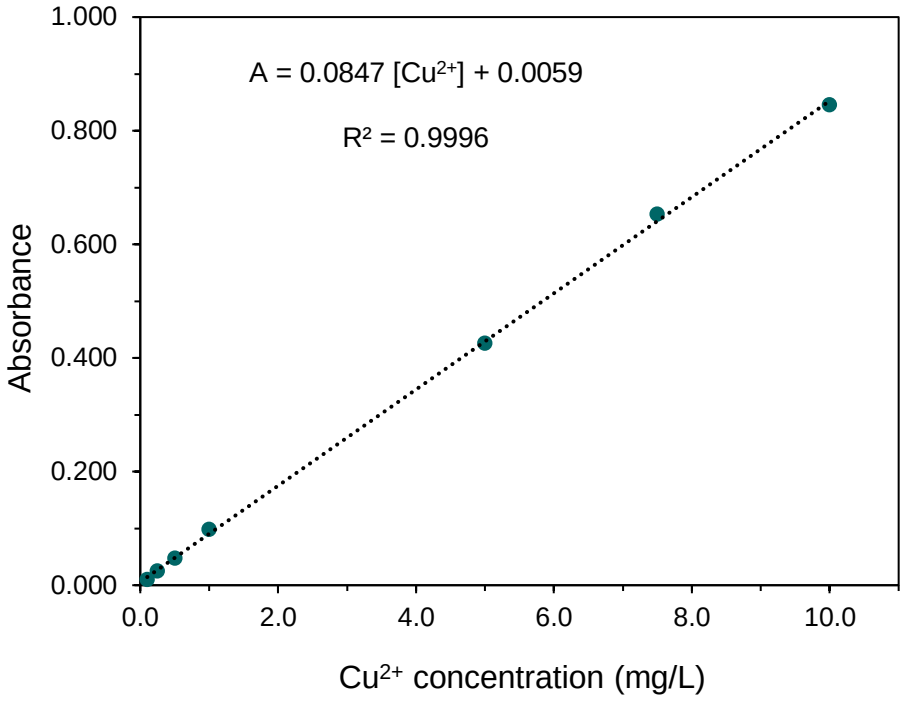

Figure A.1. Calibration curve for the determination of Cu^{2+} concentration.